STATE OF THE CLIMATE IN 2020

THE TROPICS

H. J. Diamond and C. J. Schreck, Eds.

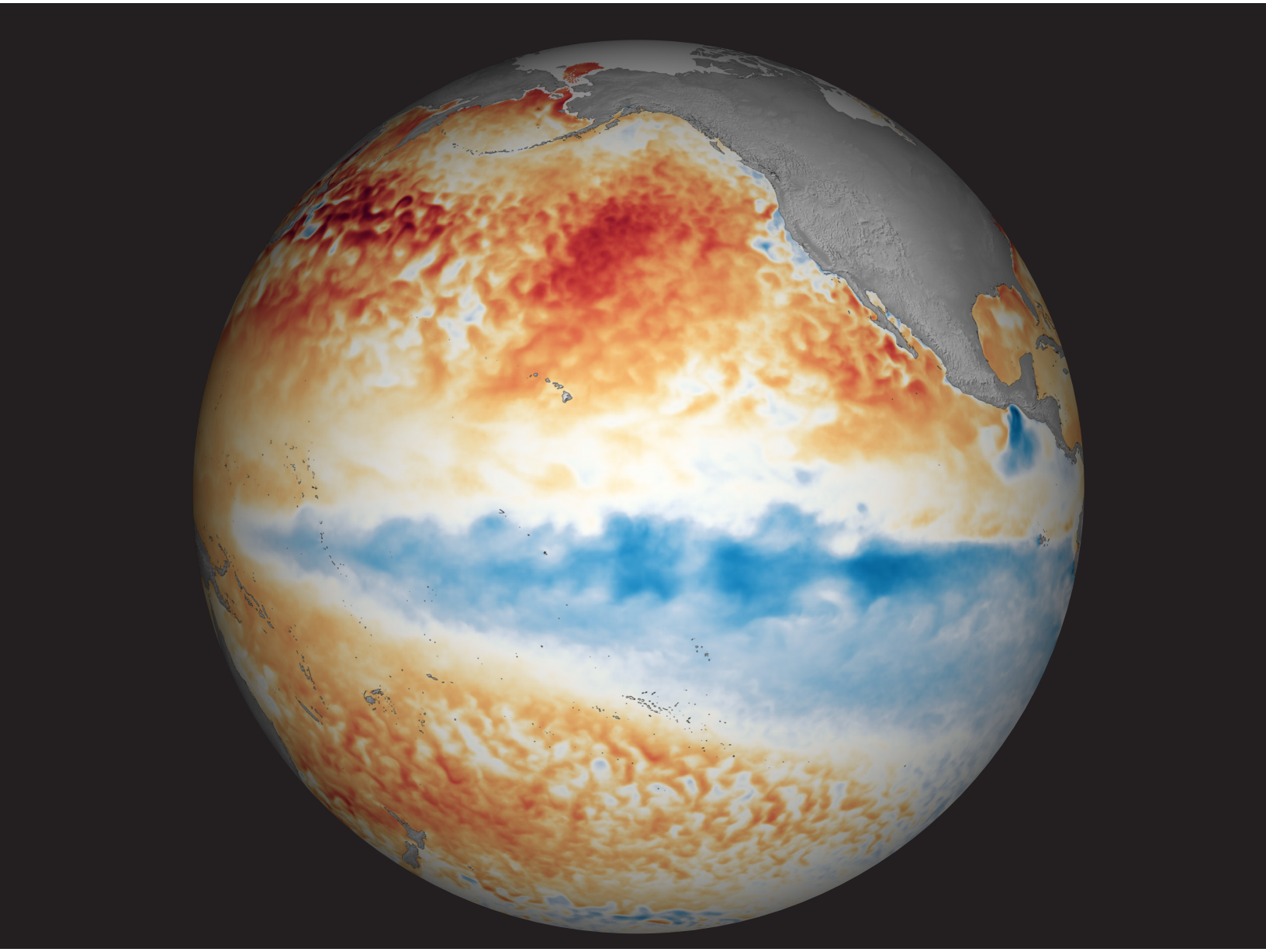

Special Online Supplement to the *Bulletin of the American Meteorological Society* Vol.102, No. 8, August, 2021

https://doi.org/10.1175/BAMS-D-21-0080.1

Corresponding author: Howard J. Diamond / howard.diamond@noaa.gov

STATE OF THE CLIMATE IN 2020
THE TROPICS

Editors

Jessica Blunden
Tim Boyer

Chapter Editors

Freya Aldred
Peter Bissolli
Howard J. Diamond
Matthew L. Druckenmiller
Robert J. H. Dunn
Catherine Ganter
Nadine Gobron
Gregory C. Johnson
Tim Li
Rick Lumpkin
Ademe Mekonnen
John B. Miller
Twila A. Moon
Ahira Sánchez-Lugo
Ted A. Scambos
Carl J. Schreck III
Sharon Stammerjohn
Richard L. Thoman
Kate M. Willett

Technical Editor

Andrea Andersen

***BAMS* Special Editor for Climate**

Michael A. Alexander

American Meteorological Society

Cover credit:
Sea surface temperature (SST) anomalies along the equatorial Pacific in November 2020 compared to the long-term 30-year average from 1981–2010; the blue colors across the equatorial Pacific Ocean indicate below-normal SSTs that are a key and canonical feature associated with the La Niña conditions in place at the time.

The Tropics is one chapter from the *State of the Climate in 2020* annual report and is available from https://doi.org/10.1175/BAMS-D-21-0080.1. Compiled by NOAA's National Centers for Environmental Information, *State of the Climate in 2020* is based on contributions from scientists from around the world. It provides a detailed update on global climate indicators, notable weather events, and other data collected by environmental monitoring stations and instruments located on land, water, ice, and in space. The full report is available from https://doi.org/10.1175/2021BAMSStateoftheClimate.1.

How to cite this document:

Citing the complete report:
Blunden, J. and T. Boyer, Eds., 2021: "State of the Climate in 2020". *Bull. Amer. Meteor. Soc.*, **102** (8), Si–S475, https://doi.org/10.1175/2021BAMSStateoftheClimate.1.

Citing this chapter:
Diamond, H.J. and C. J. Schreck, Eds., 2021: The Tropics [in "State of the Climate in 2020"]. *Bull. Amer. Meteor. Soc.*, **102** (8), S199–S261, https://doi.org/10.1175/BAMS-D-21-0080.1.

Citing a section (example):
Domingues, R., G. J. Goni, J. A. Knaff, I-I Lin, and F. Bringas, 2021: Tropical cyclone heat potential [in "State of the Climate in 2020"]. *Bull. Amer. Meteor. Soc.*, **102** (8), S252–S255, https://doi.org/10.1175/BAMS-D-21-0080.1.

Editor and Author Affiliations (alphabetical by name)

Becker, Emily, J., University of Miami Rosenstiel School of Marine & Atmospheric Science, Miami, Florida
Bell, Gerald D., NOAA/NWS Climate Prediction Center, College Park, Maryland
Blake, Eric S., NOAA/NWS National Hurricane Center, Miami, Florida
Bond, Stephanie, Australian Bureau of Meteorology, Perth, Australia
Bringas, Francis G., NOAA/OAR Atlantic Oceanographic and Meteorological Laboratory, Miami, Florida
Camargo, Suzana J., Lamont-Doherty Earth Observatory, Columbia University, Palisades, New York
Chen, Lin, Institute for Climate and Application Research (ICAR)/KLME/ILCEC/CIC-FEMD, Nanjing University of Information Science and Technology, Nanjing, China
Coelho, Caio A. S., CPTEC/INPE Center for Weather Forecast and Climate Studies, National Institute for Space Research, Cachoeira Paulista, Brazil
Diamond, Howard J., NOAA/OAR Air Resources Laboratory, College Park, Maryland
Domingues, Ricardo, Cooperative Institute for Marine and Atmospheric Studies, University of Miami, Miami, Florida
Goldenberg, Stanley B., NOAA/OAR/AOML Hurricane Research Division, Miami, Florida
Goni, Gustavo, NOAA/OAR/AOML Hurricane Research Division, Miami, Florida
Fauchereau, Nicolas, National Institute of Water and Atmospheric Research, Ltd., Auckland, New Zealand
Halpert, Michael S., NOAA/NWS Climate Prediction Center, College Park, Maryland
He, Qiong, Earth System Modeling Center, Nanjing University of Information Science and Technology, Nanjing, China
Klotzbach, Philip J., Department of Atmospheric Science, Colorado State University, Fort Collins, Colorado
Knaff, John A., NOAA/NESDIS Center for Satellite Applications and Research, Fort Collins, Colorado
L'Heureux, Michelle, NOAA/NWS Climate Prediction Center, College Park, Maryland
Landsea, Chris W., NOAA/NWS National Hurricane Center, Miami, Florida
Lin, I.-I., National Taiwan University, Taipei, Taiwan
Lorrey, Andrew M., National Institute of Water and Atmospheric Research, Ltd., Auckland, New Zealand
Luo, Jing-Jia, Institute for Climate and Application Research (ICAR)/KLME/ILCEC/CIC-FEMD, Nanjing University of Information Science and Technology, Nanjing, China
MacRitchie, Kyle, NOAA/NWS Climate Prediction Center, College Park, Maryland
Magee, Andrew D., Centre for Water, Climate and Land, School of Environmental and Life Sciences, University of Newcastle, Callaghan, NSW, Australia
Noll, Ben, National Institute of Water and Atmospheric Research, Ltd., Auckland, New Zealand
Pasch, Richard J., NOAA/NWS National Hurricane Center, Miami, Florida
Pezza, Alexandre B., Greater Wellington Regional Council, Wellington, New Zealand
Rosencrans, Matthew, NOAA/NWS Climate Prediction Center, College Park, Maryland
Schreck III, Carl J., North Carolina State University, Cooperative Institute for Climate and Satellites–North Carolina (CICS-NC), Asheville, North Carolina
Tippet, Michael K., Department of Applied Physics and Applied Mathematics, Columbia University, New York, New York
Trewin, Blair C., Australian Bureau of Meteorology, Melbourne, Victoria, Australia
Truchelut, Ryan E., "WeatherTiger," Tallahassee, Florida
Wang, Bin, Department of Atmospheric Science and IPRC, University of Hawaii, Honolulu, Hawaii
Wang, Hui, NOAA/NWS Climate Prediction Center, College Park, Maryland
Wood, Kimberly M., Department of Geosciences, Mississippi State University, Mississippi State, Mississippi
Woolley, John-Mark, National Institute of Water and Atmospheric Research, Ltd., Auckland, New Zealand
Young, Steven, H., Independent Researcher, Long Beach, California

Editoral and Production Team

Allen, Jessicca, Graphics Support, Cooperative Institute for Satellite Earth System Studies, North Carolina State University, Asheville, North Carolina
Andersen, Andrea, Technical Editor, Innovative Consulting and Management Services, LLC, NOAA/NESDIS National Centers for Environmental Information, Asheville, North Carolina
Hammer, Gregory, Content Team Lead, Communications and Outreach, NOAA/NESDIS National Centers for Environmental Information, Asheville, North Carolina
Love-Brotak, S. Elizabeth, Lead Graphics Production, NOAA/NESDIS National Centers for Environmental Information, Asheville, North Carolina
Misch, Deborah J., Graphics Support, Innovative Consulting and Management Services, LLC, NOAA/NESDIS National Centers for Environmental Information, Asheville, North Carolina
Riddle, Deborah B., Graphics Support, NOAA/NESDIS National Centers for Environmental Information, Asheville, North Carolina
Veasey, Sara W., Visual Communications Team Lead, Communications and Outreach, NOAA/NESDIS National Centers for Environmental Information, Asheville, North Carolina

4. Table of Contents

*Please refer to Chapter 8 (Relevant datasets and sources) for a list of all climate variables and datasets used in this chapter for analyses, along with their websites for more information and access to the data.

4. THE TROPICS

H. J. Diamond and C. J. Schreck, Eds.

a. Overview—H. J. Diamond and C. J. Schreck

The tropics in 2020 reflected El Niño–Southern Oscillation neutral conditions through June–August, with the index decreasing from positive values during boreal spring to negative values during boreal summer. Starting in July–September (JAS), La Niña thresholds were met, with Oceanic Niño Index (ONI) values decreasing through October–December (OND). In OND 2020, the ONI reached a minimum of –1.3°C, which is considered informally to be a La Niña of moderate strength (ONI values between –1.0°C and –1.4°C). The ONI reached and slightly exceeded the +0.5°C threshold in several seasons during the Northern Hemisphere (NH) winter of 2019/20, but the anomalies were weak and did not last long enough to be considered an El Niño episode.

For the global tropics, combined land and ocean surface temperatures (measured at 20°S–20°N) registered +0.43°C above the 1981–2010 average. This makes 2020 the fourth-warmest year for the tropics since records began in 1880. The five warmest years have all occurred since 2015. Data from the Global Precipitation Climatology Project indicate a mean annual total precipitation value of 1317 mm across the 20°S–20°N latitude band over land. This is 11 mm above the 1981–2010 average and ranks 11th in the 1979–2020 period of record.

Globally, 102 named tropical cyclones (TCs; ≥34 kt; or ≥17 m s^{-1}) were observed during the 2020 NH season (January–December 2020) and the 2019/20 Southern Hemisphere season (July–June 2019/20; Table 4.2), as documented in IBTrACSv4 (Knapp et al. 2010). Overall, this number was well above the 1981–2010 global average of 85 TCs, slightly greater than the 96 TCs reported during 2019 (Diamond and Schreck 2020), and was three storms shy of the record 104 named storms in 1992. The 30 named storms in the North Atlantic during 2020 surpassed the previous record of 28 set in 2005. For the North Atlantic, the 14 hurricanes during 2020 were the second most on record behind the 15 observed in 2005, and the seven major hurricanes were the most on record, tying the seven observed in 2005.

In terms of Accumulated Cyclone Energy (ACE; Bell et al. 2000), all basins were below their 1981–2010 averages except for the North Atlantic and North Indian Ocean basins. The 2020 seasonal ACE value in the North Atlantic was 191.5% of the 1981–2010 median. This value is the sixth highest since 1970 and is above NOAA's threshold (Bell et al 2011) for both an above-normal (120%) and an extremely active (165%) season. There have now been a record five consecutive above-normal seasons, which surpasses the previous record of four set in 1998–2001. In the western North Pacific, Super Typhoons Goni and Haishen and Typhoon Maisak contributed 45% of the seasonal ACE for that basin. The Australian and South Indian Ocean basins were comparatively quiet; each had an ACE that was below normal. The global total ACE was below the average for 1981–2010 at 574×10^4 kt^2 and well below the 795×10^4 kt^2 value recorded in 2019. Three TCs across the globe reached Saffir–Simpson Hurricane Wind Scale (https://www.nhc.noaa.gov/aboutsshws.php) Category 5 intensity level, one in the western North Pacific (Goni), one in the North Indian Ocean (Amphan), and one in the southwest Pacific (Harold).

b. ENSO and the tropical Pacific—M. L'Heureux, E. Becker, M. S. Halpert, Z.-Z. Hu, K. MacRitchie, and M. Tippett

The El Niño–Southern Oscillation (ENSO) is a coupled ocean–atmosphere climate phenomenon across the tropical Pacific Ocean, with opposite phases called El Niño and La Niña. For historical purposes, NOAA's Climate Prediction Center (CPC) classifies and assesses the strength and duration of El Niño and La Niña events using the Oceanic Niño Index (ONI, shown for mid-2019 through 2020 in Fig. 4.1). The ONI is the 3-month (seasonal) running average of sea surface temperature (SST) anomalies in the Niño-3.4 region (5°S–5°N, 170°–120°W), currently calculated as the departure from the 1991–2020 base period mean.[1] El Niño is classified when the ONI is at or greater than +0.5°C for at least five consecutive and overlapping seasons, while La Niña occurs when the ONI is at or less than −0.5°C for at least five consecutive and overlapping seasons.

The ONI reached and slightly exceeded the +0.5°C threshold in several seasons during the Northern Hemisphere winter of 2019/20, but the anomalies were weak and did not last long enough to be considered an El Niño episode. Consequently, NOAA CPC and other agencies (e.g., Australian Bureau of Meteorology and World Meteorological Organization) did not post El Niño advisories or alerts during the boreal winter of 2019/20. At times, intraseasonal variability also contributed to El Niño-like atmospheric anomalies across the tropical Pacific Ocean, especially during mid-January and mid-February (see section 4c).

The ONI reflected ENSO-neutral conditions through June–August (JJA) 2020, with the index decreasing from positive values during boreal spring to negative values during boreal summer. Starting in July–September (JAS), La Niña thresholds were met, with ONI values decreasing through October–December.[2] During this period, the ONI reached a minimum of –1.3°C, which is considered informally to be a La Niña of moderate strength (ONI values between –1.0°C and –1.4°C).

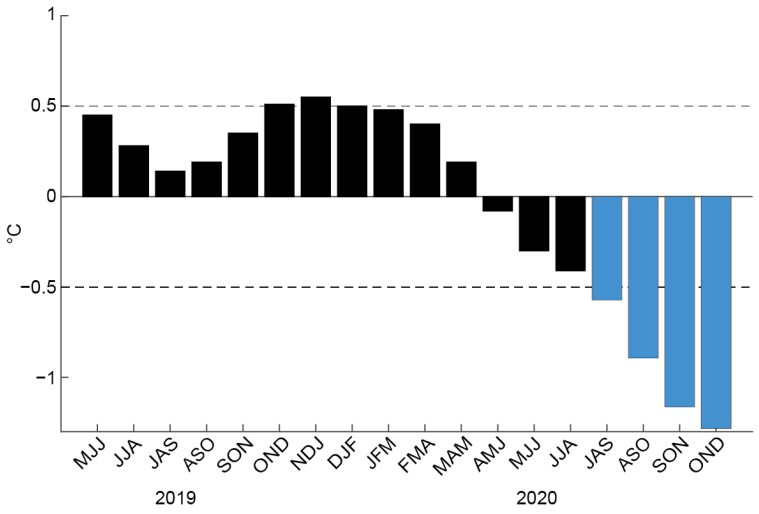

Fig. 4.1. Time series of the ONI (°C) from mid-2019 through 2020. Overlapping 3-month seasons are labeled on the *x*-axis, with initials indicating the first letter of each month in the season. Blue bars indicate negative values that are below –0.5°C. The ONI values are derived from the ERSSTv5 dataset and are based on departures from the 1991–2020 period monthly means (Huang et al. 2017).

1) Oceanic conditions

Figure 4.2 displays the mean SST (left column) and SST anomalies (right column) for four, 3-month periods from December–February (DJF) 2019/20 through September–November (SON) 2020. SST anomalies on the equator during DJF (Fig. 4.2, top row) exceeded +1.0°C near the date line, extending from 170°W to 160°E. The western Pacific warm pool extended farther east than its mean position, with the 30°C isotherm reaching the date line. However, the east-central and eastern equatorial Pacific remained near average during DJF 2019/20.

[1] The ONI is an index measuring a climate phenomenon, ENSO, and for that reason, the base period is updated every 5 years with a rolling 30-year climatology. The rolling climatology is used in part to remove those secular SST trends and focus on the state of ENSO. The 1986–2015 normal was used operationally for 2020, but it was updated to 1991–2020 at the completion of the year.

[2] While the season November 2020–January 2021 (NDJ) is not covered by this review, the NDJ value of the ONI was –1.2°C. Therefore, the period beginning in JAS 2020 is part of an official La Niña episode.

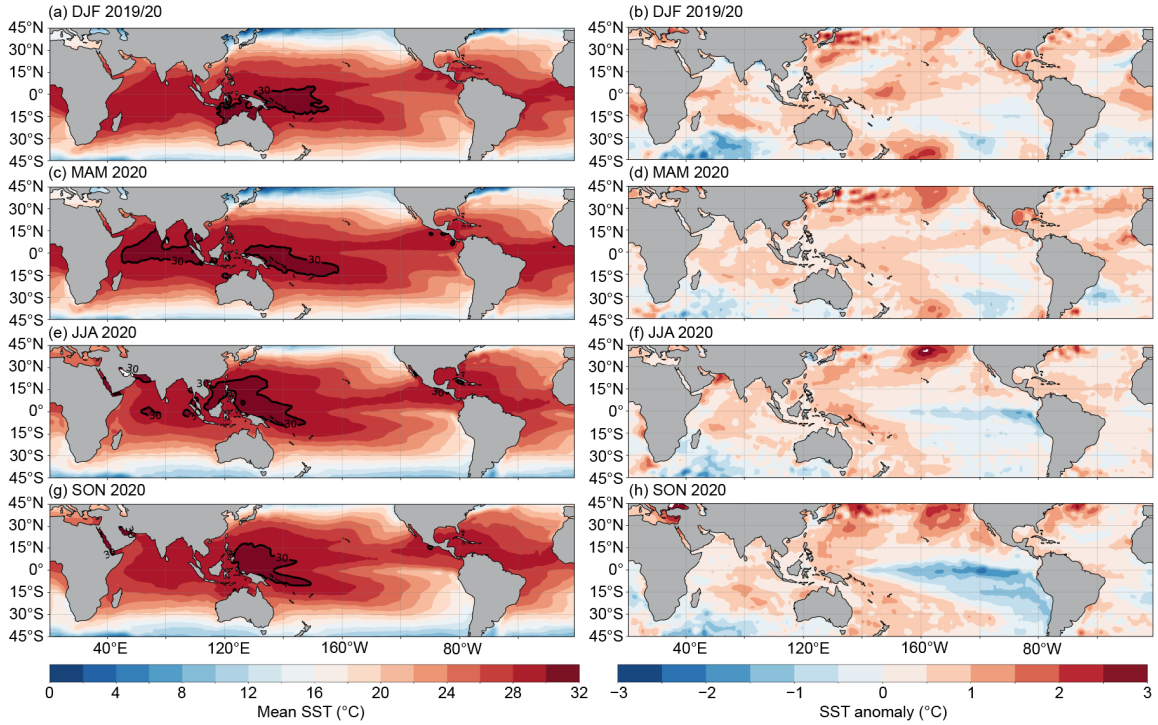

Fig. 4.2. (left) Mean SST and (right) SST anomaly for (°C) (a), (b) DJF 2019/20, (c), (d) MAM 2020, (e), (f) JJA 2020, and (g), (h) SON 2020. The bold contour for total SST is located at 30°C. Anomalies are departures from the 1981–2010 seasonal adjusted OI climatology (Reynolds et al. 2002).

The duration of positive SST anomalies was too short to be considered an El Niño episode, and by March–May (MAM) 2020, anomalies weakened across the equatorial Pacific Ocean (Figs. 4.2a–d). However, SSTs remained elevated in the western equatorial Pacific and extended east-northeast to coastal Central America. While this band of positive SST anomalies projects onto the optimal SST growth pattern that can precede the development of El Niño the following winter (Penland and Sardeshmukh 1995), by SON 2020 the Pacific had instead transitioned to La Niña.

By JJA 2020 (Figs. 4.2e,f), the western Pacific warm pool had retracted farther west and the cold tongue was stronger than average. Negative SST anomalies became more prominent on the equator from ~160°W to the South American coast. During SON 2020 (Figs. 4.2g,h), these negative SST anomalies strengthened and expanded even farther west to the date line. By this season, SST anomalies exceeded –1.0°C across the east-central and eastern equatorial Pacific Ocean. Below-average SSTs were also quite prominent in the southeastern Pacific Ocean, reaching coastal Chile. These subtropical SST anomalies were asymmetric across the hemispheres. Below-average SSTs did not extend into the northeastern Pacific Ocean, which was instead above average.

Consistent with the SST evolution, subsurface temperatures during DJF 2019/20 were above average in the central and eastern equatorial Pacific Ocean (Fig. 4.3a). Near the date line, temperature anomalies in excess of +1.5°C extended from ~150-m depth to the surface. Like those at the surface, the positive subsurface temperature anomalies weakened by MAM (Fig. 4.3b), and, by JJA, negative subsurface temperature anomalies dominated the eastern equatorial Pacific Ocean (Fig. 4.3c). This cooling reflected the shallower oceanic thermocline and increased upwelling that accompanies a developing La Niña. During SON 2020 (Fig. 4.3b), the shoaling of the equatorial thermocline in the eastern Pacific was most apparent relative to earlier in the year, and subsurface temperature anomalies were –4.5°C or cooler at a depth of ~50–100 m. Late in the year, positive temperature anomalies remained weak and confined at depth near the date line and in the western Pacific. The east–west contrast in subsurface temperature anomalies is consistent with the tilt mode of ENSO (Clarke 2010; Kumar and Hu 2014).

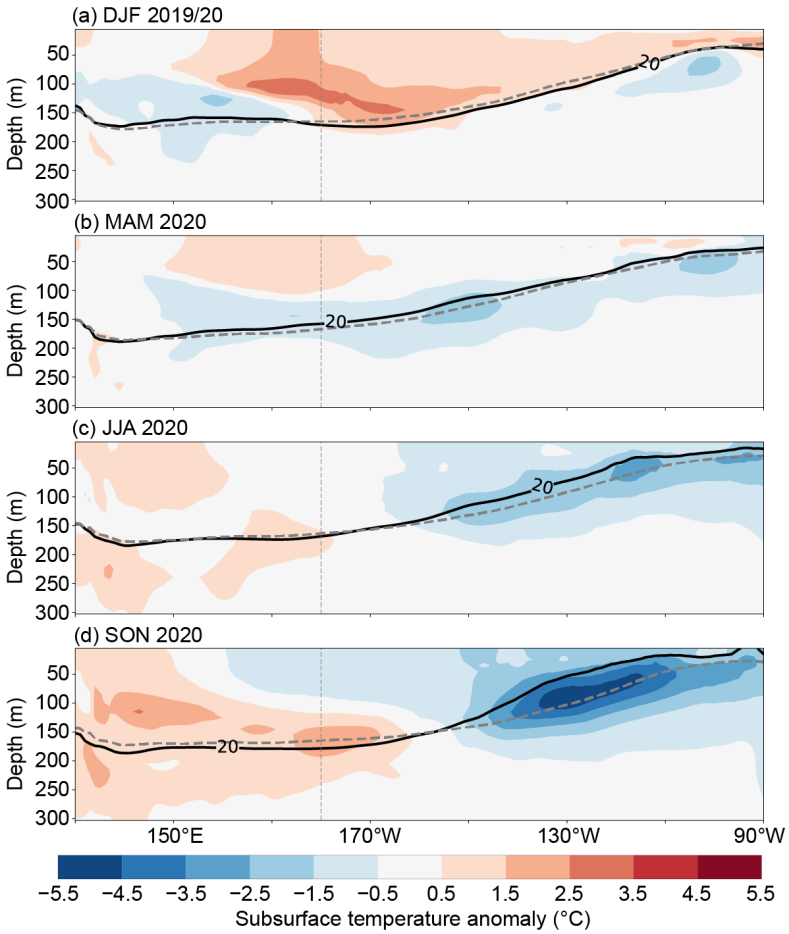

Fig. 4.3. Equatorial depth–longitude section of Pacific Ocean temperature anomalies (°C) averaged between 5°S and 5°N during (a) DJF 2019/20, (b) MAM 2020, (c) JJA 2020, and (d) SON 2020. The 20°C isotherm (thick solid line) approximates the center of the oceanic thermocline. The gray, dashed line shows the climatology of the 20°C isotherm based on 1982–2010. The data are derived from a reanalysis system that assimilates oceanic observations into an oceanic general circulation model (Behringer et al. 1998). Anomalies are departures from the 1982–2010 period monthly means.

2) Atmospheric circulation and precipitation anomalies from December–February 2019/20 to June–August 2020

The pattern of tropical convection and low-level winds during DJF 2019/20 was associated with weak warm SST anomalies (Figs. 4.4–4.6). Specifically, tropical convection (as measured by outgoing longwave radiation [OLR]) was enhanced around the date line (green shading) and suppressed over Indonesia (brown shading; Fig. 4.4a). Low-level (850-hPa) tropical wind anomalies were westerly over the western Pacific Ocean during DJF (Fig. 4.5a). Upper-level (200-hPa) tropical winds were westerly across the central to eastern Pacific Ocean, and were strongest over the eastern Pacific (Fig. 4.6a). Despite the enhanced convection around the date line, the upper-level zonal wind anomalies were not divergent on the equator (though meridional wind anomalies were divergent over the western Pacific, highlighting the lack of a robust circulation response through the entire atmosphere to the underlying SST anomaly pattern). Because the climatological 200-hPa winds are westerly from ~160°W to coastal South America during this season, the upper-branch of the Pacific Walker circulation was stronger than average. The lack of a weak Walker circulation at upper levels, the mild, westward shifted SST anomalies, and the short duration of warming precluded the designation of El Niño conditions during DJF 2019/20. Furthermore, several pulses of enhanced convection occurred near the date line, concurrent with the passage of eastward-propagating intraseasonal disturbances that can be seen in the 200-hPa velocity potential anomalies in early 2020 (see Fig. 4.7).

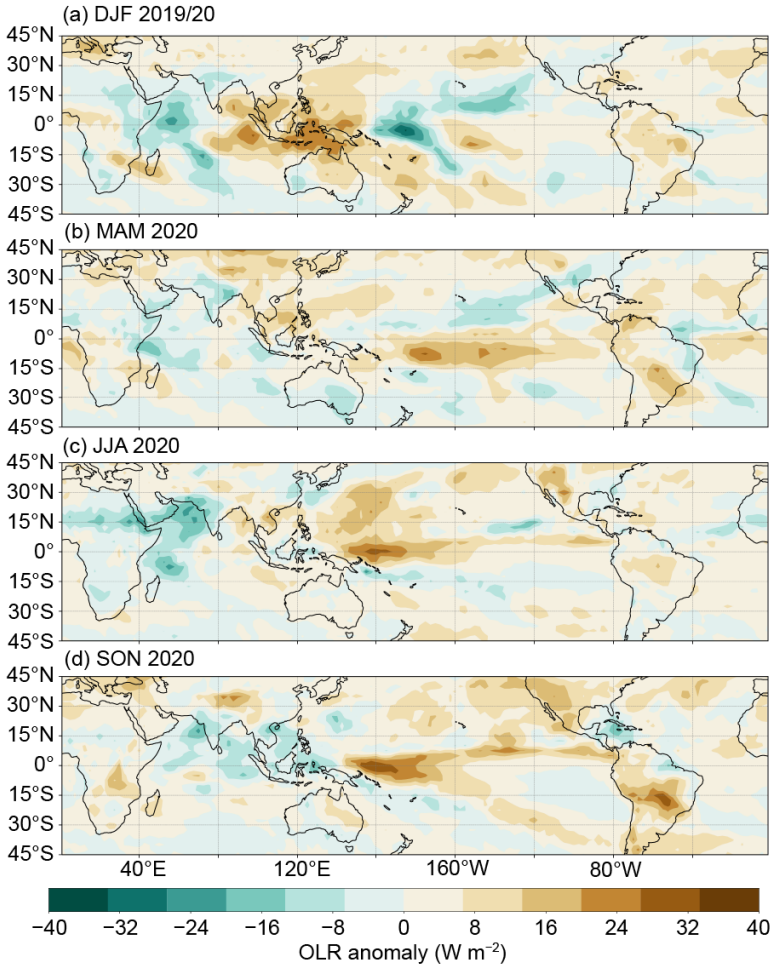

Fig. 4.4. OLR anomalies (shaded, W m^{-2}), during (a) DJF 2019/20, (b) MAM 2020, (c) JJA 2020, and (d) SON 2020. Anomalies are departures from the 1981–2010 period monthly means. Data are from the NCEP/NCAR Reanalysis (Kalnay et al. 1996).

ENSO-neutral conditions continued through JJA though signs of a developing La Niña were evident in anomalies of OLR and winds during the boreal spring and summer. In particular, below-average convection was observed near the date line starting in MAM (Fig. 4.4b). These suppressed OLR anomalies were initially focused south of the equator and became more equatorially confined to the western and central Pacific during JJA (Fig. 4.4c). Low-level trade winds were enhanced, with easterly wind anomalies observed on the equator starting in MAM and continuing through the remainder of 2020 (Figs. 4.5b–d). The strengthening of the upper-level branch of the Walker circulation, first seen in the 200-hPa wind anomalies in DJF 2019/20, also persisted throughout the remainder of the year, with the brief exception of near-average winds in the central Pacific during JJA 2020 (Fig. 4.6c). The upper-level branch of the Walker Circulation became stronger again with the onset of La Niña in SON (Fig. 4.6d).

3) Atmospheric circulation and precipitation anomalies during La Niña (September–November 2020)

As La Niña formed in JAS 2020, its signal increasingly dominated the atmospheric circulation over the tropical Pacific Ocean. A convective anomaly dipole became evident as the Pacific Walker circulation strengthened. Suppressed convection became even more noticeable in the western and central equatorial Pacific during SON (Fig. 4.4d). Enhanced convection appeared around Indonesia, extending northwestward into Southeast Asia and India. Anomalous low-level easterlies were prominent across most of the equatorial Pacific Ocean (Fig. 4.5d) along with anomalous upper-level westerlies overlying them (Fig. 4.6d). These wind anomalies also reflect the further strengthening of the Walker circulation as per Bjerknes (1969).

While global teleconnections are typically strongest following the peak of La Niña in the boreal winter, there were extratropical circulation anomalies that resembled La Niña during SON 2020. In particular, over the North Pacific Ocean, the retraction of the East Asia–North Pacific jet stream was evident in the easterly wind anomalies from ~20°N to 40°N (Fig. 4.6d). This signal was hemispherically symmetric, with a weakened jet stream also apparent across the middle latitudes of the South Pacific Ocean. A wave train with positive height anomalies around New Zealand, negative height anomalies near West Antarctica, and positive height anomalies east of Argentina is reminiscent of the Pacific–South America pattern (Mo and Higgins 1998).

In addition to suppressed precipitation over Indonesia and Southeast Asia, La Niña is typically associated with below-average precipitation anomalies over parts of the southwestern United States and coastal southern Alaska, which indeed emerged during SON. Southern Brazil, Chile, and Argentina, experienced below-average precipitation in SON, which has been shown to be influenced by La Niña conditions (Ropelewski and Halpert 1989).

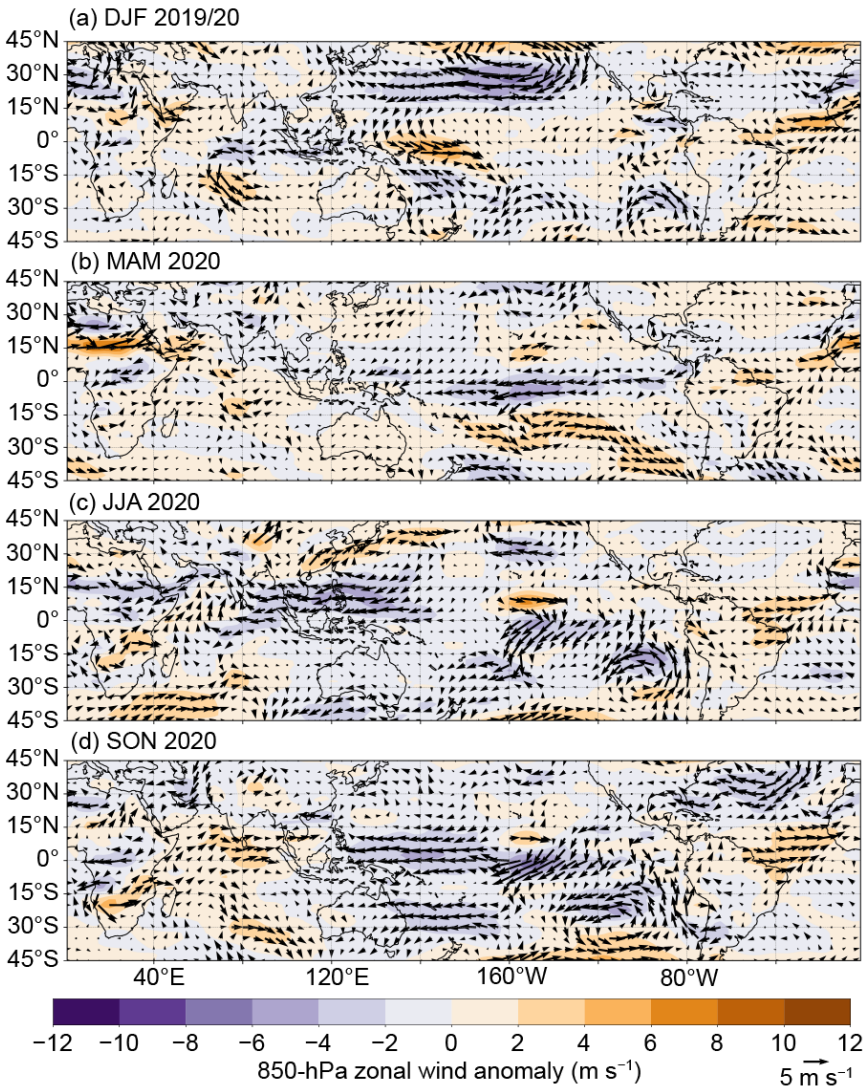

Fig. 4.5. Anomalous 850-hPa wind vectors and zonal wind speed during (a) DJF 2019/20, (b) MAM 2020, (c) JJA 2020, and (d) SON 2020. The reference wind vector is located at the bottom right. Anomalies are departures from the 1981–2010 period monthly means. Data are from the NCEP/NCAR Reanalysis (Kalnay et al. 1996).

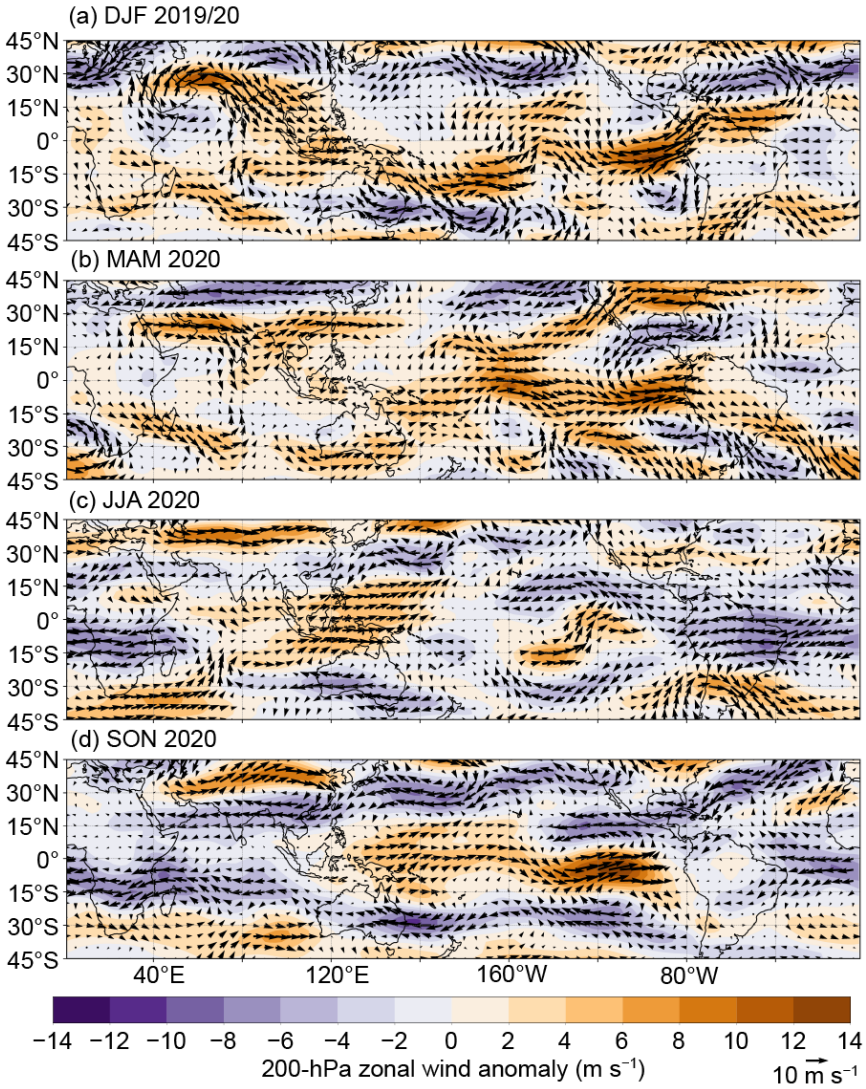

Fig. 4.6. Anomalous 200-hPa wind vectors and zonal wind speed during (a) DJF 2019/20, (b) MAM 2020, (c) JJA 2020, and (d) SON 2020. The reference wind vector is located at the bottom right. Anomalies are departures from the 1981–2010 period monthly means. Data are from the NCEP/NCAR Reanalysis (Kalnay et al. 1996).

c. Tropical intraseasonal activity—K. MacRitchie and C. Schreck

The Madden-Julian Oscillation (MJO; Madden and Julian 1971, 1972, 1994; Zhang 2005) and convectively coupled equatorial wave activity (Wheeler and Kiladis 1999; Kiladis et al. 2009) are the primary modes of tropical intraseasonal variability. The MJO is the leading mode of intraseasonal variability in the tropics and is characterized by an eastward-propagating convective envelope generally traverses the globe in 30–60 days. Other convectively coupled equatorial waves, such as atmospheric Kelvin and equatorial Rossby waves, are typically zonally narrower and faster than the MJO. All of these waves affect weather patterns around the globe, though the MJO has the most robust connections with midlatitude synoptic circulations (Knutson and Weickmann 1987; Kiladis and Weickmann 1992; Mo and Kousky 1993; Kousky and Kayano 1994; Kayano and Kousky 1999; Cassou 2008; Lin et al. 2009; Riddle et al. 2012; Schreck et al. 2013; Baxter et al. 2014) and can impact monsoons (Krishnamurti and Subrahmanyam 1982; Lau and Waliser 2012) and tropical cyclones (Mo 2000; Frank and Roundy 2006; Camargo et al. 2009; Schreck et al. 2012; Diamond and Renwick 2015).

The MJO is often episodic, with periods of moderate-to-strong activity followed by little or no activity (e.g., Matthews 2008). Common metrics for identifying the MJO include time–longitude plots of anomalous 200-hPa velocity potential and outgoing longwave radiation (OLR; Fig. 4.7) and the Wheeler-Hendon (2004) Real-time Multivariate MJO (RMM) index (Fig. 4.8). In the time–longitude

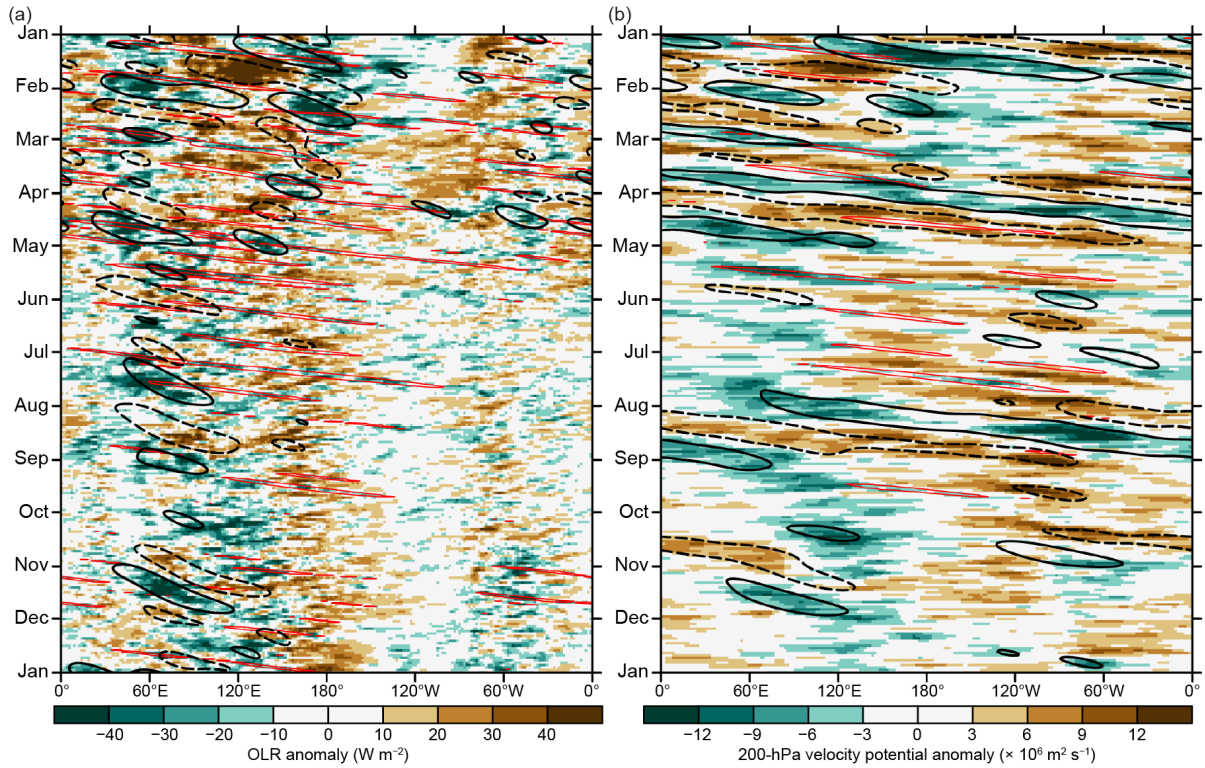

Fig. 4.7. Time–longitude section of (a) OLR (Schreck et al. 2018) anomalies (W m^{-2}) and (b) 200-hPa velocity potential anomalies (× 10^6 m^2 s^{-1}) from the CFSR (Saha et al. 2014). Both variables are averaged over 10°S–10°N. Time increases downward on this graph, beginning with Jan 2020 at the top and ending with Jan 2021 at the bottom. Negative anomalies (green) indicate enhanced convection, and positive anomalies (brown) indicate suppressed convection. Contours identify anomalies filtered for the MJO (black) and atmospheric Kelvin waves (red). Contours are drawn at ±12 W m^{-2} and ±4 × 10^6 m^2 s^{-1} with the enhanced (suppressed) convective phase of these phenomena indicated by solid (dashed) contours. Anomalies are departures from the 1981–2010 base period daily means.

plots, the MJO exhibits eastward propagation from upper-left to lower-right. In the RMM plots, the MJO propagation and intensity are seen as large, counter-clockwise circles around the origin.

The MJO was more active during the first 5 months of 2020 than it was during the remainder of the year (Fig. 4.7, black contours). The strongest MJO activity occurred during January (Fig. 4.8), with a zonal wave number 1 pattern across the tropical strip. The RMM index showed an especially prominent signal over the Maritime Continent during mid-January (Fig. 4.8a), which then weakened during February before strengthening again over the Indian Ocean during March. This period of MJO activity projected more strongly onto the 200-hPa velocity potential anomaly field (Fig. 4.7b) than the OLR anomaly field (Fig. 4.7a) or the 850-hPa zonal wind anomaly field (Fig. 4.9a), which is a common characteristic of MJO events (Straub 2013).

The high-amplitude MJO activity coincided with a period of anomalously high sea surface temperatures (SSTs) in the central and eastern Pacific (Fig. 4.2), resulting in positive Oceanic Nino Index values (Fig. 4.1) and El Niño-like OLR anomalies (Fig. 4.7a). Strong MJO activity often precedes El Niño events, but is often weak during La Niña events (Hendon et al. 1999; Zhang and Gottschalck 2002; Zhang 2005). Zonal wind anomalies at 850-hPa were also enhanced during this period (Fig. 4.9a), with westerly wind bursts (WWBs) evident in January and April across the western and central Pacific. The WWB activity likely aided development of an oceanic Kelvin wave, which began in January and continued through the April (Fig. 4.9a).

SST anomalies trended negative beginning in April (Fig. 4.1) and eventually developed La Niña criteria during the July–September period. MJO activity also weakened substantially around this time (Fig. 4.7). The primary intraseasonal convective variability during this period was a series of prominent atmospheric Kelvin waves (Fig. 4.7, red contours), which move eastward with a smaller scale and faster phase speed than the MJO.

There were only two distinct MJO events in the second half of 2020: one in mid-July to early September and one in late October through November. These types of events have been shown to be particularly impactful for modulating tropical cyclone (TC) activity (Klotzbach 2010). They likely contributed to the most active periods for TC activity over the North Pacific and North Atlantic. The suppressed phase in late September–early October also contributed to a relative lack of TC activity in the North Atlantic during that time.

The typical MJO structure features anomalous easterlies throughout the low levels of the suppressed region of the convective envelope (Rui and Wang 1990), resulting in a surge of trade winds throughout the Pacific. Indeed, trade wind surges are evident in the 850-hPa zonal wind anomaly plot (Fig. 4.9a) during late August and November. Such trade wind surges are consistent with La Niña conditions (see section 4b).

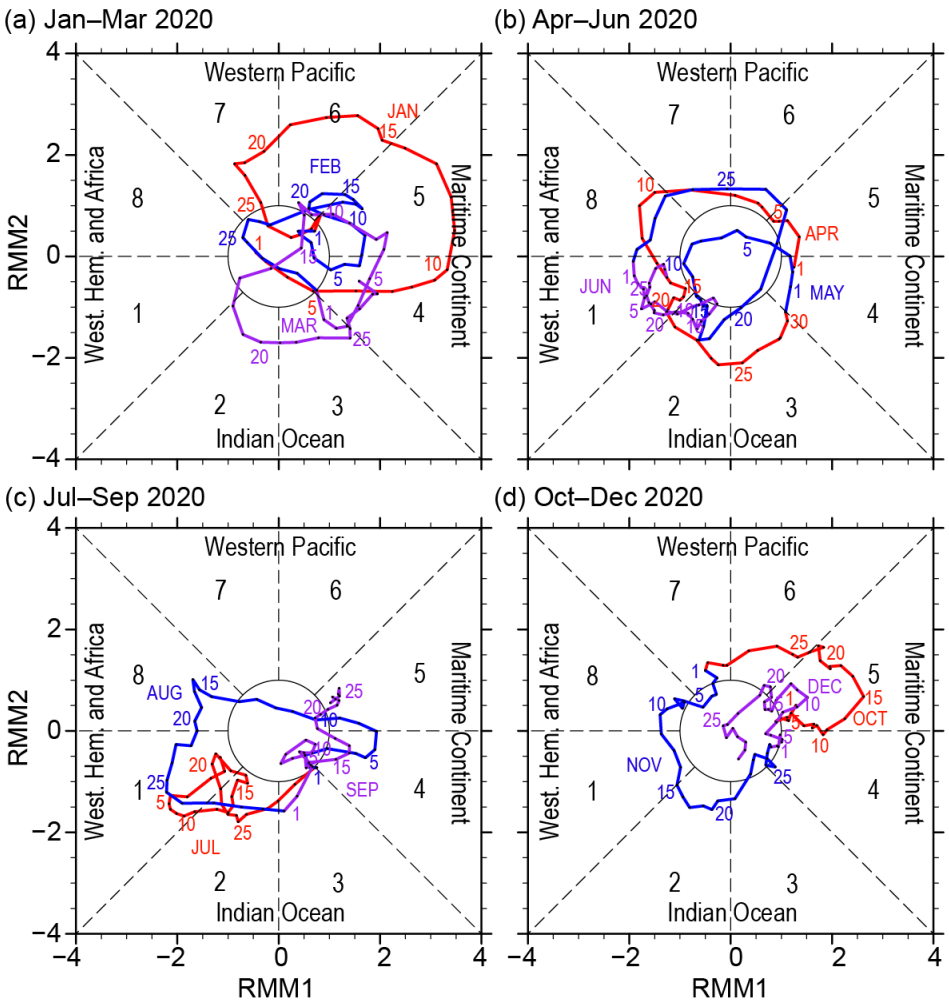

Fig. 4.8. Wheeler and Hendon (2004) RMM index for (a) Jan–Mar, (b) Apr–Jun, (c) Jul–Sep, and (d) Oct–Dec 2020. Each point represents the MJO amplitude and location on a given day, and the connecting lines illustrate its propagation. Amplitude is indicated by distance from the origin, with points inside the circle representing weak or no MJO. The eight phases around the origin identify the region experiencing enhanced convection, and counter-clockwise movement is consistent with eastward propagation.

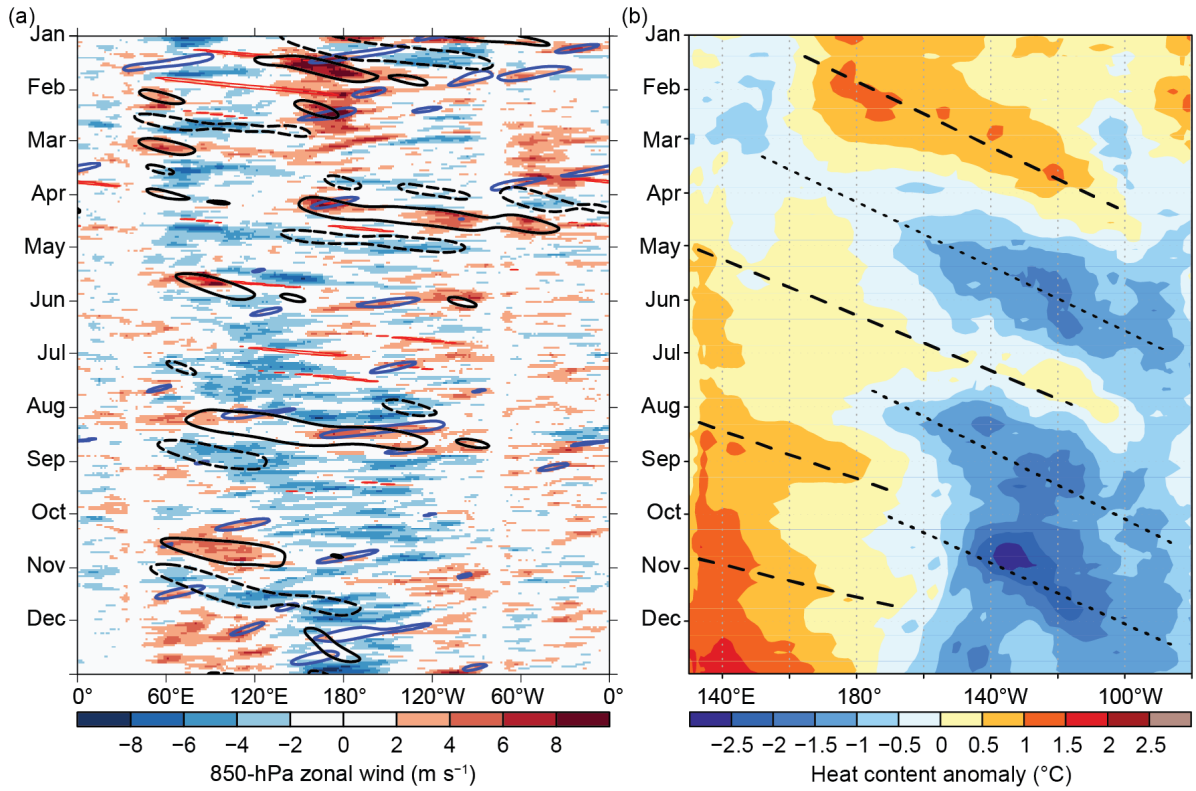

Fig. 4.9. (a) Time–longitude section for 2020 of anomalous 850-hPa zonal wind (m s^{-1}) averaged for 10°N to 10°S. Contours identify anomalies filtered for the MJO (black), atmospheric Kelvin waves (red), and equatorial Rossby waves (blue). Significant WWBS and trade wind surges over the equatorial Pacific that resulted in notable downwelling and upwelling oceanic Kelvin waves are dashed and dotted respectively. (b) Time–longitude section for 2020 of the anomalous equatorial Pacific Ocean heat content (°C), calculated as the mean temperature anomaly between 0–300-m depth. Yellow/red (blue) shading indicates above- (below-) average heat content. Relative warming (dashed lines) and cooling (dotted lines) due to downwelling and upwelling equatorial oceanic Kelvin waves are indicated. Anomalies are departures from the 1981–2010 base period pentad means. Data in (b) are derived from an analysis system that assimilates oceanic observations into an oceanic general circulation model (Behringer et al. 1998).

d. Intertropical convergence zones

1) Pacific—N. Fauchereau and B. Noll

Tropical Pacific rainfall patterns are dominated by two convergence zones, the Intertropical Convergence Zone (ITCZ; Schneider et al. 2014) north of the equator and the South Pacific Convergence Zone (SPCZ; Vincent 1994). Figure 4.10 summarizes the behavior for both convergence zones during 2020 using rainfall estimated from satellite microwave and infrared data in a product known as the Climate Prediction Center (CPC) Morphing Technique (CMORPH; Joyce et al. 2004). Rainfall transects over 30°S to 20°N are presented for each quarter of the year, averaged across successive 30-degree longitude bands, starting in the western Pacific at 150°E–180°. The 2020 seasonal variation is compared against the longer-term 1998–2019 CMORPH climatology.

Early in the year, the El Niño–Southern Oscillation (ENSO) phase was neutral, although an area of above-average ocean temperatures was located in the west-central Pacific, with a spatial signature somewhat similar to a weak, central Pacific El Niño (El Niño "Modoki"; see Ashok et al. 2007), although the Modoki condition is not a formal part of the ENSO section of this report (section 4b). The transects for January–March (Fig. 4.10a) for the western and central Pacific (150°W–150°E, especially 150°E to the date line) show that the SPCZ mean signature was shifted northeast of its climatological position, while the ITCZ appears to have been displaced slightly equatorward compared to normal. These anomalies were weak, but somewhat consistent with typical Modoki patterns (Ashok et al. 2007).

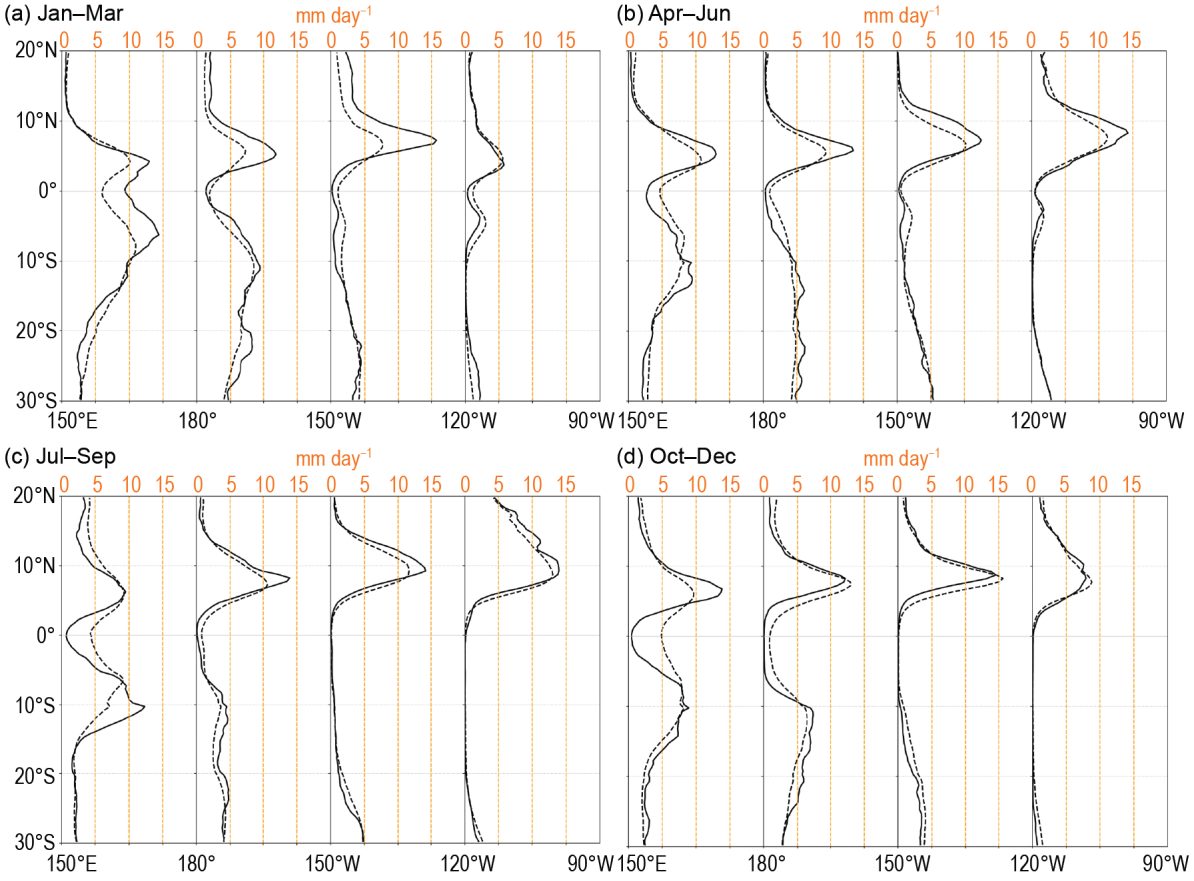

Fig. 4.10. Rainfall rate (mm day^{-1}) from the CMORPH analysis for (a) Jan–Mar, (b) Apr–Jun, (c) Jul–Sep, and (d) Oct–Dec of 2020. The separate panels for each quarter show the rainfall cross-section between 30°S and 20°N (solid line) and the 1998–2019 climatology (dotted line), separately for four 30° sectors from 150°E–180° to 120°–90°W.

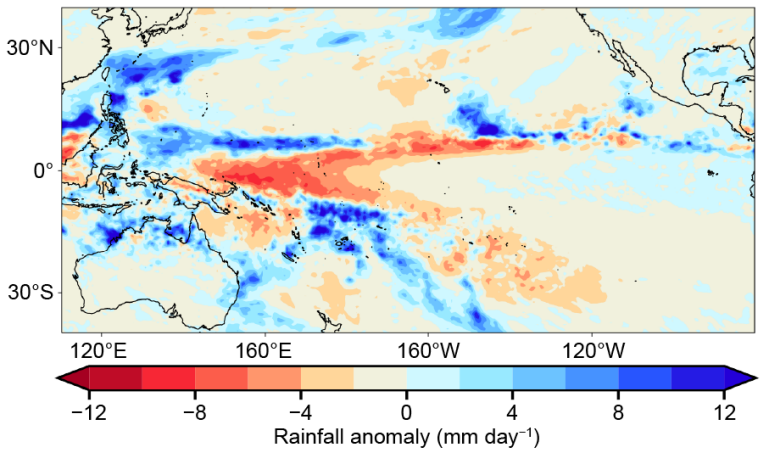

Fig. 4.11. Rainfall anomalies (mm day^{-1}) from CMORPH analysis for Dec 2020. The anomalies are calculated with respect to the 1998–2019 climatology.

During boreal summer, an increase in tropical trade winds contributed to cooling ocean temperatures across the equatorial central and eastern Pacific. At the end of 2020, it became more apparent that the La Niña was of the non-traditional central Pacific flavor, with the coolest sea surface temperatures (SSTs) located toward the central Pacific. Cooling SSTs across the central and eastern Pacific were accompanied with distinct shifts in the ITCZ position and intensity: from April to June, all sectors of the Pacific (see Fig. 4.10b) showed an ITCZ shifted north of its climatological position, with rainfall rates within the convergence zone exceeding climatological values. The ITCZ remained to the north of its usual position throughout the remainder of 2020, a pattern broadly consistent with La Niña conditions.

Meanwhile, the position and intensity of the SPCZ showed large month-to-month variability. During La Niña years, the SPCZ tends to be displaced to the southwest of its climatological position and, conversely, the SPCZ northeast of its climatological position during El Niño years. The SPCZ followed this pattern in the last quarter of 2020, as exemplified by anomalies recorded in December (Fig. 4.11).

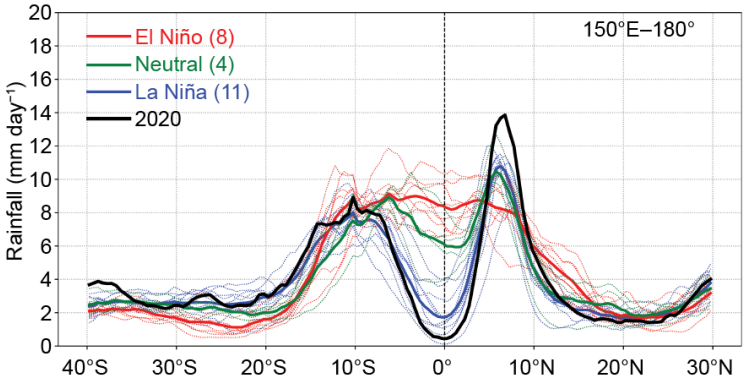

Fig. 4.12. CMORPH rainfall rate (mm day^{-1}) for Oct–Dec, for each year 1998 to 2019, averaged over the longitude sector 150°W–180°. The cross-sections are color-coded according to NOAA's ONI, except 2020, which is shown in black. Dotted lines are individual years and solid lines are the average over all years in each ENSO phase. Inset legend indicates how many years went into each composite.

Figure 4.12 shows a more detailed comparison of the western Pacific (150°E–180°) CMORPH rainfall transects for all years from 1998 to 2020. In 2020, October–December (OND) has a relatively clear La Niña signal. The ITCZ intensified and was shifted north of its climatological position, with the strongest positive anomalous precipitation rates on record between about 7°N and 9°N. Conversely, rainfall rates along the equator were among the lowest on record, which was consistent with La Niña conditions (blue line on Fig. 4.12). Farther south, the SPCZ position and intensity in OND 2020 was close to the composite average during La Niña years.

2) Atlantic—A. B. Pezza and C. A. S. Coelho

The Atlantic ITCZ is a well-organized convective band that oscillates between approximately 5°–12°N during July–November and 5°S–5°N during January–May (Waliser and Gautier 1993; Nobre and Shukla 1996). Equatorial atmospheric Kelvin waves can modulate ITCZ intraseasonal variability (Guo et al. 2014). ENSO and the Southern Annular Mode (SAM) can also influence the ITCZ on interannual time scales (Münnich and Neelin 2005). The SAM, also known as the Antarctic Oscillation, describes the north–south movement of the westerly wind belt that encircles Antarctica. A negative SAM event reflects an expansion of the westerly winds belt toward the equator, with more abundant midlatitude precipitation in general (see Fig. 6.2c for monthly SAM values in 2020).

A relatively persistent pattern dominated the main South American climate signals for 2020. For most of the year, the South Atlantic was warmer than normal, characterized by moist westerly wind bursts near the equator, affecting the Atlantic ITCZ. Significant anomalies in low-pressure systems dominated the 60°S latitude belt to the southwest of South America, with a corresponding weak South Atlantic anticyclone (Fig. 4.13a). A mostly positive SAM pattern, later reinforced by a rapid transition into La Niña from June onward, further reinforced the pattern above. As a result of this persistence, a large portion of inland Brazil experienced severe precipitation deficits and remarkable anomalous warmth, which escalated from September onward.

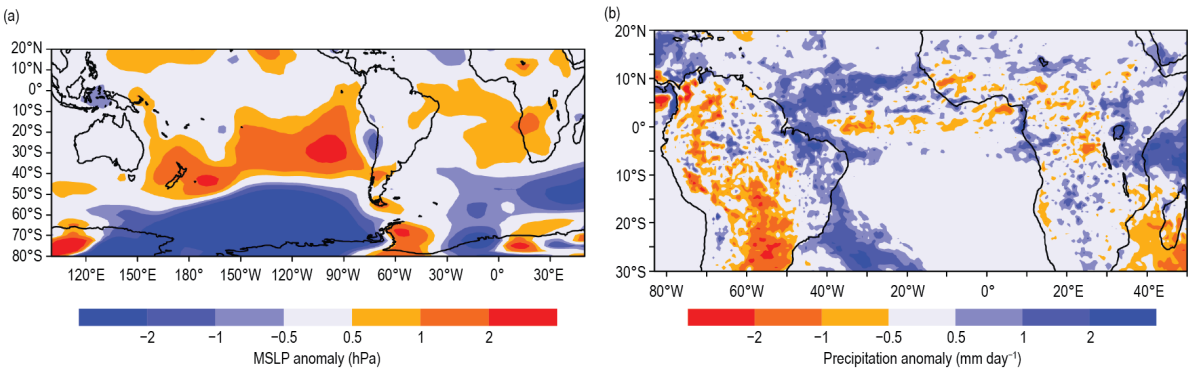

Fig. 4.13. Observed (a) tropical and SH MSLP anomaly (hPa) and (b) precipitation anomaly (mm day^{-1}) for tropical and subtropical South America and Africa for Jan–Dec 2020. MSLP anomalies are calculated with respect to a 1981–2010 climatology derived from the NCEP/NCAR Reanalysis (Kalnay et al. 1996). Precipitation anomalies calculated with respect to a 1998–2019 climatology are derived from CMORPH (Joyce et al. 2004).

In contrast, the Atlantic ITCZ experienced mildly enhanced convective activity south of the equator, with positive rainfall anomalies contrasting with the pattern for the tropics and subtropics (Fig. 4.13b). The ITCZ itself remained centered slightly north of its climatological position for most of the southern rainy season. The Atlantic Index (Pezza and Coelho 2019), as defined by the SST south of the equator minus the SST north of the equator over key areas of influence for the ITCZ, reflected the role of the north–south gradient mechanism for 2020, with the ITCZ tending to shift toward the warmer side of this gradient (Figs. 4.14a,b).

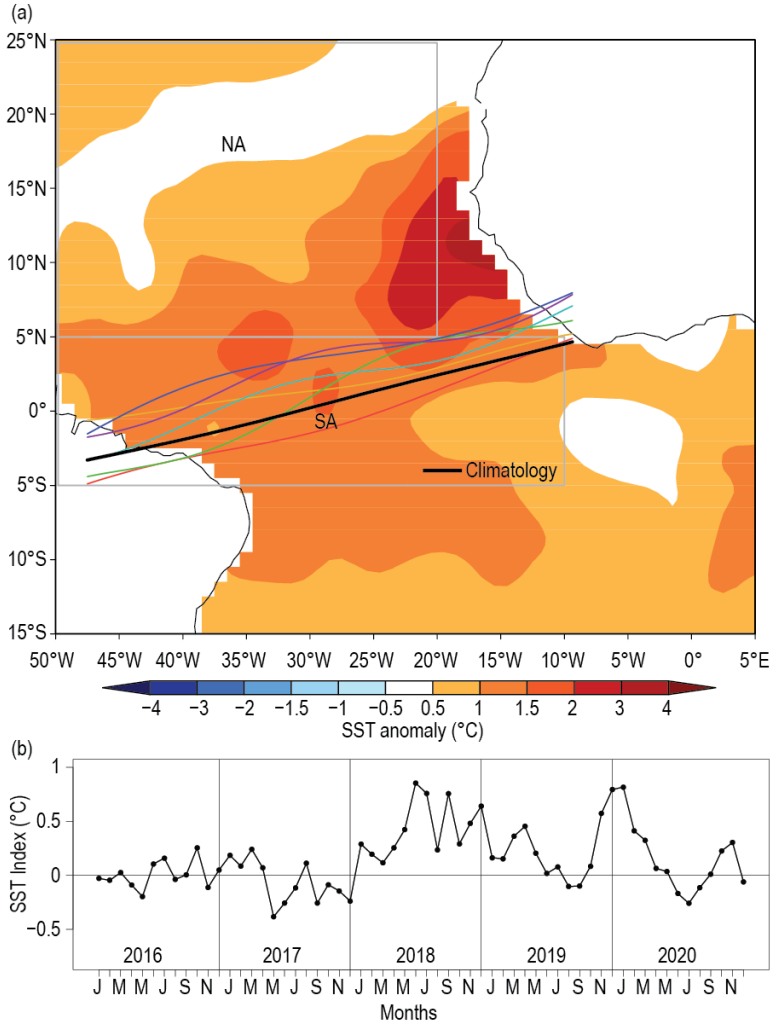

Fig. 4.14. (a) Atlantic ITCZ position inferred from OLR (Liebmann and Smith 1996) during Mar 2020. The colored thin lines indicate the approximate position for the six pentads of the month. The black thick line indicates the Atlantic ITCZ climatological position for Mar. The SST anomalies for Mar 2020 calculated with respect to the 1982–2019 climatology are shaded (°C). The two boxes indicate the areas used for the calculation of the Atlantic index in panel (b), which shows monthly OISST (Smith et al. 2008) anomaly time series averaged over the South Atlantic sector (SA region, 5°S–5°N, 10°–50°W) minus the SST anomaly time series averaged over the North Atlantic sector (NA region, 5°–25°N, 20°–50°W) for the period 2016–20, forming the Atlantic index. The positive phase of the index indicates favorable conditions for enhanced Atlantic ITCZ activity south of the equator.

e. Global monsoon summary—B. Wang and Q. He

The global monsoon is the dominant mode of annual precipitation and circulation variability and is a critical feature of Earth's climate system. The tropical monsoon rainfall domain was first defined by Wang (1994), who showed that a monsoon characterized by a rainy summer and dry winter distinguishes an arid climate (without a rainy season) from equatorial regions where rainfall lacks a significant seasonal cycle. The monsoon domain defined using precipitation characteristics is shown in Fig. 4.15, and consists of eight regional monsoons (Table 4.1). Figure 4.15 also shows global summer precipitation anomalies in the Southern Hemisphere (SH) during November 2019–April 2020 and the Northern Hemisphere (NH) during May–October 2020. Figure 4.16 shows temporal variations of summer monsoon precipitation and low-level circulation indices for each of the eight regional monsoons. The precipitation indices represent the anomalous precipitation rate averaged over the rectangular box regions, including both land and ocean areas shown in Fig. 4.15. Note that the precipitation averaged in each box well represents the precipitation averaged over the corresponding entire regional monsoon domain ($r > 0.90$). The

Table 4.1. Definition of the regional summer monsoon circulation indices and their Pearson correlation coefficients (r) with the corresponding regional summer monsoon precipitation indices for 1979/80–2019/20. All circulation indices are defined by the meridional shear of the zonal wind at 850 hPa (or 700 hPa in highland southern Africa), which measures the intensity (relative vorticity) of the monsoon troughs except for northern African (NAF) and East Asian (EA). The NAF monsoon circulation index is defined by the westerly monsoon strength. The EASM circulation index is defined by the meridional wind strength, which reflects the east–west thermal contrast between the Asian continent and the western North Pacific. The precipitation indices are defined by the areal mean precipitation over the blue box regions shown in Fig. 4.16. The correlation coefficients were computed using monthly time series (164 summer months; June–September in NH [1980–2020] and December–March in SH [1979/80–2019/20]). Bolded numbers represent significance at the 99% confidence level. (Adapted from Yim et al. 2014).

Regional monsoon	Definition of the circulation index	r
Indian (ISM)	U850 (5° –15°N, 40°–80°E) minus U850 (25°–35°N, 70°–90°E)	0.70
Western North Pacific (WNPSM)	U850 (5°–15°N, 100°–130°E) minus U850 (20°–35°N, 110°–140°E)	0.82
East Asian (EASM)	V850 (20°–40°N, 120°–140°E)	0.66
North American (NASM)	U850 (5°–15°N, 130°–100°W) minus U850 (20°–30°N, 110°–80°W)	0.85
Northern African (NAFSM)	U850 (0°–15°N, 60°–10°W)	0.68
South American (SASM)	U850 (20°–5°S, 70°–40°W) minus U850 (35°–20°S, 70°–40°W)	0.81
Southern African (SAFSM)	U700 (15°S-0°, 10°–40°E) minus U700 (25°–10°S, 40°–70°E)	0.63
Australian (AUSSM)	U850 (15°S–0°, 90°–130°E) minus U850 (30°–20°S, 100°–140°E)	0.89

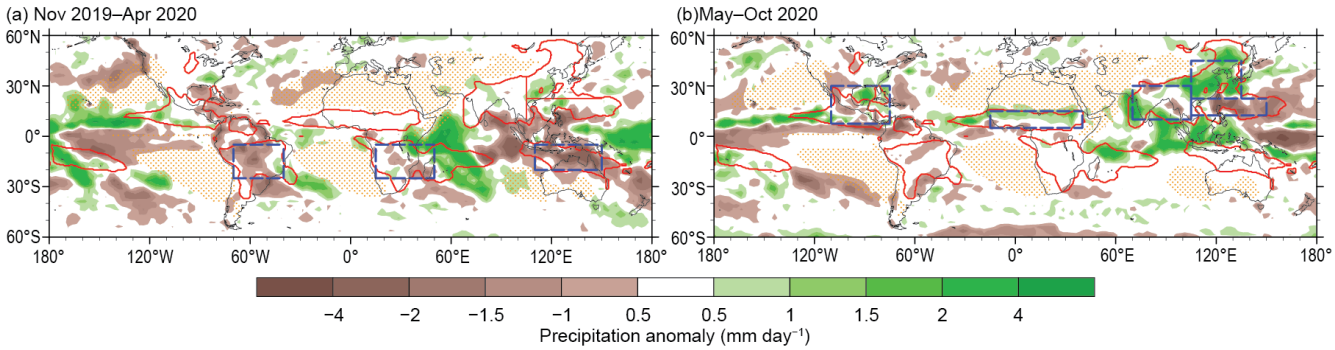

Fig. 4.15. Seasonal mean precipitation anomalies (mm day^{-1}) for (a) the SH summer monsoon season: Nov 2019–Apr 2020 and (b) the NH summer monsoon season: May–Oct 2020. Red lines outline the global monsoon precipitation domain. The monsoon domain is defined by (1) the annual range (local summer minus winter) where precipitation exceeds 300 mm and (2) the summer mean precipitation is >55% of the total annual precipitation amount, where summer is defined to be May–Sep for the NH and Nov–Mar for the SH (Wang and Ding 2008). The dotted area represents the dry region where the local summer precipitation rate is below 1 mm day^{-1}. Precipitation indices for each regional monsoon are defined by the areal mean precipitation in the corresponding rectangular regions (dashed blue), which are highly correlated with the precipitation averaged over the corresponding real regional monsoon domains. Rainfall data were taken from the GPCP (Huffman et al. 2009).

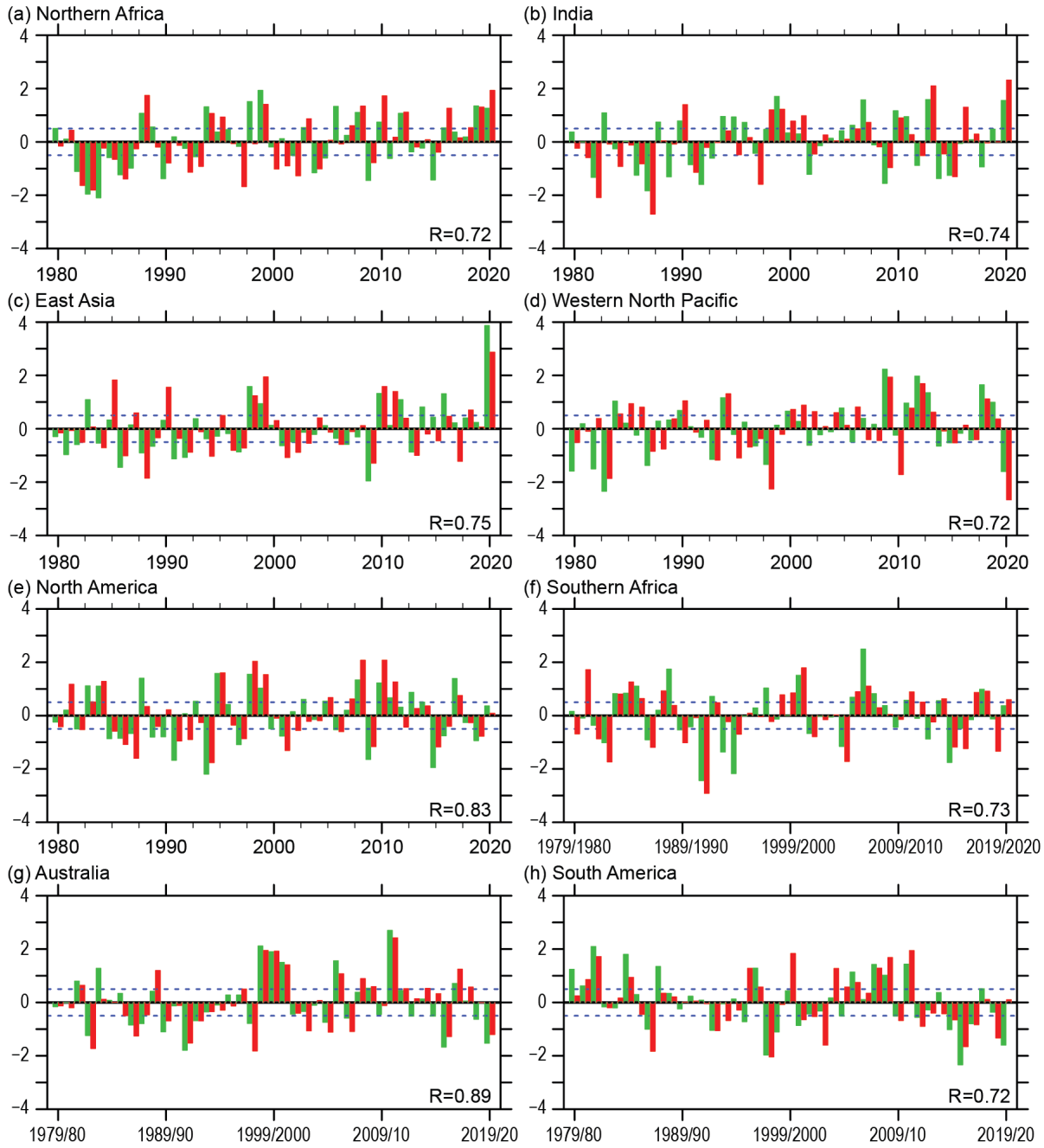

Fig. 4.16. (a)–(h) Normalized summer mean precipitation (green) and circulation (red) indices for each of the eight regional monsoons (Table 4.1). Indices were normalized by their corresponding standard deviation. Numbers shown in each panel's bottom right denote the correlation coefficient between the seasonal mean precipitation and circulation indices (sample size: 41). Dashed lines indicate ±0.5 std. dev. The monsoon seasons are May–Oct for the NH and Nov–Apr for the SH. (Data source: GPCP for precipitation and ERA-5 [Hersbach et al. 2020] for circulation.)

definitions of the circulation indices for each monsoon region are provided in Table 4.1. The precipitation and circulation indices are well-correlated in most regional monsoons, with correlation coefficients ranging from 0.63 to 0.89 with a sample size of 164 summer months (Table 4.1). The precipitation and circulation indices together provide consistent measurements of the strength of each regional monsoon system.

Total seasonal rainfall over the NH monsoon region over land was the highest since the start of the record in 1980 (Fig. 4.17). It was largely driven by the 2020 East Asian summer monsoon (EASM), which was nearly 4 standard deviations above average (Fig. 4.16c). The Meiyu season (July–August), a typical rainy season over the Yangtze and Huaihe River Valleys (YHRV) of China, doubled its climatological mean duration by 2 months in 2020. The May–October

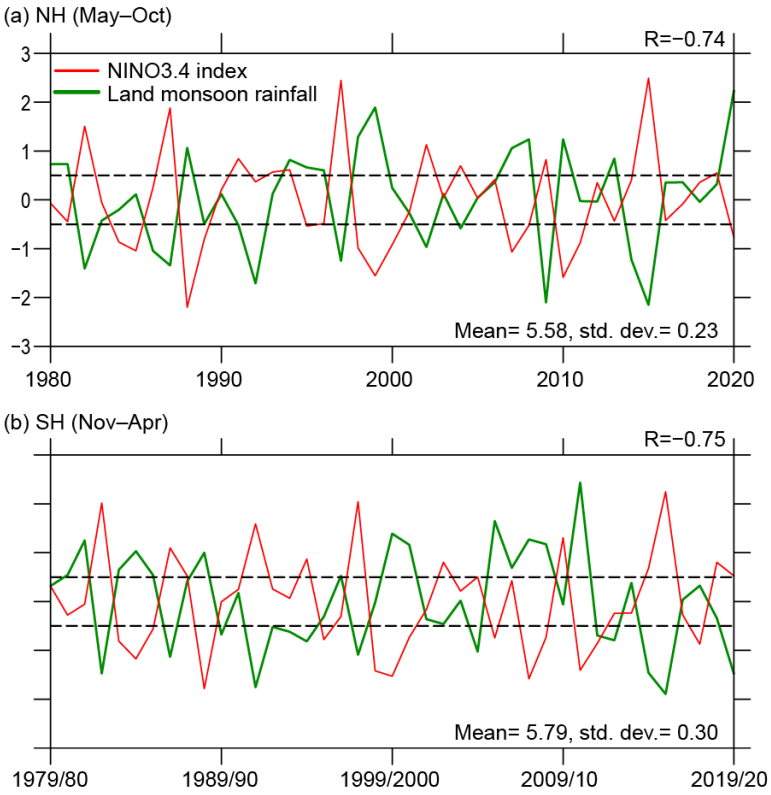

Fig. 4.17. (a) NH summer (May–Oct) land monsoon precipitation anomaly (green) normalized by its standard deviation. The climatological mean NH summer land monsoon precipitation (Mean) and standard deviation (SD) are shown in the lower right panel (mm day^{-1}). Numbers shown in each panel's top right denote the correlation coefficient between the seasonal mean precipitation anomaly and the simultaneous Niño-3.4 index (red). Dashed lines indicate ±0.5. (b) As in (a) except for the SH summer (Nov–Apr). Note that the land monsoon precipitation excludes the monsoon rainfall over the oceanic monsoon domain. (Data source: GPCP for precipitation, HadISST and ERSSTv5 for SST.)

accumulated rainfall averaged over the YHRV exceeded 750 mm, the most since the start of the record in 1961 (Qiao et al. 2021). Associated severe flooding affected about 45.5 million people and caused a direct economic loss of more than 100 billion Chinese Yuan ($15.5 billion [U.S. dollars]; Wei et al. 2020; see section 7g for more details).

During the 2019/20 SH summer monsoon season (November–April), precipitation over the Maritime Continent–Australian and South American monsoon regions was substantially suppressed, while rainfall in the equatorial central Pacific and the western Indian Ocean was markedly enhanced (Fig. 4.15a). This contrast is due to the anomalous Walker circulation associated with the warm Central Pacific sea surface temperature (SST) anomalies even though they did not reach the thresholds for El Niño. The Indian Ocean rainfall anomalies were also driven by a positive phase of the Indian Ocean dipole (IOD; Saji et al. 1999) SST anomaly, which was +1.8°C during SH summer. The Australian summer monsoon produced precipitation 1.5 standard deviations below normal, with an associated reduced circulation intensity (Fig. 4.16g). The South American monsoon region also received precipitation 1.5 standard deviations below normal, although the corresponding circulation's strength was near normal (Fig. 4.16h). Southern African summer monsoon precipitation and circulation intensity were normal (Fig. 4.16f) due to a dipolar structure in eastern Africa (increased rainfall in equatorial East Africa and decreased rainfall near Madagascar). The increased eastern African rainfall was largely caused by the positive phase of the IOD SST anomaly experienced from November 2019 to April 2020. During November 2019–April 2020, the IOD index is 1.82 standard deviations or 0.34°C (not shown). In fact, November 2019–April 2020 was the second-highest such period of the IOD index. Overall, the SH summer monsoon showed a consistent reduction of precipitation and weakening of the monsoon circulation, although there were various degrees of weakening in the three SH regional monsoons.

During the 2020 NH summer monsoon season (May–October), precipitation over the Maritime Continent was significantly above normal due to the rapidly developing La Niña, while there was a noticeable reduction of precipitation in the equatorial Pacific Ocean and the Philippine Sea (Fig. 4.15b). In addition to the unprecedented EASM strength, the summer precipitation over both the Indian and northern African monsoon regions were also ~1.5 standard deviations above normal, and the corresponding circulation intensity was >2 standard deviations above average (Figs. 4.16a,b). The North American monsoon was characterized by near-normal precipitation and circulation intensity (Fig. 4.16e), and the western North Pacific monsoon precipitation, which is generally out of phase with the EASM, was about 1.5 standard deviations below normal (Fig. 4.16d).

Monsoon rainfall over land has more significant socio-economic impacts than monsoon rainfall over the ocean. Therefore, we specifically examine land monsoon rainfall. Global land monsoon precipitation is strongly influenced by tropical SST anomalies, especially related to El Niño–Southern Oscillation (ENSO; Wang et al. 2012). Figure 4.17 highlights that both NH and SH land summer monsoon precipitation are well correlated with the simultaneous Niño-3.4, suggesting that ENSO explains about 50% of their variance. Figure 4.17 shows that the total amount of 2020 NH land monsoon precipitation was the highest of any monsoon season in the record that dates to 1980, whereas the 2019/20 SH land monsoon precipitation was below normal. However, the 2020 La Niña cannot fully explain the record high NH land monsoon precipitation nor the EASM extreme. Further study of the causes is warranted.

f. Indian Ocean dipole and unique Indian Ocean basin warming in 2020—L. Chen and J.-J. Luo

Year-to-year climate variability in the tropical Indian Ocean (IO), which is largely driven by local air–sea interactions and the El Niño–Southern Oscillation in the tropical Pacific, exerts great influence on weather and climate in the regions surrounding the IO (e.g., Saji et al. 1999; Luo et al. 2010; Xie et al. 2016). Among them, the Indian Ocean dipole (IOD; Saji et al. 1999) is an inherent air–sea coupled mode in the tropical IO. The IOD usually starts to grow in boreal summer, peaks in autumn, and terminates rapidly in early boreal winter in connection with the reversal of monsoonal winds along the west coast of Sumatra. As shown in Figs. 4.18a,b, a strong positive IOD event, with anomalously warm waters to the west and anomalously cool waters to the east, occurred in 2019 and was of an extreme intensity in the boreal fall of 2019 (Chen et al. 2020).

Throughout 2020, the IOD index (also known as the Dipole Mode Index) was near zero, indicating a neutral IOD status in 2020 (Fig. 4.18b). In the tropical IO, the most remarkable feature was that sea surface temperatures (SSTs) exhibited warm anomalies over the entire tropical IO throughout 2020 (Fig. 4.18c, Figs. 4.19a–d). Following the early boreal winter of 2019/20, the extreme positive IOD event rapidly terminated and then the tropical IO turned into an Indian Ocean basin (IOB) mode (Figs. 4.18b,c). The IOB, characterized by a basin-wide warming or cooling, is one of two dominant modes of SST anomalies in the tropical IO, and the other is IOD. In March–May 2020, above-average SST anomalies were observed over the tropical IO, and positive precipitation anomalies dominated the

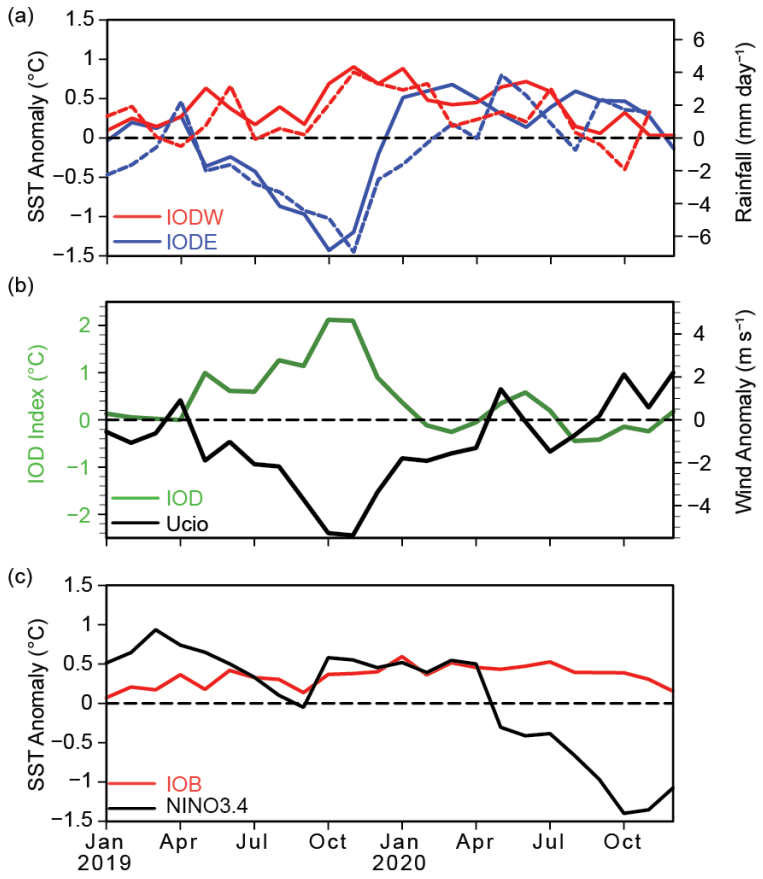

Fig. 4.18. (a) Monthly anomalies of SST (°C; solid lines) and precipitation (mm day^{-1}; dashed lines) for the eastern pole (IODE; 10°S–0°, 90°–110°E; blue lines) and the western pole (IODW; 10°S–10°N, 50°–70°E; red lines) of the IOD. (b) As in (a), but for the IOD index (measured by the SST difference between the IODW and IODE, green line) and surface zonal wind anomaly (m s^{-1}) in the central equatorial IO (Ucio; 5°S–5°N, 70°–90°E; black line). (c) As in (a), but for SST anomalies in the Niño-3.4 region (5°S–5°N, 170°–120°W; black line) and the tropical IO (IOB; 20°S–20°N, 40°–100°E; red line). Anomalies are relative to the 1982–2020 base period. (Sources: NOAA OISST [Reynolds et al. 2002]; monthly GPCP precipitation analysis [available at http://precip.gsfc.nasa.gov/]; and JRA-55 atmospheric reanalysis [Ebita et al. 2011].)

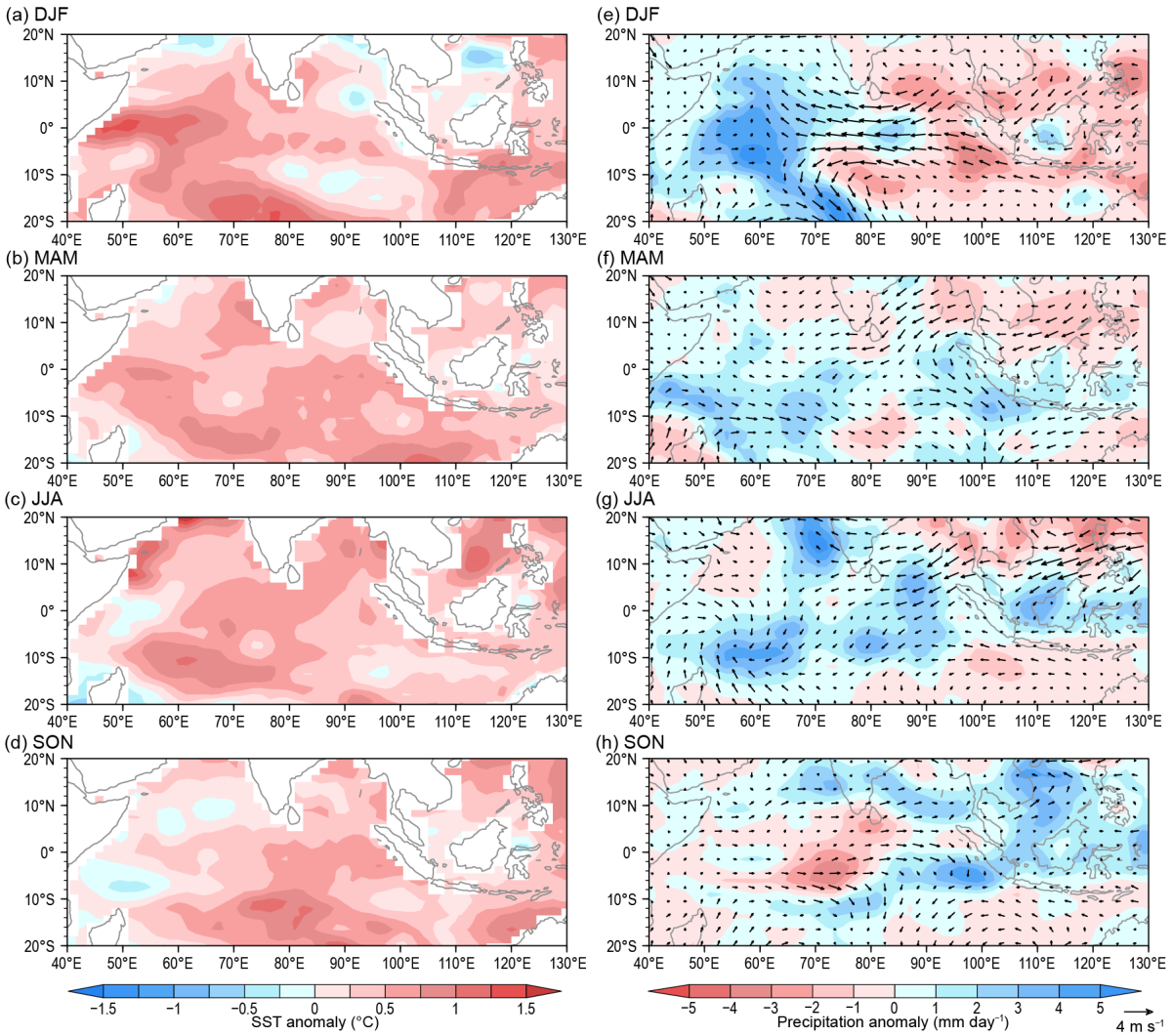

Fig. 4.19. (a)–(d) SST (°C, colored scales) anomalies during (a) Dec–Feb 2019/20, (b) Mar–May 2020, (c) Jun–Aug 2020, and (d) Sep–Nov 2020. (e)–(h) As in (a)–(d), but for precipitation (mm day^{-1}; °C, colored scales) and surface wind anomalies (vector). Anomalies were calculated relative to the climatology over the period 1982–2020. (Sources: NOAA OISST [Reynolds et al. 2002]; monthly GPCP precipitation analysis [available at http://precip.gsfc.nasa.gov/]; and JRA-55 atmospheric reanalysis [Ebita et al. 2011].)

equatorial IO (Figs. 4.19b,f). Given that there was more above-average precipitation occurring in the Southern Hemisphere compared to the Northern Hemisphere, the central and eastern equatorial IO were dominated by anomalous cross-equatorial northerly winds (Fig. 4.19f). During June–August, the above-average SSTs and above-average precipitation persisted in the tropical IO, and easterly anomalies occurred in the central and eastern equatorial IO (Figs. 4.19c,g). During September–November (SON), the above-average SSTs continued over the entire tropical IO, but there was a weak zonal gradient with larger SST anomalies in the eastern equatorial IO and smaller SST anomalies in the western equatorial IO (Figs. 4.19d,h). This weak zonal gradient of SST anomalies corresponded to a marginally negative value of IOD index in SON 2020 (Fig. 4.18b). Concurrently, the precipitation anomalies exhibited a dipole pattern with dry conditions in the western equatorial IO and wet conditions in the eastern equatorial IO. These conditions corresponded with westerly wind anomalies in the central equatorial IO (Fig. 4.19h).

On the other hand, the tropical Pacific had a prolonged weak El Niño-like warming status from winter 2018/19 to winter 2019/20 (Fig. 4.18c). The weakly positive Niño-3.4 index declined as SSTs cooled and became negative in May 2020. Then, a La Niña event rapidly developed throughout the remainder of 2020, maturing to a moderate status by the end of the year. Previous studies have suggested that in response to a preceding El Niño event, the IO tends to exhibit anomalous

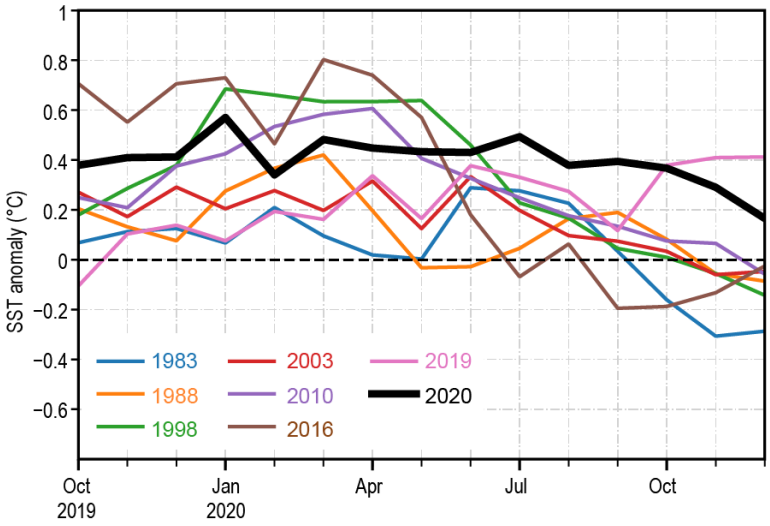

Fig. 4.20. Evolution of monthly SST anomalies averaged in the tropical IO (IOB; 20°S–20°N, 40°–100°E). The bold black curve indicates the IOB event in 2020 and the other curves indicate the other positive IOB events since 1980. (Source: NOAA OISST [Reynolds et al. 2002].)

basin-wide warming in the following year (Yang et al. 2007; Xie et al. 2016). However, there is not robust evidence to determine whether the weak El Niño in 2019/20 winter made a contribution to the long-lasting IOB mode in 2020.

The IO basin-wide anomalous warmth that dominated throughout 2020 differs from the majority of positive IOB events. The typical IOB event usually peaks in late boreal winter and early spring, and persists through boreal summer (Yang et al. 2007). The evolution of all of the positive IOB events since 1980 are displayed in Fig. 4.20. Most of the positive IOB events tend to peak in the first half of the year, then rapidly decay in the second half. In contrast, the basin-wide warming in 2020 did not begin declining until November, presenting a unique, long-lasting IOB event in 2020. Such a unique event in 2020 may be traced back to the continuous enhancement of the tropical IO warming trend during recent decades (Luo et al. 2012).

In summary, the IOD index exhibited a neutral status in 2020. A marked basin-wide anomalously warm SST pattern persisted throughout 2020, indicating that the IOB mode dominated in 2020. This unique IOB event in 2020 differed from most of the past positive IOB events, indicating that the long-lasting IO basin-wide warming of 2020 may be attributed to the long-term warming trend of SST in the IO (Luo et al. 2012).

g. Tropical cyclones

1) Overview—H. J. Diamond and C. J. Schreck

The International Best Track Archive for Climate Stewardship (IBTrACS) dataset comprises historical tropical cyclone (TC) best-track data from numerous sources around the globe, including all of the World Meteorological Organization (WMO) Regional Specialized Meteorological Centers (RSMCs; Knapp et al. 2010). This dataset represents the most complete compilation of global TC data. From these data, Schreck et al. (2014) compiled 1981–2010 climatological values of TC activity for each basin using statistics from both the WMO RSMCs and the Joint Typhoon Warning Center (JTWC). These values are referenced in each subsection.

Tallying the global TC numbers is challenging and involves more than simply adding up basin totals, because some storms cross TC basin boundaries, some TC basins overlap, and multiple agencies track and categorize TCs. Global metrics and Northern Hemisphere (NH) basins are typically measured from January to December while Southern Hemisphere (SH) basins are typically measured from July to June. Compiling the activity using preliminary data from NOAA's National Hurricane Center and the JTWC over all seven TC basins as archived in IBTrACS (Fig. 4.21), the 2020 calendar year had 102 (per Table 4.2) named storms (sustained wind speeds ≥ 34 kt or 17 m s–1), which is six more than last season (2019; Diamond and Schreck 2020) and well above the 1981–2010 average of 85 (Schreck et al. 2014). This year also featured 46 hurricanes/typhoons/cyclones (HTCs; sustained wind speeds ≥ 64 kt or 33 m s^{-1}), which is equal to the climatological average (Schreck et al. 2014). During 2020, 22 storms reached major HTC status (sustained wind speeds ≥ 96 kt or 49 m s^{-1}), which is just above the long-term average of 21 and 10 fewer than the 2019 season (Diamond and Schreck 2020). The Accumulated Cyclone Energy (ACE) for the season

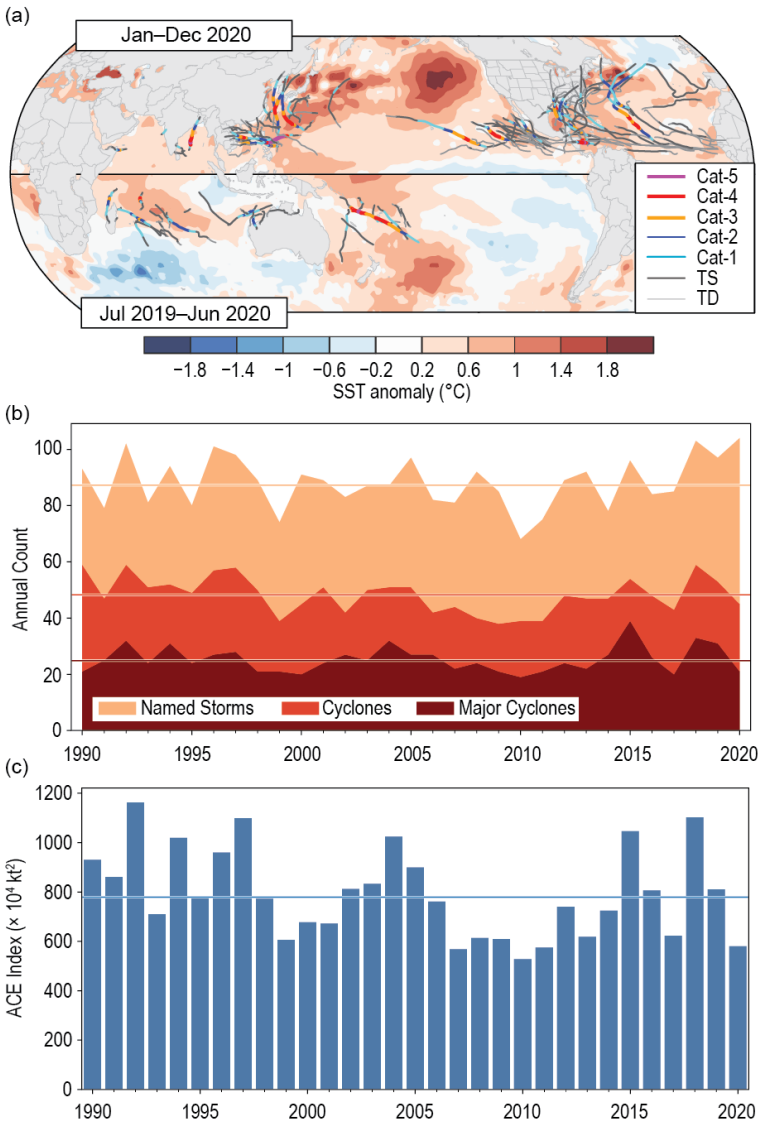

Fig. 4.21. (a) Global summary of TC tracks overlaid on associated OISST anomalies (°C; Reynolds et al. 2002) for the 2020 season relative to 1982–2010; (b) global TC counts; and (c) global ACE values. Horizontal lines on (b) and (c) are 1981–2010 normals.

was 574 × 10^4 kt^2, which would put it in the lowest 10% of years from 1981–2010 and considerably less than the value of 795 × 10^4 kt^2 in 2019 (Diamond and Schreck, 2019).

In sections 4g2–4g8, 2019/20 (SH) and 2020 (NH) seasonal TC activity is described and compared to the historical record for each of the seven WMO-defined TC basins. For simplicity, all counts are broken down by the U.S. Saffir-Simpson Hurricane Wind Scale (SSHWS). The overall picture of global TCs during 2020 is shown in Fig. 4.21. Actual counts by category are documented in Table 4.2.

Globally, three storms during the year reached SSHWS Category 5 strength (sustained wind speeds ≥ 137 kt or 70.5 m s^{-1}). This was three fewer than recorded in 2016 (Diamond and Schreck 2017), and two less than recorded in 2017 and 2019 (Diamond and Schreck 2018; 2020). The all-time record of 12 Category 5 global TCs was set in 1997 (Schreck et al. 2014),[3] while 11 Category 5 global TCs were recorded in 2018.

The three Category 5 storms in 2020 were: Super Typhoon Goni in the western North Pacific, Cyclone Amphan in the North Indian Ocean, and Tropical Cyclone Harold in the southwest Pacific. Despite only reaching Category 4 status, Iota caused devastating damage to the nations of Central America, especially Nicaragua and Honduras, that was exacerbated by the landfall of Category 4 Eta only 2 weeks prior to Iota in essentially the same area. Super Typhoon Goni was the strongest TC to make landfall in the historical record and led to almost 1 million people being evacuated from its path and thousands of homes destroyed. Super Cyclone Amphan caused $13.9 billion (U.S. dollars) in damage and resulted in over 100 fatalities, primarily in India. Harold had major impacts in the southwest Pacific, particularly in Vanuatu and the Solomon Islands. Of note, a fourth Category 5 storm, Yasa, formed in the Southwest Pacific in December 2020. While forming in 2020, this storm is part of the July–June 2020/21 tropical cyclone season and thus will be discussed in detail in next year's report. Sidebar 4.1 details the record-setting and devastating local impacts of Category 4 Hurricane Laura in Louisiana.

Finally, and while not an official TC basin, three significant TC-like storms or "medicanes" were recorded within the Mediterranean Sea in September, November, and December, affecting Greece, Tunisia, and Syria/Lebanon, respectively. Sidebar 4.2 focuses on these storms.

[3] SSHWS is based on 1-minute averaged winds, and the categories are defined at: https://www.weather.gov/mfl/saffirsimpson; the Australian category scale is based on 10-minute averaged winds, and those categories are defined at: https://australiasevereweather.com/cyclones/tropical_cyclone_intensity_scale.htm

Table 4.2. Global counts of TC activity by basin for 2020. "+" denotes top tercile; "++" is top 10%; "-" is bottom tercile; "--" is bottom 10% (all relative to 1981–2010). "+++" denotes record values for the entire IBTrACS period of record. (Note that some inconsistencies between Table 4.2 and the text of the various basin write-ups in section g exist and are unavoidable, as tallying global TC numbers is challenging and involves more than simply adding up basin totals, because some storms cross TC basin boundaries, some TC basins overlap, and multiple agencies are involved in tracking and categorizing TCs.)

Basin	TCs	HTCs	Major HTCs	SS Cat 5	ACE ($\times 10^4$ kt^2)
North Atlantic	30 +++	14 ++	7 ++	0	180 +
Eastern Pacific	17	4 −−	3	0	77 −
Western Pacific	23 −	12 −	7 −	1	150 −−
North Indian	5 +	4 ++	2 ++	1 ++	27 +
South Indian	11 +	6	3	0	54 −
Australia	10	3 −	0	0	31 −
Southwest Pacific	9	5 +	1	1 ++	56
Global Totals	**102** ++	**48**	**23**	**3**	**574** −−

2) Atlantic basin—G. D. Bell, M. Rosencrans, E. S. Blake, C. W. Landsea, H. Wang, S. B. Goldenberg, and R. J. Pasch

(I) 2020 SEASONAL ACTIVITY

The 2020 Atlantic hurricane season produced 30 named storms, of which 14 became hurricanes and seven of those became major hurricanes (Fig. 4.22a). The Hurricane Database 2 (HURDAT2; Landsea and Franklin, 2013) 1981–2010 seasonal averages (included in IBTrACS) are 12.1 named storms, 6.4 hurricanes, and 2.7 major hurricanes (Landsea and Franklin 2013). The 30 named storms during 2020 surpasses the previous record of 28 set in 2005. The 14 hurricanes during 2020 are the second most on record behind 15 observed in 2005, seven major hurricanes tied with 2005 for the most on record.

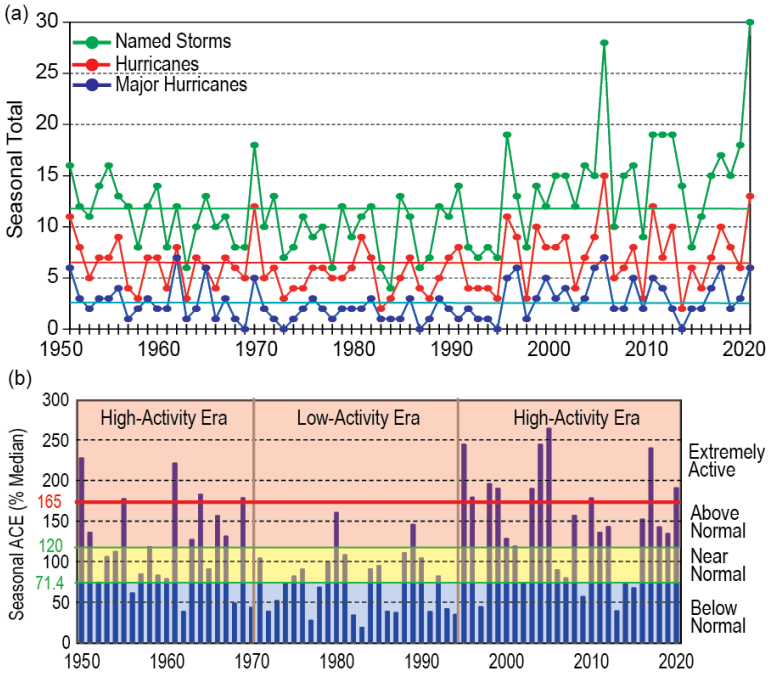

Fig. 4.22. Seasonal North Atlantic hurricane activity during 1950–2020. (a) Numbers of named storms (green), hurricanes (red), and major hurricanes (blue). (b) The ACE index expressed as percent of the 1981–2010 median value. ACE is calculated by summing the squares of the 6-hourly maximum sustained surface wind speed (kt) for all periods while the storm is at least tropical storm strength. Red, yellow, and blue shadings correspond to NOAA's classifications for above-, near-, and below-normal seasons, respectively (http://www.cpc.ncep.noaa.gov/products/outlooks/background_information.shtml). The thick red horizontal line at 165% of the median ACE value denotes NOAA's threshold for an extremely active season. Vertical brown lines separate high- and low-activity eras. Note that there is a low bias in activity during the 1950s to the early 1970s due to the lack of satellite imagery and a technique (Dvorak) to interpret tropical cyclone intensity for systems over the open ocean. (Source: HURDAT2 [Landsea and Franklin 2013].)

Nine of 30 named storms during 2020 were short-lived (≤2 days). There has been a large artificial increase (approximately five per year) in these "shorties" since 2000 (Landsea et al. 2010). These increased counts primarily reflect new observational capabilities such as scatterometers, Advanced Microwave Sounding Units, and the Advanced Dvorak Technique, and have no association with any known climate variability (Villarini et al. 2011).

The 2020 seasonal ACE value (Bell et al. 2000) was 191.5% of the 1981–2010 median (which is 92.4×10^4 kt^2; Fig. 4.22b). This value is the sixth largest since 1970 and is above NOAA's threshold for both an above-normal (120%) and an extremely active (165%) season. There have now been a record five consecutive above-normal seasons, which surpasses the previous record of four set in 1998–2001. Since the current Atlantic high-activity era began in 1995 (Goldenberg et al. 2001; Bell et al. 2019, 2020), there have been 18 above-normal seasons, with 10 being classified as extremely active. By comparison, the preceding 24-year low-activity era of 1971–94 had only two above-normal seasons, and none were extremely active.

(II) STORM FORMATION TIMES, REGIONS, AND LANDFALLS

Substantial TC activity occurred throughout the 2020 hurricane season (Fig. 4.23a). May–July saw a record nine named storms. Seven of those, of which four were "shorties," formed in the extratropics from pre-existing extratropical disturbances. On average, 1–2 named storms form per year during this period.

August–October (ASO), typically the most active part of the hurricane season, featured 18 named storms during 2020, with a record 10 forming in September. Ten of the 18 named storms became hurricanes, and four of those became major hurricanes. Most of these storms (13 of 18) formed in the Main Development Region (MDR, green box in Fig. 4.23c), which is also typical of an above-normal season. The MDR spans the tropical North Atlantic Ocean and Caribbean Sea between 9.5°N and 21.5°N (Goldenberg and Shapiro 1996; Goldenberg et al. 2001; Bell and Chelliah 2006; Bell et al. 2017, 2018, 2019). November 2020 saw three named storms, with two becoming major hurricanes over the western Caribbean Sea and striking Nicaragua as Category 4 storms, and generated the second-most Atlantic ACE on record (36×10^4 kt^2), trailing only 1932 (71×10^4 kt^2). On average, November sees only one named storm every other year. Only five major hurricanes have occurred in November in the previous 70 years (1950–2019), and 2020 had two.

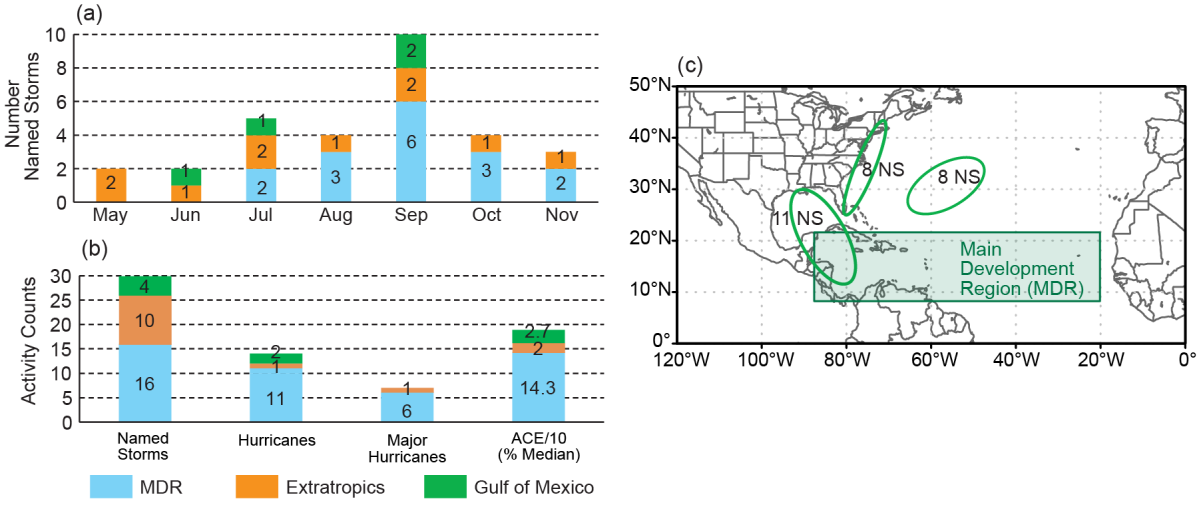

Fig. 4.23. Atlantic TC activity in 2020: (a, b) Storm counts and (c) areas of increased track density. In (a), named storm counts are shown for the month and region the storm was first named. In (b), total seasonal counts for the three storm classifications and ACE are shown for each region where the storm was first named. ACE reflects the entire storm ACE and is attributed to the region in which the storm was first named. Regions in (a, b) are indicated by the color bar below panel (b). In (c), areas of increased track density are shown by green ovals, and the number of named storms that passed through each region are indicated. The Atlantic MDR is shown by the green box. The "extratropics" includes all regions except for the MDR and Gulf of Mexico. (Source: HURDAT2 [Landsea and Franklin 2013].)

Historically, above-normal seasons result from a sharp increase in the number, intensity, and duration of storms that develop in the MDR. During the 2020 season, 16 of the 30 named storms formed in the MDR (Fig. 4.23b) and accounted for 10 of the season's 14 hurricanes and five of the season's seven major hurricanes. The associated MDR-related ACE value was 143% of the median and far exceeds the ACE of 27% associated with storms first named over the Gulf of Mexico and 20% for storms from the extratropics. This MDR-related ACE value was comparable to the 1981–2010 MDR average for above-normal seasons of 155% of the median. These values are roughly 10 times higher than the MDR average of 15.8% for below-normal seasons (Bell et al 2011).

The actual storm tracks during 2020 (not shown) showed three main regions of exceptionally high track density (Fig. 4.23c). One region extended from the western Caribbean Sea to the central U.S. Gulf Coast experiencing 11 named storms with nine as hurricanes and four of those as major hurricanes. Another region extended along the U.S. Atlantic Coast, with eight named storms, one of which became a hurricane. A third region covered the west-central North Atlantic, also with eight named storms, three of which became hurricanes and two of those became major hurricanes.

The season's storm tracks resulted in a record 12 landfalling storms in the continental United States. Six struck as hurricanes, including five as Category 1–2 storms and one as a Category 4 major hurricane (Hurricane Laura in Louisiana). Regionally, nine named storms (including four Category 1–2 hurricanes and Hurricane Laura) made landfall along the Gulf Coast. Louisiana alone experienced a record five landfalling storms, with two striking as Category 1–2 hurricanes (Delta and Zeta) and Category 4 Hurricane Laura. The U.S Atlantic Coast experienced three landfalling storms, including Category 1 Hurricane Isaias. Elsewhere, two hurricanes (Delta and Zeta) made landfall in Mexico, two major hurricanes (Eta and Iota) made landfall in Nicaragua, and one hurricane (Nana) made landfall in Belize.

(III) SEA SURFACE TEMPERATURES

Four main sea surface temperature (SST) signals were present during ASO 2020 (Fig. 4.24). First, SSTs were above average throughout the MDR (Fig. 4.24a), and the area-averaged SST anomaly was +0.6°C (Fig. 4.24b). The largest anomalies were observed throughout the Caribbean Sea and ranged from +0.5° to +1.0°C. Second, the area-averaged SST anomaly in the MDR was also higher (by 0.35°C) than that of the remainder of the global tropics (Fig. 4.24c). This signal typifies the warm phase of the Atlantic Multi-decadal Oscillation (AMO; Enfield and Mestas-Nuñez 1999; Bell and Chelliah 2006) and is a ubiquitous characteristic of Atlantic high-activity eras such as 1950–70 and 1995–present (Goldenberg et al. 2001; Vecchi and Soden 2007; Bell et al. 2018).

The third SST signal during ASO 2020 reflected above-average temperatures across most of the North Atlantic Ocean. Outside of the MDR, the largest anomalies (exceeding +1.5°C) occupied the western and portions of the central North Atlantic (Fig. 4.24a), where numerous tropical storms and hurricanes tracked across this region. The area-averaged SST anomaly in the western North Atlantic (red box, Fig. 4.24a) was +0.91°C and reflected a continuation of exceptional warmth that began in 2014 (Fig. 4.24d).

The fourth SST signal during ASO 2020 was the development of La Niña (section 4b). As discussed below, La Niña contributed to the extensive hurricane activity from September onward.

(IV) ATMOSPHERIC CONDITIONS

Climatologically, the ASO peak in Atlantic hurricane activity largely reflects the June–September peak in the West African monsoon. The inter-related circulation features of an enhanced monsoon increase hurricane activity, while those of an anomalously weak monsoon suppress it (Gray 1990; Hastenrath 1990; Landsea et al. 1992; Bell and Chelliah 2006; Bell et al. 2018, 2020). The association on multi-decadal time scales between the AMO and Atlantic hurricane activity largely exists because of their common relationship with the West African monsoon (Bell and Chelliah 2006).

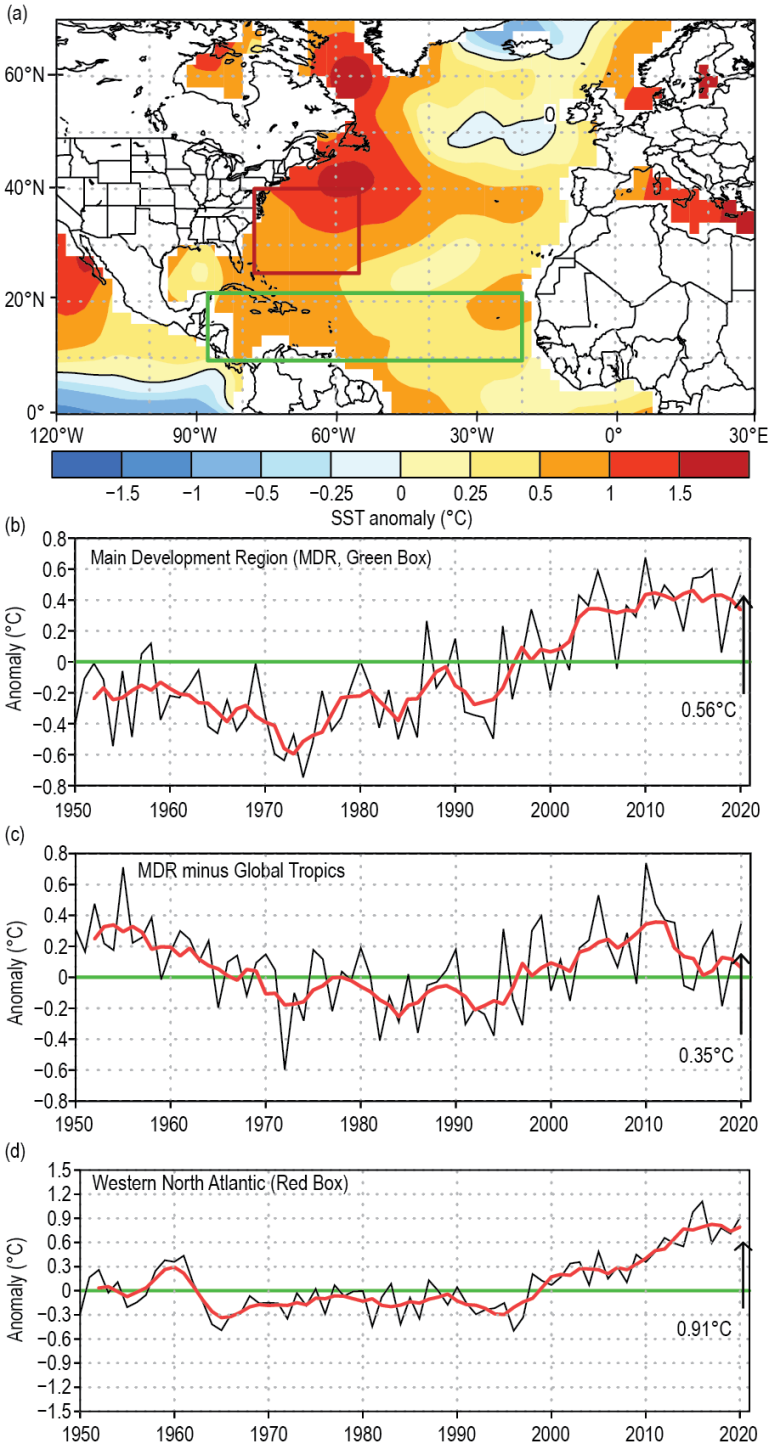

Fig. 4.24. (a) Aug–Oct 2020 SST anomalies (°C). (b)–(d) Time series of Aug–Oct area-averaged SST anomalies (black) and 5-point running mean of the time series (red), (b) in the MDR (green box in (a) spanning 20°–87.5°W and 9.5°–21.5°N), (c) difference between the MDR and the global tropics (20°S–20°N), and (d) in the western North Atlantic (red box in (a) spanning 55°–77.5°W and 25°–40°N). Anomalies are departures from the 1981–2010 period means. (Source: ERSST-v5 [Huang et al. 2017].)

The West African monsoon was enhanced during July–September 2020, as indicated by negative outgoing longwave radiation (OLR) anomalies across the African Sahel (red box, Fig. 4.25a). Total OLR values in this region averaged 234 W m^{-2} (Fig. 4.25b), with values less than 240 W m^{-2}, indicating deep tropical convection. Consistent with these conditions, the larger-scale divergent circulation at 200-hPa featured an extensive area of anomalous divergence and a core of negative velocity potential anomalies across subtropical northern Africa (Fig. 4.25c). The OLR time series shows that an enhanced monsoon has largely prevailed throughout the current Atlantic high-activity era and warm AMO of 1995–present (Fig. 4.25b). By contrast, a much weaker monsoon with OLR values well above 240 W m^{-2} in the Sahel region was typical of the low-activity and cool AMO period of the 1980s and early 1990s.

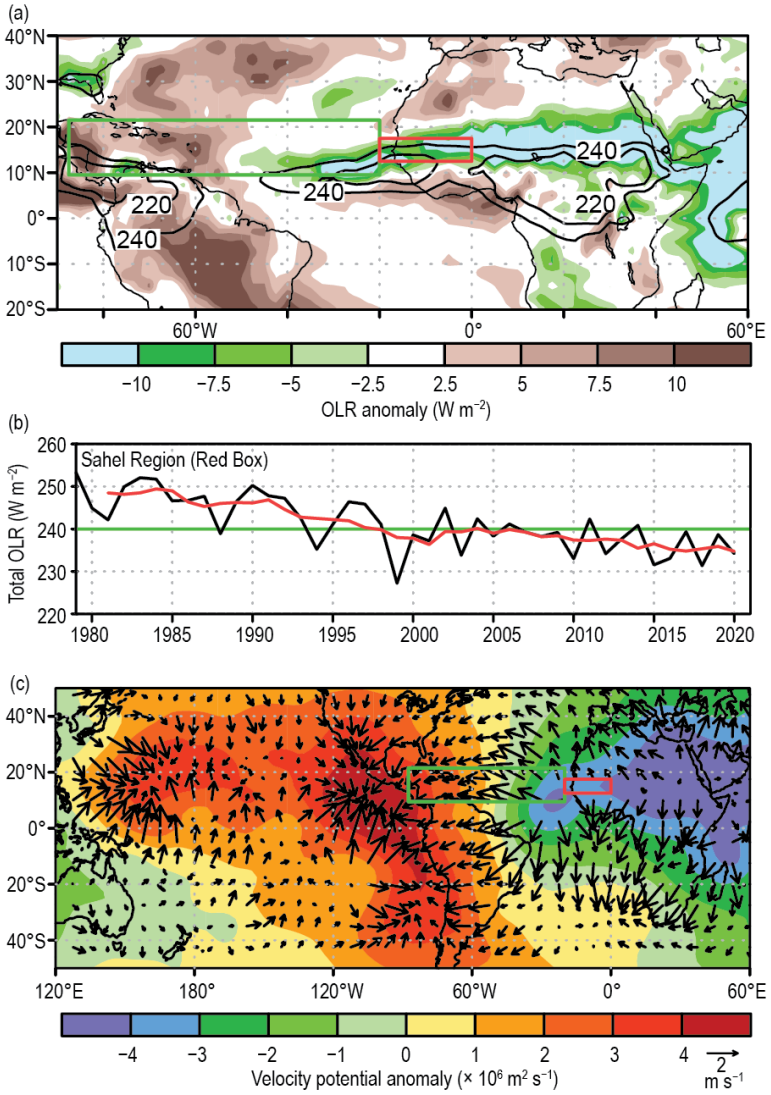

Fig. 4.25. (a) Jul–Sep 2020 anomalous OLR (W m^{-2}), with negative (positive) values indicating enhanced (suppressed) convection. (b) Time series of Jul–Sep total OLR (black) and 5-point running mean of the time series (red) averaged over the African Sahel region (red box in (a), (c) spanning 20°W–0° and 12.5°–17.5°N). (c) Jul–Sep 2020 anomalous 200-hPa velocity potential (× 10^6 m^2 s^{-1}) and divergent wind vectors (m s^{-1}). In (a), contours show total OLR values of 220 W m^{-2} and 240 W m^{-2}. In (a), (c), the green box denotes the Atlantic MDR. Anomalies are departures from the 1981–2010 means. (Source: NCEP/NCAR Reanalysis [Kalnay et al. 1996] for velocity potential and wind, and Liebmann and Smith [1996] for OLR.)

During ASO 2020, core atmospheric conditions within the MDR reflected a combination of the enhanced West African monsoon and La Niña. At 200 hPa, one monsoon-related feature was amplified subtropical ridges (indicated by anticyclonic streamfunction anomalies) across the Atlantic Ocean and Africa in both hemispheres (Fig. 4.26a). La Niña impacts in that field (Bell and Chelliah 2006) included cyclonic streamfunction anomalies in both hemispheres of the western and central subtropical Pacific, along with a contribution to the anticyclonic anomalies across the Caribbean Sea and MDR. This combination resulted in a zonal wave-1 anomaly pattern in both hemispheres (green ovals in Fig. 4.26a) that is a classic signal for an extremely active Atlantic hurricane season (Bell and Chelliah 2006; Landsea et al. 1998; Bell et al. 2011).

Within the MDR, this anomaly pattern also reflected a weaker tropical upper-tropospheric trough (indicated by anomalous easterly winds in Fig. 4.26b). Other monsoon-related features were present in the lower troposphere, including lower sea level pressure and weaker easterly and northeasterly trade winds (indicated by westerly and southwesterly anomalies) across the southern half of the central and eastern MDR (Fig. 4.26c).

The resulting combination of anomalous low-level westerlies and upper-level easterlies produced an extensive area of weak vertical wind shear across the tropical Atlantic, western Caribbean Sea, and southern Gulf of Mexico (Figs. 4.27a,b). The area-averaged magnitude of the vertical

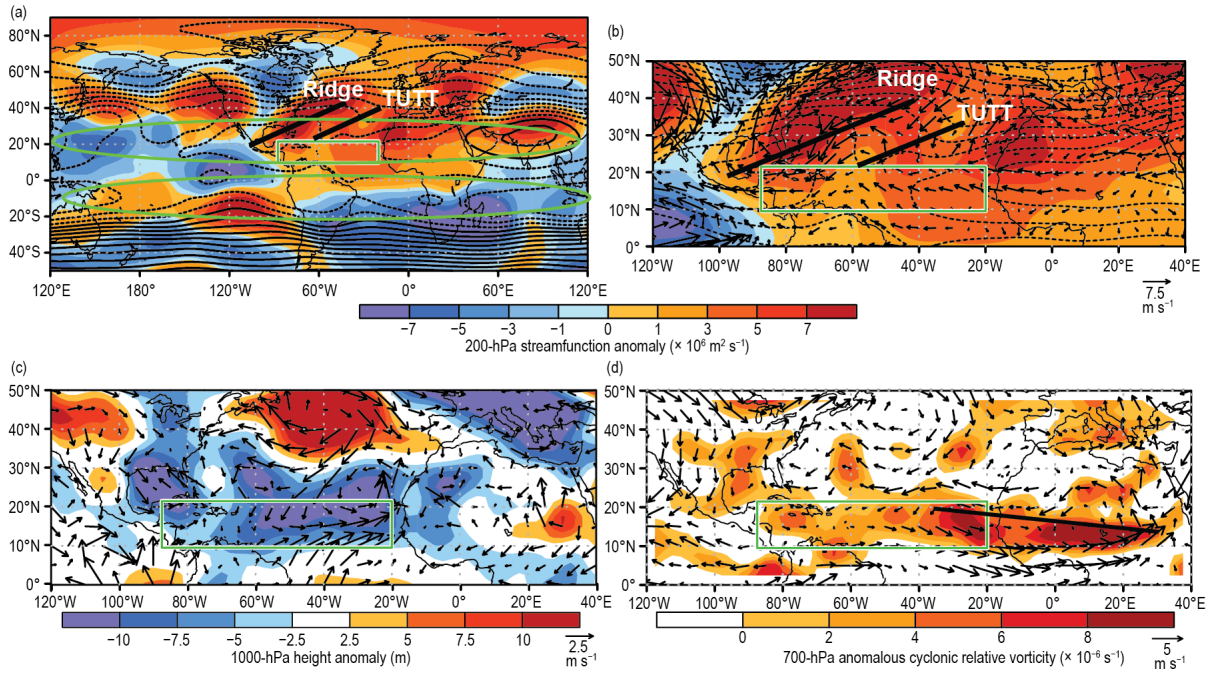

Fig. 4.26. Aug–Oct 2020: (a), (b) 200-hPa streamfunction (contours, interval is 5 × 10^6 m^2 s^{-1}) and anomalies (shaded), with anomalous vector winds (m s^{-1}) also shown in (b); (c) anomalous 1000-hPa heights (shaded, m) and vector winds; and (d) anomalous 700-hPa cyclonic relative vorticity (shaded, × 10^{-6} s^{-1}) and vector winds. In (a), (b) the upper-level ridge and TUTT discussed in the text are labeled and denoted by thick black lines. In (a), green ovals highlight the zonal wave-1 pattern discussed in the text. In (d), the thick solid line indicates the axis of the mean African Easterly Jet, which was hand-drawn based on total seasonal wind speeds (not shown). Vector scales differ for each panel and are below right of color bar. The green box denotes the MDR. Anomalies are departures from the 1981–2010 means. (Source: NCEP/NCAR Reanalysis [Kalnay et al. 1996].)

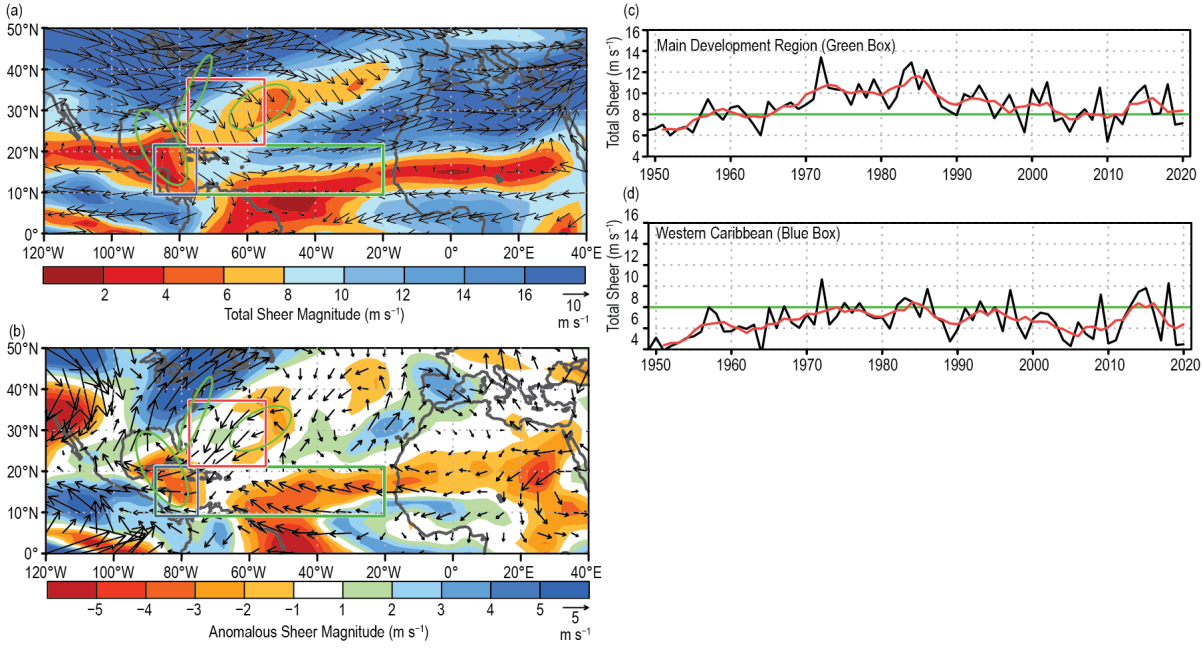

Fig. 4.27. Aug–Oct (ASO) magnitude of the 200–850 hPa vertical wind shear (m s^{-1}): 2020 (a) total magnitude and vector and (b) anomalous magnitude and vector. (c), (d) Time series of ASO vertical shear magnitude (black) and 5-point running mean of the time series (red) averaged over (c) the MDR (green box in (a),(b) spanning 20°–87.5°W and 9.5°–21.5°N), and (d) the western Caribbean Sea (blue box in (a),(b) spanning 87.5°–75°W and 9.5°–21.5°N). Regions with increased track density are shown by green ovals copied from Fig. 4.23c. Anomalies are departures from the 1981–2010 means. (Source: NCEP/NCAR Reanalysis [Kalnay et al. 1996].)

wind shear for the entire MDR was 7.2 m s^{-1} (Fig. 4.27c) and for the western Caribbean Sea was an exceptionally low 4.5 m s^{-1} (Fig. 4.27d). Both of these values are well below the upper threshold of 8 m s^{-1} considered conducive to hurricane formation on monthly time scales (Bell et al. 2017).

The anomalous low-level circulation also reflected an extensive flow of deep tropical moisture into the southern half of the central and eastern MDR. This moisture not only helps feed the monsoon, but also favors increased Atlantic hurricane activity. This situation contrasts with the drier and cooler air that normally accompanies enhanced northeasterly trade winds when the monsoon is weak.

Another aspect of the enhanced West African monsoon system during ASO 2020 was an upward extension of the easterly wind anomalies over the eastern half of the MDR to at least the 700-hPa level (Fig. 4.26d), which is the approximate level of the African Easterly Jet (AEJ). This anomaly pattern contributed to a deep layer of anomalous cyclonic relative vorticity (i.e., increased horizontal cyclonic shear) along the equatorward flank of the AEJ. These conditions are known to favor increased TC activity by helping African easterly waves to be better maintained and by providing an inherent cyclonic rotation to their embedded convective cells (Bell et al. 2004, 2006, 2017, 2018, 2020; Landsea et al. 1998).

The above conditions typified the many above-normal and extremely active seasons seen during the current Atlantic high-activity era; however, interannual signals were also in play during 2020. One of those was La Niña, which supported increased Atlantic hurricane activity over the Caribbean Sea and southern Gulf of Mexico in response to its contribution to weaker vertical wind shear. Another interannual signal was a strong ridge over the western North Atlantic (Figs. 4.26a,b). This ridge contributed to the weak vertical wind shear (Fig. 4.27a), exceptionally warm SSTs over the western North Atlantic (Fig. 4.24d), and to the development of several hurricanes north of the MDR. It also contributed to a highly anomalous steering current (Fig. 4.28), which not only helped focus the storm tracks (Fig. 4.23c), but also contributed to the development of several hurricanes north of the MDR.

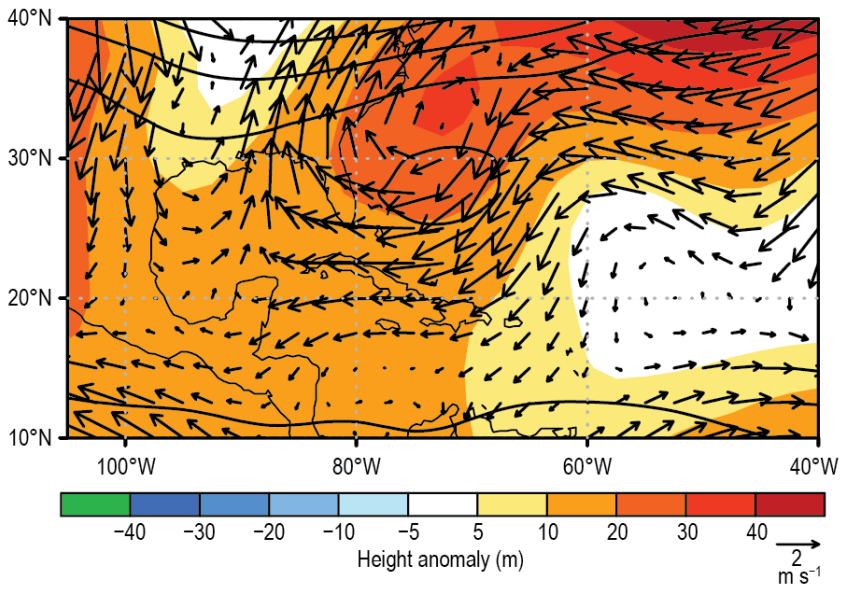

Fig. 4.28. Aug–Oct (ASO) vertically averaged anomalous wind vector between 850 and 200 hPa, along with 500-hPa heights (contours) and anomalies (shaded). (Source: NCEP/NCAR Reanalysis [Kalnay et al. 1996].)

Sidebar 4.1: Hurricane Laura: A record-setting hurricane for southwest Louisiana—

P. J. KLOTZBACH AND R. E. TRUCHELUT

The 2020 Atlantic hurricane season was extremely active, setting the record for most named storms observed in a single season with 30, breaking the old record of 28 set in 2005. The 2020 season also broke the record for most continental United States named storm landfalls in a single season with 11, breaking the old record of nine set in 1916. Of these 11 named storm landfalls, Hurricane Laura was the strongest, making landfall near Cameron, Louisiana, with maximum sustained winds of 130 kt (67 m s^{-1}) on 27 August 2020. Laura caused tremendous damage in Lake Charles and other smaller communities in southwest Louisiana. Laura was the third of four named storms that would make landfall in Louisiana in 2020, tying the old record of four Louisiana named storm landfalls set in 2002.

Fig. SB4.1. GeoColor satellite image of Category 4 Hurricane Laura on 26 Aug at 2050 UTC.

Here, the meteorological history of Laura will be summarized, along with some of the notable records that the system set. Historical landfall records from 1851–present are taken from the National Hurricane Center/Atlantic Oceanographic and Meteorological Laboratory archive located at: http://www.aoml.noaa.gov/hrd/hurdat/All_U.S._Hurricanes.html. Laura's observed values are taken from Pasch et al. (2021). All times are listed in hours UTC.

Laura became a tropical depression on 20 August in the central tropical Atlantic and slowly intensified to a tropical storm the following day. Westerly shear and dry air entrainment caused persistent displacement of the mid- and low-level circulation centers, and Laura remained a low-end tropical storm as it tracked just south of Puerto Rico on 22 August. Vertical wind shear decreased as Laura crossed the southern portion of the Dominican Republic and Haiti on 23 August. This allowed for better vortex alignment, and maximum sustained winds increased to 55 kt (28 m s^{-1}) before weakening slightly due to both an increase in northerly shear and land interaction with Cuba on 24 August.

Once Laura emerged from the west coast of Cuba, the storm entered a more favorable environment of relatively low wind shear, high sea surface temperatures (~30°C), and increased levels of mid-level moisture. Laura intensified slowly at first, reaching hurricane strength at 1200 UTC on 25 August over the south-central Gulf of Mexico. By early on 26 August, the environment became even more conducive for strengthening, and Laura rapidly intensified from a 75-kt (39-m s^{-1}) Category 1 hurricane at 00 UTC on 26 August to a 130-kt (67-m s^{-1}) Category 4 hurricane at 00 UTC on 27 August (Fig. SB4.1). This 55-kt (28-m s^{-1}) intensification in 24 hours was the fastest intensification rate for an Atlantic named storm in the Gulf of Mexico since Hurricane Karl in 2010, which also intensified by 55 kt (28 m s^{-1}) in 24 hours. Around 6 hours after ending its rapid intensification, Laura made landfall in southwest Louisiana at its peak intensity (i.e., 130 kt [67 m s^{-1}]). Following landfall, Laura rapidly weakened to a tropical storm later on 27 August and then to a tropical depression on 28 August as it tracked north into Arkansas, dissipating early on 29 August over the Ohio Valley.

Fig. SB4.2. Heavily damaged National Weather Service Lake Charles radar following Hurricane Laura. (Image courtesy of Brett Adair, Live Storms Media.)

Hurricane Laura caused tremendous damage in southwestern Louisiana, with a current estimated cost of $19 billion (U.S. dollars). Laura was responsible for seven direct and 34 indirect fatalities in the United States, with 31 additional fatalities occurring in Haiti and nine in the Dominican Republic. About 4 to 6 m of storm surge occurred to the east of Laura's landfall near Creole and Grand Chenier, Louisiana. Lake Charles, Louisiana, suffered extreme wind damage from gusts exceeding 115 kt (59 m s^{-1}), including the destruction of the Lake Charles' Weather Forecast Office's WSR-88D doppler radar (Fig. SB4.2). Laura's track was slightly farther east than anticipated just before landfall, thus sparing Lake Charles a much more significant storm surge.

The 130 kt (67 m s^{-1}) maximum sustained winds at the time of Laura's landfall were the strongest for a Louisiana hurricane since the Last Island Hurricane of 1856 and tied for the fifth strongest on record in the continental United States. Laura's landfall pressure of 939 hPa was the fourth lowest for a Louisiana hurricane on record, trailing Katrina in 2005 (920 hPa), the Last Island Hurricane in 1856 (934 hPa), and Rita in 2005 (937 hPa). Laura also rapidly intensified prior to landfall, defined to be an intensification of ≥30 kt in 24 hours (≥15 m s^{-1} in 24 hours). This was one of three hurricanes in 2020 to rapidly intensify in the 24 hours before its continental U.S. landfall, with the others being Hurricanes Hanna and Zeta. Like Laura, Zeta also rapidly intensified in the 24 hours prior to its landfall in Louisiana. Laura's 40 kt (21 m s^{-1}) of intensification in its final 24 hours prior to landfall in the continental United States are tied with Hurricanes Michael (2018) and Charley (2020) for the second highest in the last two decades, trailing only Zeta, which intensified by 45 kt in the 24 hours before its landfall in Louisiana in late October 2020.

3) Eastern North Pacific and Central North Pacific basins—K. M. Wood and C. J. Schreck

(I) SEASONAL ACTIVITY

This section combines statistics from the two agencies responsible for issuing advisories and warnings in the eastern North Pacific (ENP) basin: NOAA's National Hurricane Center in Miami, Florida (from the Pacific coast of North America to 140°W), and NOAA's Central Pacific Hurricane Center in Honolulu, Hawaii (between 140°W and the date line, the Central North Pacific [CNP]).

A total of 17 named storms formed in the combined ENP/CNP basin in 2020 (Fig. 4.29a), four of which became hurricanes and three became major hurricanes. This activity is near normal for named storms but below normal for hurricanes: the 1981–2010 IBTrACS seasonal averages are 16.5 named storms, 8.5 hurricanes, and 4.0 major hurricanes (Schreck et al. 2014). All named storms occurred between the official hurricane season start date of 15 May and end date of 30 November; however, the first tropical depression formed at 1200 UTC on 25 April, marking the earliest ENP tropical cyclone (TC) formation since the start of the satellite record in 1966 (Cangialosi 2020). That depression did not reach tropical storm intensity; the first to do so was Tropical Storm Amanda on 31 May. The final named storm, Tropical Storm Polo, dissipated on 19 November. Sixteen named storms were classified operationally and post-season analysis revealed the season's seventh tropical depression was, in fact, a short-lived tropical storm (Brown 2020). No named storms formed within the CNP, but one (Douglas) entered the region from the east, placing 2020 well below the 1981–2010 IBTrACS seasonal average of 4.7 for the CNP.

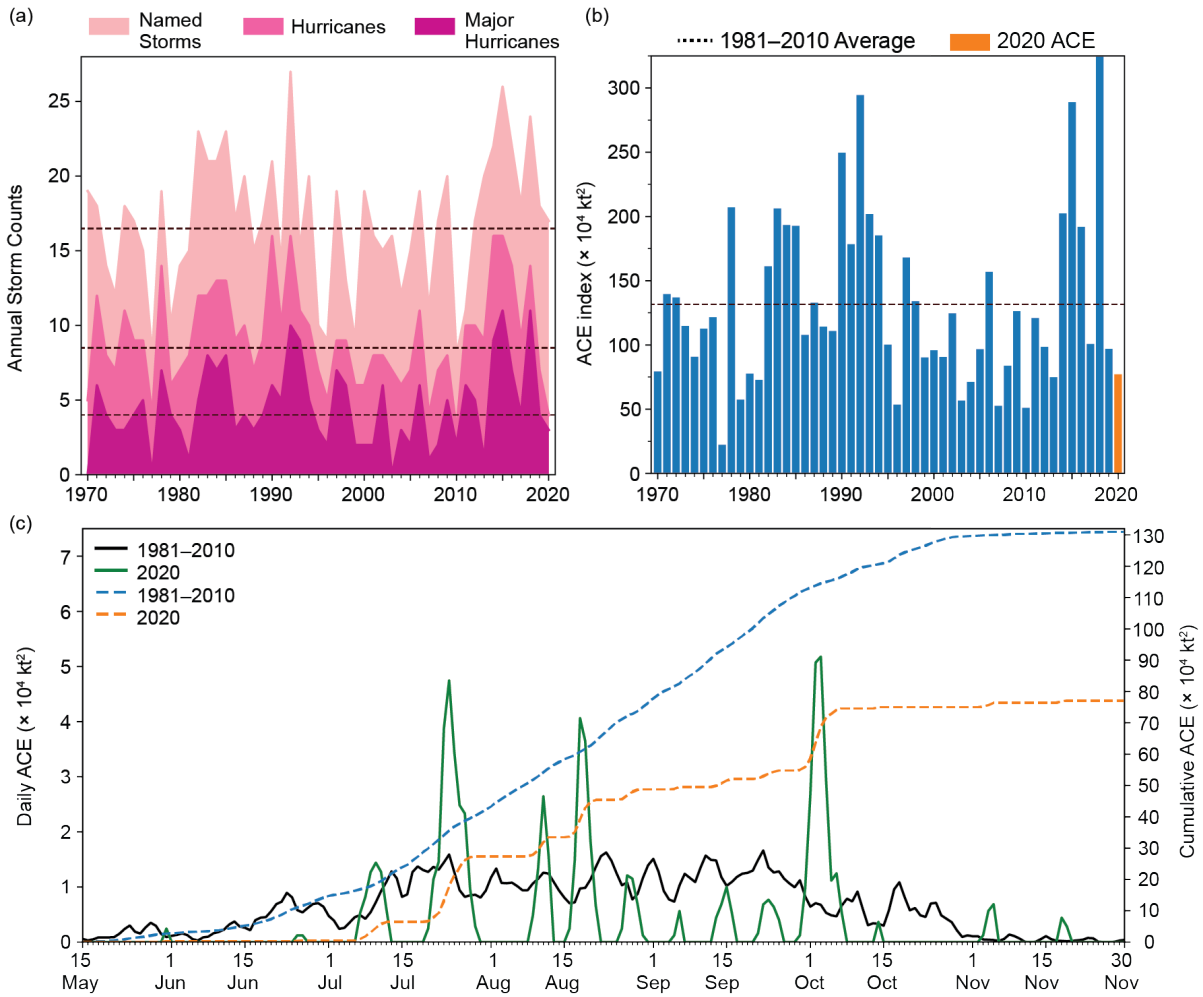

Fig. 4.29. (a) Annual storm counts by category during 1970–2020, with the 1981–2010 average by category denoted by each dashed line. (b) Annual ACE during 1970–2020, with 2020 highlighted in orange and the 1981–2010 average denoted by the dashed line. (c) Daily ACE during 1981–2010 (solid black) and during 2020 (solid green); accumulated daily ACE during 1981–2010 (dashed blue) and during 2020 (dashed orange).

The 2020 seasonal ACE index was 77 × 10^4 kt^2, or 58% of the 1981–2010 mean of 132 × 10^4 kt^2 (Figs. 4.29b,c; Bell et al. 2000; Schreck et al. 2014). The bulk of 2020 TC activity, including three hurricanes and two major hurricanes, was confined to July and August (comprising 63% of the season's ACE). Only tropical storms formed in September, and the season's final major hurricane (Marie) occurred in early October.

As in 2019 (Wood and Schreck 2020), three 2020 ENP TCs contributed more than half of the season's total ACE, with each reaching Category 4 intensity (113–136 kt; 58–70 m s^{-1}) on the SSHWS. In addition, all three TCs underwent rapid intensification (≥30 kt or 15.4 m s^{-1} in 24 hours) prior to peak intensity and later rapidly weakened while over open ocean (≤–30 kt or –15.4 m s^{-1} in 24 hours; Wood and Ritchie 2015). Hurricane Genevieve (16–21 August) exhibited the fastest 24-hour intensification rate of 50 kt (26 m s^{-1}). The fastest 24-hour intensification rate for Hurricane Douglas (21–29 July) was 45 kt (23 m s^{-1}), and Hurricane Marie (29 September–6 October) intensified 40 kt (21 m s^{-1}) in 24 hours. Despite achieving the most rapid 24-hour intensification rate, Genevieve spent the least amount of time at its peak intensity, which lasted only 6 hours before it began weakening. Conversely, Marie maintained ≥115-kt maximum winds for 30 hours.

(II) ENVIRONMENTAL INFLUENCES ON THE 2020 SEASON

Negative SST anomalies were observed over much of the equatorial eastern Pacific during the 2020 ENP hurricane season, a signature of the developing La Niña event (section 4b), although season-averaged SSTs were generally above normal where most TCs formed (Fig. 4.30a). Pronounced positive anomalies persisted at higher latitudes, particularly north of Hawaii, and these warmer-than-normal waters may have contributed to the long track of Douglas near Hawaii in July.

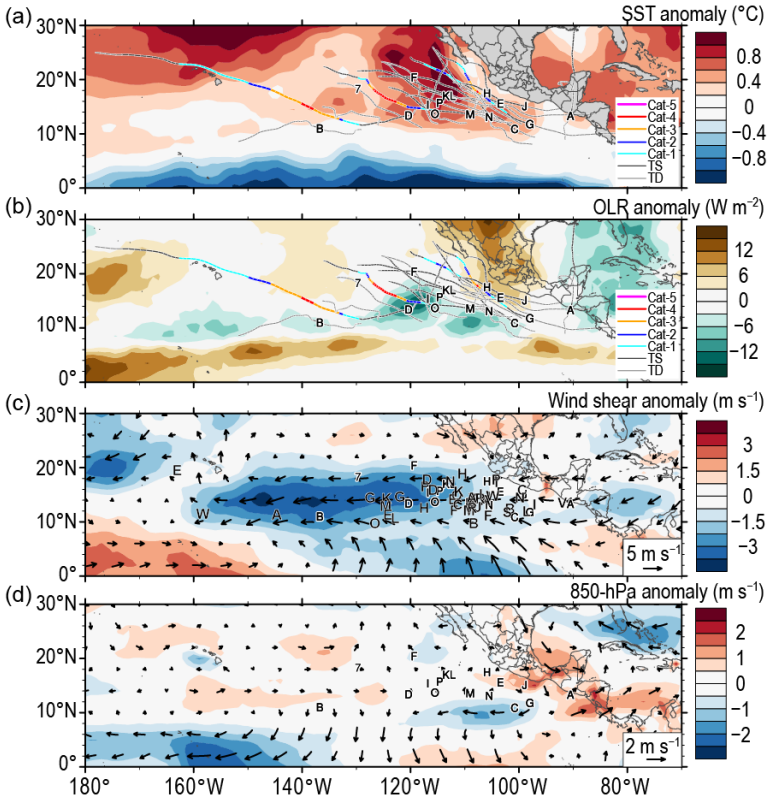

Fig. 4.30. 15 May–30 Nov 2020 anomaly maps of (a) SST (°C; Banzon and Reynolds 2013), (b) OLR (W m^{-2}; Schreck et al. 2018), (c) 200–850-hPa vertical wind shear (m s^{-1}) vector (arrows) and scalar (shading) anomalies, and (d) 850-hPa wind (m s^{-1}, arrows) and zonal wind (shading) anomalies. Anomalies are relative to the annual cycle from 1981–2010, except for SST, which is relative to 1982–2010 due to data availability. Letters denote where each TC attained tropical storm intensity; "7" represents the unnamed tropical storm revealed in post-season analysis. Wind data are obtained from CFSR (Saha et al. 2014).

Most TC activity was confined to the eastern part of the basin, where OLR anomalies were near or below normal and co-located with below-normal vertical wind shear (Figs. 4.30b,c); however, only two TCs tracked west of 120°W where the shear was most anomalously below normal. As in recent ENP seasons, 2020 was again marked by enhanced 850-hPa easterly flow near Central America, which may have limited activity by reducing the available low-level cyclonic vorticity (Fig. 4.30d).

Tropical cyclone activity in the ENP, especially cyclogenesis, can be affected by the Madden-Julian Oscillation (MJO) as well as convectively coupled Kelvin waves (e.g., Maloney and Hartmann 2001; Aiyyer and Molinari 2008; Schreck and Molinari 2011; Ventrice et al. 2012a,b; Schreck 2015, 2016). Although the MJO signal was weak within the ENP for much of the hurricane season, the enhanced convective phase in August may have supported the development of Elida, Fausto, and Genevieve (Fig. 4.31; see Kiladis et al. 2005, 2009 for methodology). The convectively enhanced phase of Kelvin waves likely contributed to the formation of Amanda, Boris, Cristina, Douglas, Iselle, and Lowell. Easterly wave activity can be inferred from Fig. 4.31 as westward-moving negative (green) anomalies; such waves were particularly active during the genesis of Cristina, Elida, Genevieve, Hernan, Karina, Lowell, Marie, Odalys, and Polo.

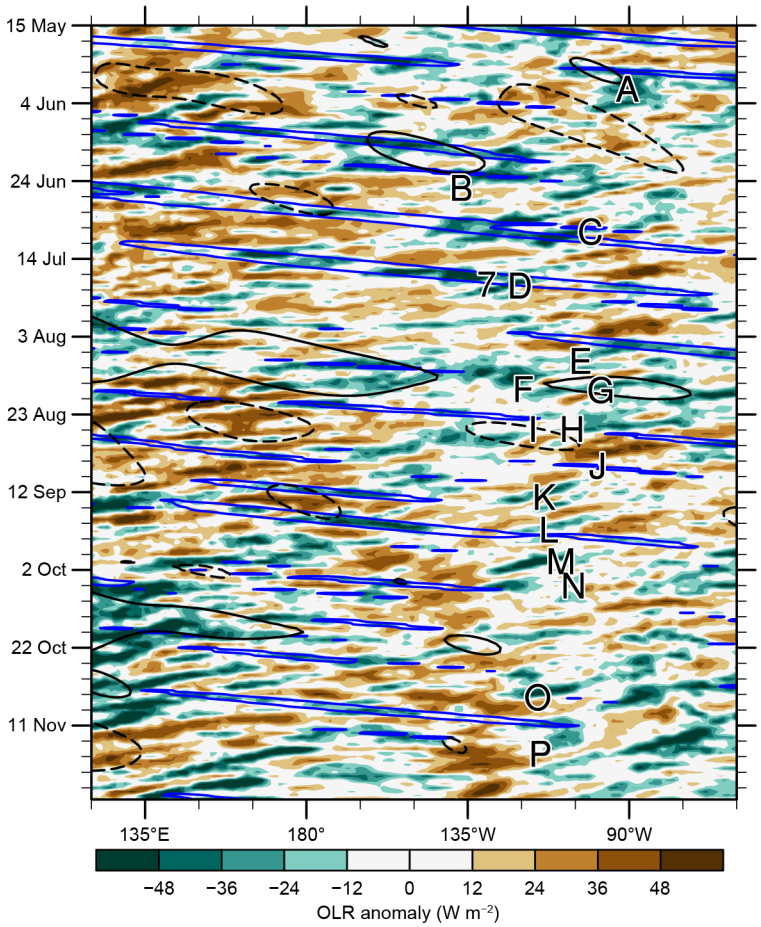

Fig. 4.31. Longitude–time Hovmöller diagram of 15°–5°N average OLR (W m^{-2}; Schreck et al. 2018). Unfiltered anomalies from a daily climatology are shaded. Negative anomalies (green) indicate enhanced convection. Anomalies filtered for Kelvin waves are contoured in blue at –10 W m^{-2} and MJO-filtered anomalies are contoured in black at ±10 W m^{-2} (dashed for positive, solid for negative). Letters denote the longitude and time when each TC attained tropical storm intensity; "7" represents the unnamed tropical storm revealed in post-season analysis.

(III) TROPICAL CYCLONE IMPACTS

One ENP TC made landfall while at least at tropical storm strength, yet five TCs (Amanda, Genevieve, Hernan, Iselle, and Douglas) produced impacts in 2020. Tropical Storm Amanda (30–31 May) became the second known Pacific TC to make landfall in Guatemala, with the first being Tropical Storm Agatha in 2010 (Berg 2020). Amanda contributed to excessive rainfall, widespread flooding, and numerous mudslides in Central America. The other contributors were Atlantic Tropical Storm Cristobal (which formed in part from Amanda's remnants) and a Central American gyre in the region as described by Papin (2014). These impacts resulted in 40 deaths, affected over 100,000 people, and damaged or destroyed over 3000 ha of crops (Berg 2020).

On average, 1.8 ENP TCs make landfall in Mexico each year (Raga et al. 2013), but no TCs made landfall in 2020. Nonetheless, Hurricane Genevieve tracked close to Baja California Sur, bringing heavy rain and strong winds to the peninsula as it weakened while encountering decreasing SSTs and dry air. Short-lived Tropical Storm Hernan (26–28 August) also impacted Baja California Sur, although it also did not make landfall. Shortly after Hernan dissipated, Tropical Storm Iselle (26–30 August) approached Baja California but weakened to a remnant low well offshore.

Hurricane Douglas, one of three Category 4 ENP hurricanes in 2020 and the only named storm to reach the CNP portion of the basin, passed within 50 nautical miles (93 km) of multiple Hawaiian Islands while at hurricane intensity (Latto 2020). Although the TC did not make landfall, its circulation crossed several of the northwestern Hawaiian Islands as a tropical storm. In line with its close proximity to land, there was some minor damage in Hawaii—mainly nuisance flooding and some downed trees, but no casualties were reported due to Douglas (see https://weather.com/safety/hurricane/news/2020-07-27-hawaii-hurricane-douglas).

4) Western North Pacific basin—S. J. Camargo

(I) OVERVIEW

The 2020 TC season in the western North Pacific (WNP) was below normal by most measures of TC activity. The data used here are primarily from the JTWC best-track data for 1945–2019 and preliminary operational data for 2020. All statistics are based on the 1981–2010 climatological period unless otherwise noted.

According to the JTWC, a total of 23 TCs (bottom quartile ≤ 23) reached tropical storm intensity in 2020. From these, 12 reached typhoon intensity (bottom quartile ≤ 15), with two reaching super typhoon status (≥130 kt, bottom quartile ≤ 2). There were also three tropical depressions (median = 3.5); however, Krovanh was considered a tropical storm by the Japan Meteorological Agency (JMA). Only 52% of the tropical storms intensified into typhoons (bottom quartile ≤ 59%) and only 17% of the typhoons reached super typhoon intensities (median = 25%). Figure 4.32a shows the number of storms in each category for 1945–2020.

The JMA total for 2020 was also 23 TCs (bottom quartile ≤ 23). While this is the same number of storms that reached tropical storm intensity for JTWC, there were differences between the agencies.[4] In addition to Krovanh, Tropical Storm Six was not included among the JMA 2020 storms, and Mekkhala and Kujira were considered typhoons by JTWC, but were only considered tropical storms by JMA. Of the 23 JMA TCs, eight were tropical storms (top quartile ≥ 7), five were severe tropical storms (median = 5), and 10 were typhoons (bottom quartile ≤ 13). Only 44% of the storms reached typhoon intensity (bottom quartile ≤ 50%). The number of all TCs (1951–1976) and tropical storms, severe tropical storms and typhoons (1977–2020) according to the JMA are shown in Fig. 4.32b. The Philippine Atmospheric, Geophysical and Astronomical Services Administration (PAGASA) named 22 TCs that entered its area of responsibility, including Tropical Depressions Carina, Gener (corresponding to JTWC Tropical Storm Six), and Ofel, which were not named by JMA.

[4] It is well known that there are systematic differences between the JMA and the JTWC datasets. These differences have been extensively documented in the literature (e.g., Knapp et al. 2013; Schreck et al. 2014).

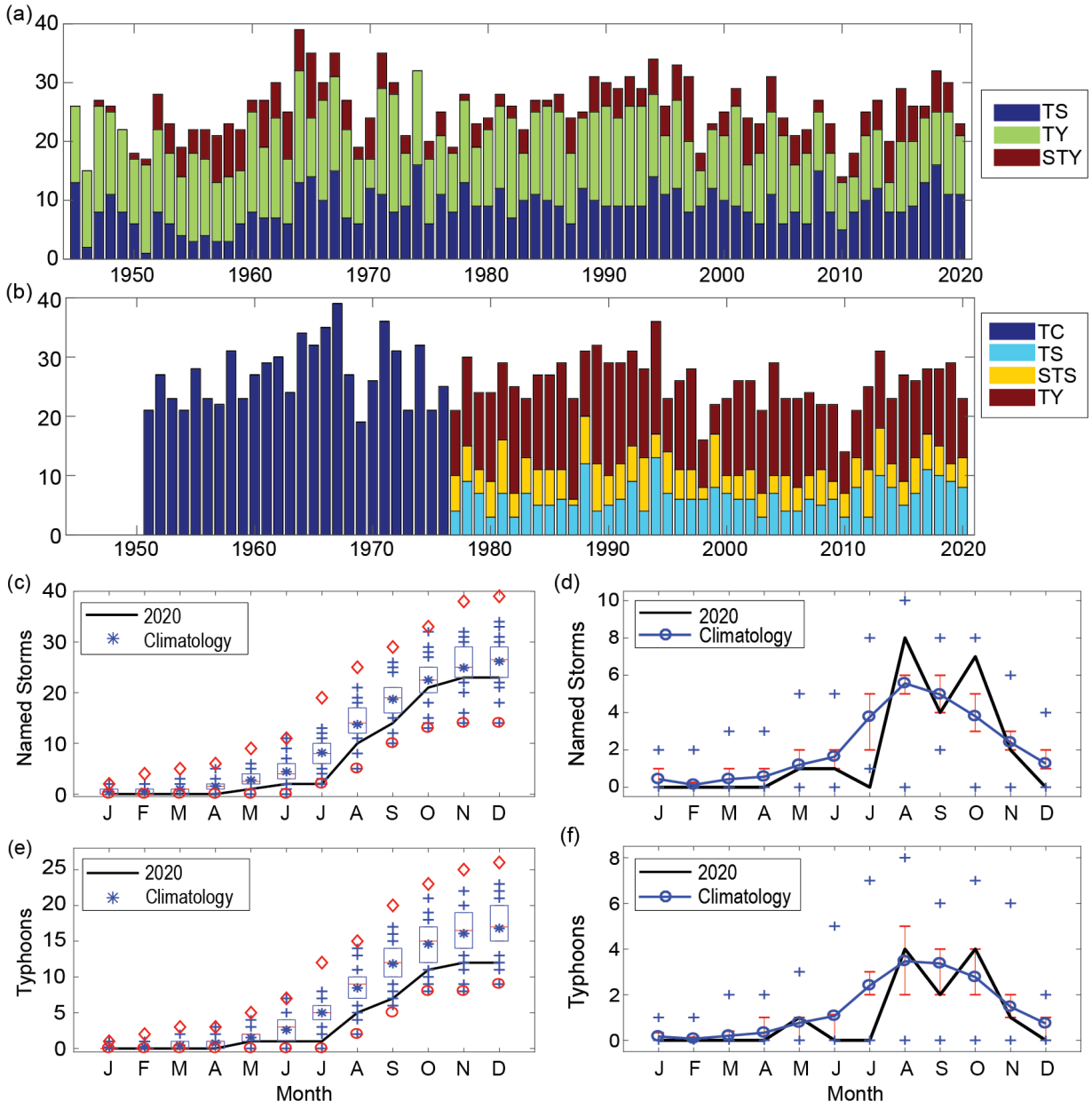

Fig. 4.32. (a) Number of tropical storms (TSs), typhoons (TYs) and super typhoons (STYs) per year in the WNP for the period 1945–2020 based on JTWC data. (b) Number of tropical cyclones (TCs; all storms that reach TS intensity or higher) from 1951 to 1976; number of TSs, severe tropical storms (STSs) and TYs from 1977 to 2020 based on JMA data. Panel (c) shows the cumulative number of tropical cyclones with TS intensity or higher (named storms) per month in the WNP in 2020 (black line), and climatology (1981–2010) as box plots (interquartile range: box; median: red line; mean: blue asterisk; values in the top or bottom quartile: blue crosses; high [low] records in the 1945–2019 period: red diamonds [circles]). Panel (e) is similar to panel (c) but for the number of TYs. Panels (d) and (f) show the number of named storms and TYs per month in 2020 (black line) and the climatological mean (blue line), the blue "+" signs denote the maximum and minimum monthly historical records, and the red error bars show the climatological interquartile range for each month (in the case of no error bars, the upper and/or lower percentiles coincide with the median). (Sources: 1945–2019 JTWC best-track dataset, 2020 JTWC preliminary operational track data for panels (a), (c), (d), (e), and (f); 1951–2020 RSMC-Tokyo, Japan Meteorological Agency (JMA) best-track dataset for panel (b).)

(II) SEASONAL ACTIVITY

No active storms were present from January to April, and therefore the season started with Typhoon Vongfong in May. Only Tropical Storm Nuri was active in June and none were active in July. Therefore, it was a below-normal early typhoon season (January–June) with only two named storms (bottom quartile ≤ 3), including only one typhoon (bottom quartile ≤ 1). The lack of storms during January–April was not unusual. Climatologically, the percentage of the years with an active TC (typhoon) during January, February, March, and April is 40% (16.7%), 13.3% (6.7%), 33.3% (16.7%), and 46.7% (30%), respectively; however, this was the first time in the historical record that no named storms occurred in July (Fig. 4.32d) and previously only four other years had no typhoons that month (1947, 1975, 1998, and 2019; Fig. 4.32f). Furthermore, there were also no typhoons in June, which climatologically has at least one active typhoon in 63% of the years.

By contrast with July, August was a busy month with eight named storms (top quartile ≥ 6), including four tropical storms (Sinlaku, Jangmi, Six, and Higos) and four typhoons (Hagupit, Mekkhala, Bavi, and Maysak; median = 3) active during that month. Super Typhoon Haishen formed on 31 August and was mostly active during September, and thus is considered a September storm in this analysis. There were four named storms active in September: Tropical Storms Noul and Dolphin (bottom quartile ≤ 4) and Super Typhoon Haishen and Typhoon Kujira (bottom quartile ≤ 2). Tropical Depression Twelve also formed in September. Similar to August, October was a busy month with one tropical depression (Twenty) and seven named storms (top quartile ≥ 5), including three tropical storms (Linfa, Nangka, and Atsani) and four typhoons (top quartile ≥ 4; Chan-Hom, Saudel, Molave, and Super Typhoon Goni).

The season ended with two storms in November (bottom quartile ≤ 2), Tropical Storm Etau and Typhoon Vamco (median = 1), and Tropical Depression Krovanh in December. As shown in Figs. 4.32c–e, the early season (January–June) activity level was below normal. These quiet months were followed by an average peak season (July–October), with 19 named storms (median = 17), including 10 typhoons (median = 12). The late season (November–December) was also quiet with two named storms (bottom quartile ≤ 3), including only one typhoon (bottom quartile ≤ 1). The below-normal activity in the early and late seasons led to a below-normal season overall, even with near-normal levels of activity during the peak season, including 2 months (August and October) with above-normal activity.

The total seasonal ACE in 2020 (Fig. 4.33a) was in the bottom quartile of the climatological distribution—the fifth lowest in the historical record. In most months, the ACE value was in the bottom quartile of the climatological distribution. Only May, October, and November ACE values reached the below-normal quartile (25%–50%; Fig. 4.33b). Of particular note is July 2020, which was the first July in the historical record (JTWC records began in 1945) with zero ACE. In contrast, a zero ACE value is not as rare an event in June, having happened 13 times before. Low ACE values are typical of La Niña in the western North Pacific (Camargo and Sobel 2005).

Furthermore, WNP ACE in 2020 had a sharp peak in October, while climatologically the WNP ACE peak is flatter and spread almost equally from August to October (Fig. 4.33b). The months from August to November corresponded approximately to 95% of the total ACE in 2020, which is much higher than the climatological median percentage of 68%. The ACE of three storms in 2020 were each in the top quartile of the ACE per storm climatology: Super Typhoons Goni and Haishen and Typhoon Maisak. Together these three storms contributed to 45% of the seasonal ACE (17%, 16%, and 12%, respectively).

The mean genesis location in 2020 was 17.8°N and 129.5°E, northwest of the climatological mean of 13.2°N, 142.8°E (std. dev. of 1.9° latitude and 5.6° longitude). The mean track position in 2020 was 20.1°N, 127.5°E, similarly northwest of the climatological mean of 17.3°N, 136.6°E (std. dev. of 1.4° latitude and 4.7° longitude). There is a well-known connection between genesis and track shifts in the WNP basin and El Niño/La Niña, with La Niña favoring a northwestward shift in TC genesis and track (Chia and Ropelewski 2002; Camargo and Sobel 2005; Camargo et al. 2007a).

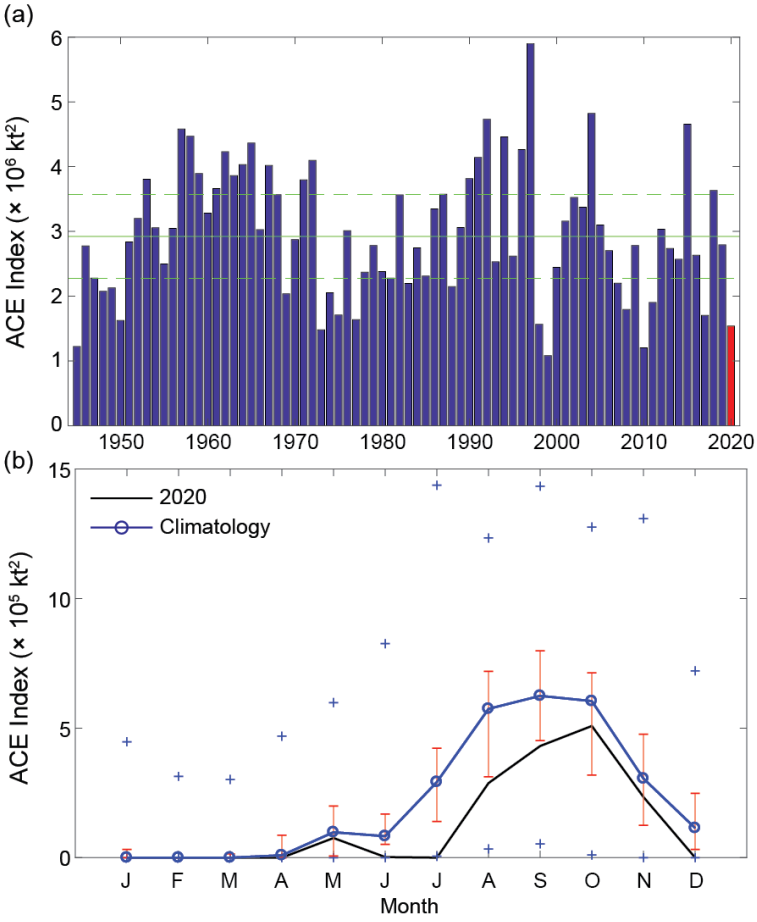

Fig. 4.33. (a) ACE per year in the WNP for 1945–2020. The solid green line indicates the climatological median (1981–2010), and the dashed lines show the climatological 25th and 75th percentiles. (b) ACE per month in 2020 (black line) and the median during 1981–2010 (blue line), with the red error bars indicating the 25th and 75th percentiles. In case of no error bars, the upper and/or lower percentiles coincide with the median. The blue "+" signs denote the maximum and minimum values during the 1945–2019. (Source: 1945–2019 JTWC best-track dataset; 2020 JTWC preliminary operational track data.)

The northwestward shift observed in 2020 is typical of La Niña seasons (genesis mean for La Niña events is 15.5°N, 136.1°E).

There were 70.25 days with active tropical storms and typhoons (bottom quartile ≤ 92.75). From these active days, 30.5 had typhoons (bottom quartile ≤ 49.5) and 10 days had major typhoons (Saffir–Simpson Categories 3–5; bottom quartile ≤ 15.75). The percentage of active days with typhoons and intense typhoons was 34% (bottom quartile ≤ 33%) and 11% (bottom quartile ≤ 10%), respectively. The median lifetime for TCs reaching tropical storm intensity was 5.0 days (bottom quartile ≤ 6.25 days) and for those reaching typhoon intensity was 6.4 days (bottom quartile ≤ 7.75 days).

The longest-lived storm in 2020 was Typhoon Chan-Hom (11.25 days), which was the only storm in the top quartile of the distribution (≥10.5 days). From the 23 named storms, only five had lifetimes above the median (7.75 days). These short-lived storms are another characteristic of La Niña in the WNP (Camargo and Sobel 2005; Camargo et al. 2007a). The maximum number of TCs active simultaneously in 2020 was three and occurred on 10 August (Tropical Storms Sinlaku, Jangmi, and Six), while two typhoons (Maysak and Haishen) were active on 2 September. The historical record is six active TCs (14–15 August 1996).

Including tropical depressions, 17 storms made landfall in 2020 (median = 17, 1951–2010 climatology). Landfall here is defined when a TC track is over land, and the previous TC location was over the ocean. In order to include landfall over small islands, tracks were interpolated from 6-hourly to 15-minutes intervals, and a high-resolution land mask was used. In cases of multiple landfalls, we considered the landfall with the highest intensity for each storm. Two storms made landfall as tropical depressions (below normal: 1–2 TDs), eight as tropical storms (top quartile ≥ 8), and five as typhoons Categories 1–2 (median = 5). Typhoon Vongfong and Super Typhoon Goni made landfall as major typhoons (Category 3–5; median = 2). Vongfong (named Ambo by PAGASA) made multiple landfalls in the Philippines, with the first and most intense landfall at San Policarpo in Eastern Samar. In late October, Typhoon Molave made landfall in both the Philippines and Vietnam and was followed in early November by Super Typhoon Goni (named Rolly by PAGASA), which made landfall in the same countries. Early estimates considered the Category 5 intensity of Goni at landfall at Catanduanes in the Philippines to be the strongest TC landfall ever recorded.

(III) ENVIRONMENTAL CONDITIONS

Figure 4.34 shows the environmental conditions associated with the 2020 typhoon season (June–October). The La Niña event was present for most of the typhoon season, with La Niña conditions developing in August 2020 (see section 4b). The SST anomaly pattern during the peak typhoon season (July–October [JASO]; Figs. 4.2c,d) was dominated by the standard eastern Pacific La Niña pattern, which includes above-normal SSTs in the western North Pacific. The genesis potential index (GPI; Fig. 4.34a; Emanuel and Nolan 2004; Camargo et al. 2007b) in JASO was characterized by two large regions of positive anomalies: the first near the Philippines and the second a large zonal band centered around 30°N. The first position of the storms formed during those months is also shown in Fig. 4.34a (black asterisks), and they are located around those two positive anomaly bands. The potential intensity (Emanuel 1988) anomalies (Fig. 4.34b) mostly reflect the SST anomalies, with positive anomalies in a horseshoe pattern in most of the WNP and negative anomalies close to the equator in the eastern part of the basin. With the exception of two bands of 600-hPa relative humidity anomalies (Fig. 4.34c) in the equatorial region (positive to the west, negative to the east), mid-level relative humidity was close to climatological conditions.

The extent of the monsoon trough, defined by 850-hPa zonal winds (Fig. 4.34d), was restricted from the South China Sea to the Philippines, as is typical in La Niña events. Many storms formed in this region during 2020 (Fig. 4.34a). Given the record lack of TCs in July, the conditions in that month are shown in Fig. 4.34e (GPI) and Fig. 4.34f (vertical wind shear). GPI anomalies in July (Fig. 4.34e) were negative in most of the basin, and the location of these negative anomalies coincided with regions of stronger-than-normal vertical wind shear (Fig. 4.34f). Comparing the GPI anomalies in July with the other components of the index (not shown: vorticity, potential intensity,

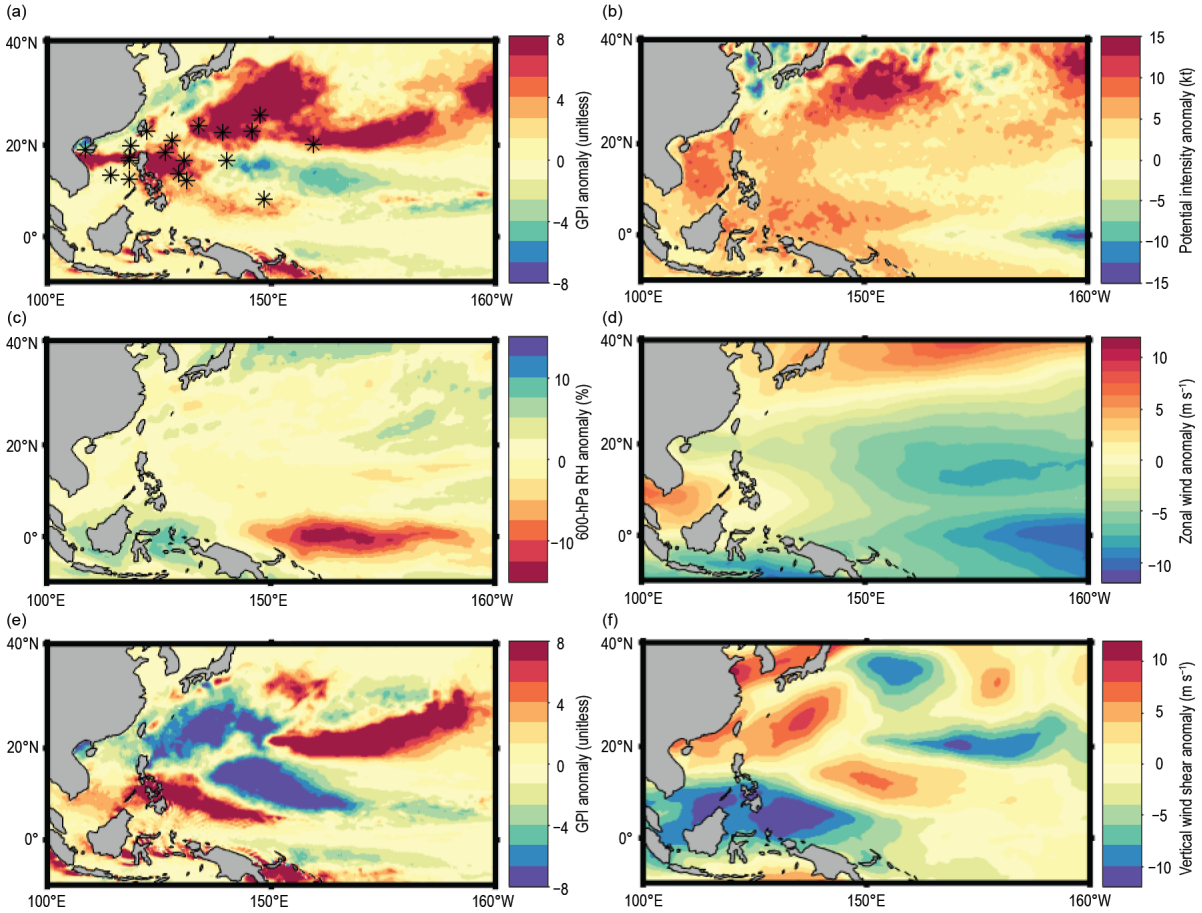

Fig. 4.34. (a) GPI anomalies in JASO 2020. First position of storms in JASO 2020 is marked with an asterisk, (b) potential intensity anomalies in JASO 2020, (c) 600-hPa relative humidity anomalies (%) in JASO 2020, (d) 850-hPa zonal winds (m s^{-1}) in JASO 2020, (e) GPI anomalies for Jul 2020, and (f) vertical wind shear magnitude anomalies for Jul 2020. (Source: ERA5 reanalysis [Hersbach et al. 2020].)

and relative humidity), it is clear that vertical wind shear anomalies were the main cause of the unfavorable GPI values during July. In addition to these unfavorable conditions, the MJO in July was active over the North Indian Ocean and suppressed over the WNP (Fig. 4.7), which likely contributed to the lack of storms that month.

(IV) TROPICAL CYCLONE IMPACTS

Many storms had social and economic impacts in Asia in 2020, in particular Typhoons Molave, Goni, and Vamco. Typhoon Molave mainly affected the Philippines and central Vietnam, where the storm caused widespread destruction and was one of the strongest storms to hit the country in the past 20 years according to the Vietnam Meteorological and Hydrological Administration. Molave was one of seven typhoons that affected Vietnam in 2020, and the combination of the monsoonal rains with these storms led to severe flooding in that country.

Super Typhoon Goni was the strongest TC to make landfall in the historical record and led to the evacuation of almost 1 million people from its path, with thousands of homes destroyed. Typhoon Vamco affected the same region of the Philippines just a few days later. This led to an emergency situation in the Philippines, with the National Disaster Risk Reduction and Management Council declaring a "state of calamity" for the island of Luzon. Local authorities reported the worst floods there in 45 years.

5) North Indian Ocean basin—A. D. Magee and C. J. Schreck

(I) SEASONAL ACTIVITY

The North Indian Ocean (NIO) TC season typically occurs between April and December, with two peaks of activity: May–June and October–December, due to the presence of the monsoon trough over tropical waters of the NIO during these periods. Tropical cyclone genesis typically occurs in the Arabian Sea and the Bay of Bengal between 8°N and 15°N. The Bay of Bengal, on average, experiences four times more TCs than the Arabian Sea (Dube et al. 1997).

The 2020 NIO TC season was the costliest season in recorded history, with damages amounting to ~$16 billion (U.S. dollars), the majority of which was driven from impacts associated with Super Cyclone Amphan ($13.9 billion [U.S. dollars]). In total, five named storms, four cyclones, and two major cyclones occurred in the region. While the number of named storms matched the IBTrACS–JTWC 1981–2010 climatology of 5.0, the numbers of both cyclones and major cyclones were tied for the third most since 1981 and were both more than double their climatological values (1.6 and 0.7, respectively; Fig. 4.35). Two major cyclone events occurred in the 2020 NIO TC season: Super Cyclone Amphan and Very Severe Cyclonic Storm Gati.

Above-average ACE index values were also recorded. The 2020 seasonal ACE index was 26.6 × 10^4 kt^2, over three times less than the record-shattering ACE generated during the 2019 NIO season, but above the 1981–2010 climatology of 19.1 × 10^4 kt^2. Indian Ocean dipole (IOD) conditions, as measured by the Dipole Mode Index, were neutral for the majority of the 2020 NIO TC

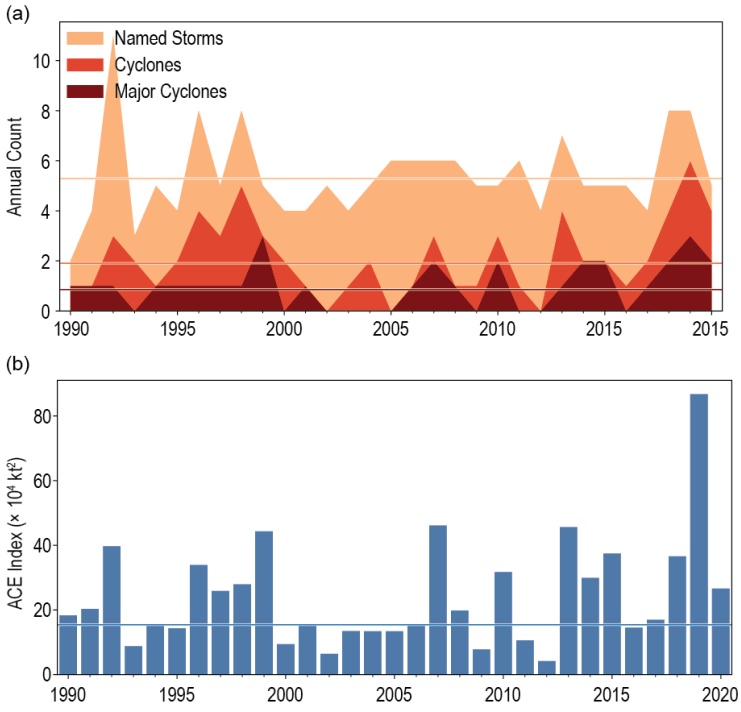

Fig. 4.35. Annual TC statistics for the NIO for 1990–2020: (a) number of named storms, cyclones, and major cyclones and (b) ACE (× 10^4 kt^2). Horizontal lines represent the 1981–2010 climatology.

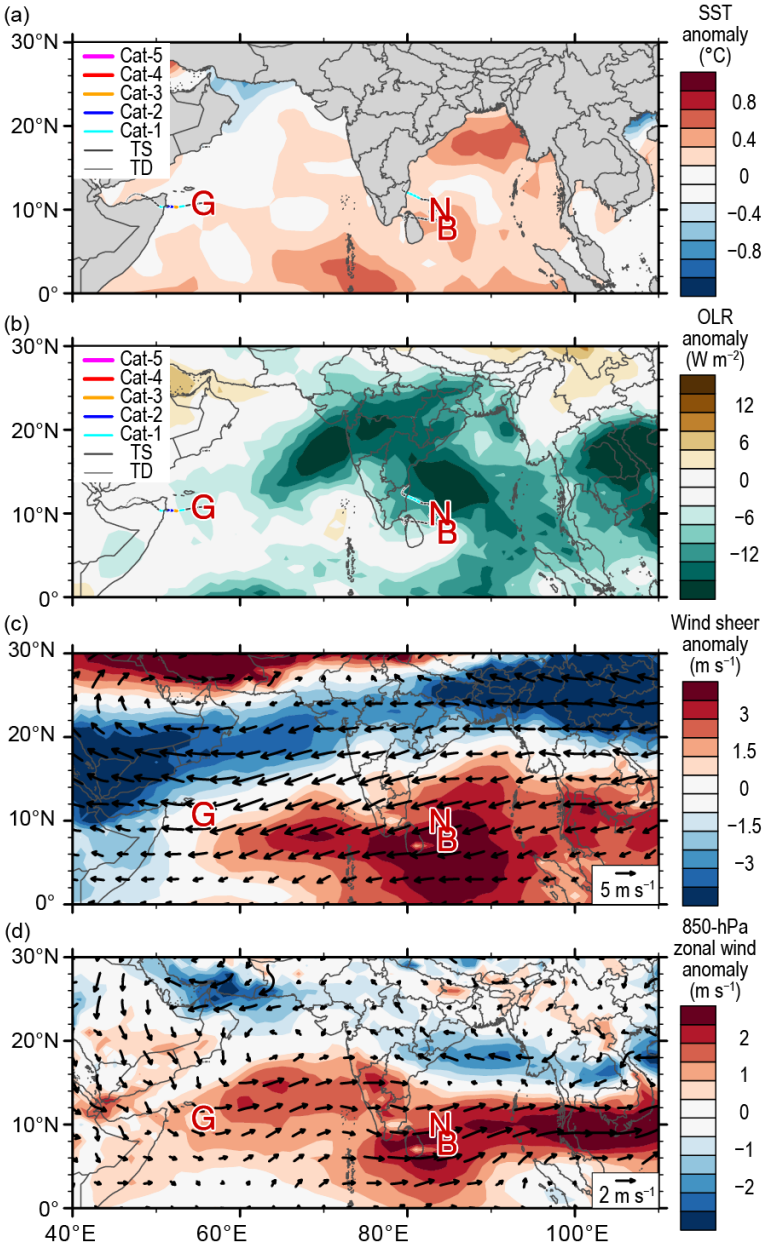

Fig. 4.36. 15 Sep–15 Dec 2020 NIO anomaly maps of (a) SST (°C; Banzon and Reynolds 2013), (b) OLR (W m $^{-2}$; Schreck et al. 2018), (c) 200–850-hPa vertical wind shear (m s^{-1}) vector (arrows) and scalar anomalies (shading), and (d) 850-hPa winds (m s^{-1} arrows) and zonal wind anomalies (shading). Anomalies are relative to the annual cycle from 1981–2010, except for SST, which is relative to 1982–2010. Letter symbols denote where each NIO TC attained its initial tropical storm intensity. (Source: Wind data from CFSR [Saha et al. 2014].)

season. Environmental conditions between 15 September and 15 December 2020 were characterized by average to above-average SSTs (Fig. 4.36a) and enhanced convection (Fig. 4.36b) in the region of cyclogenesis. Less favorable wind shear anomalies (>3 m s^{-1}), particularly in the Bay of Bengal, were present around the area of cyclogenesis around Cyclones Nivar and Burevi. Low-level westerly wind anomalies were present around 10°N (Fig. 4.36d).

(II) INDIVIDUAL TROPICAL CYCLONES AND IMPACTS

The first cyclone of the 2020 NIO cyclone season, Super Cyclone Amphan (16–21 May), was the first super cyclonic storm to form (winds ≥120 kt; ≥62 m s^{-1}) over the Bay of Bengal since Cyclone Odisha in 1999 (India Meteorological Department 2021b). Amphan originated from an area of low pressure in the southeastern Bay of Bengal, approximately 1000 km to the southeast of Andhra Pradesh, India. Exceptionally high SSTs

(30°–31°C) and low vertical wind shear (5–7 m s^{-1}) enabled Amphan to intensify from 50 kt (26 m s^{-1}) at 0600 UTC 17 May to 130 kt (67 m s^{-1}) at 2100 UTC 18 May. Amphan reached a maximum intensity of 145 kt (74 m s^{-1}) and a minimum central pressure of 901 hPa, equivalent to an SSHWS Category 5 system before crossing the West Bengal–Bangladesh coastline as a very severe cyclonic storm near Sundarbans with maximum sustained wind speed of 85 kt (44 m s^{-1}). Amphan maintained cyclonic storm intensity (winds ≥ 34 kt; 17 m s^{-1}) for almost 15 hours postlandfall. Damage associated with Amphan was estimated to be at $13.9 billion (U.S. dollars), the costliest cyclone recorded in the basin. In India alone, 98 deaths were reported, along with other fatalities in Bangladesh and Sri Lanka. The Indian state of West Bengal was most impacted by Amphan. In June, the Indian Red Cross Society reported that 2.9 million houses in the state were damaged or destroyed. A 24-hour accumulated rainfall of 240 mm was recorded at Alipore, and storm surge of approximately 15 feet inundated low-lying areas of West Bengal. Bhutan was also affected by flash flooding.

Cyclone Nisarga (2–3 June), originated as a depression in the Arabian Sea and developed into severe cyclonic storm Nisarga on 2 June, aided by an active pulse of the MJO that supported the enhancement of convective activity over the western Arabian Sea (India Meteorological Department 2021a). After recurving toward the northeast, Nisarga intensified into a Severe Cyclonic Storm on 3 June. With a peak intensity of 75 kt (38 m s^{-1}) and a minimum central pressure of 975 hPa, Nisarga made landfall along the Maharashtra coastline, approximately 100 km south of Mumbai, with reported maximum sustained winds of up to 65 kt (33 m s^{-1}). Nisarga maintained cyclonic storm intensity for approximately 7 hours after landfall, tracking toward the northeast throughout Maharashtra and Madhya Pradesh and dissipating quickly thereafter. Nisarga resulted in six fatalities and damage of over $800 million (U.S. dollars) was reported. Farmers living along the coast of Raigad and Ratnagiri suffered devastating losses, and crops including coconut, betel, and mango were destroyed. Significant rainfall (190 mm) was reported at Mahabaleshwar (Maharashtra), and up to 130 mm was reported at Mormugao (Goa) by the Indian Meteorological Department.

After 5 months of inactivity, Very Severe Cyclonic Storm Gati (21–25 November) made landfall across Somalia and was the first very severe cyclonic storm (winds ≥ 64 kt; 33 m s^{-1}) to do so since the start of the satellite era (India Meteorological Department 2020b). Gati originated from a low-pressure area that formed over the central part of the southern Arabian Sea. The MJO, favorable SSTs (29°–30°C), and low wind shear favored the development of Gati, which was defined as a "Midget System" with a compact core and eyewall. Its small size allowed it to undergo rapid intensification, reaching a maximum intensity of 100 kt (51 m s^{-1}) and a minimum central pressure of 967 hPa—a Category 3 SSHWS equivalent system. Gati made landfall near Hafun, with an estimated wind speed of 75 kt (39 m s^{-1}) and maintained cyclonic storm intensity for 15 hours after making landfall. Gati claimed the lives of nine people and brought heavy rainfall, particularly for northern Somalia. Over a 24-hour period, 128 mm of rainfall fell at Bosaso, exceeding the city's average annual rainfall total for the region of 100 mm. Flash flooding was also reported in Socotra Island, Yemen.

Cyclone Nivar (23–25 November) formed in the Bay of Bengal and tracked toward the west-northwest, passing to the northeast of Sri Lanka (India Meteorological Department 2020c). Nivar reached a maximum intensity of 70 kt (36 m s^{-1}) and a minimum central pressure of 981 hPa. On 25 November, Nivar made landfall crossing the Tamil Nadu and Puducherry coasts with recorded wind speeds of 65 kt (33 m s^{-1}). Nivar reportedly resulted in 14 deaths and damage of around $600 million (U.S. dollars). Intense rainfall of 310 mm in a 24-hour period was recorded at Tambaram (Tamil Nadu) and up to 250 mm was recorded at Kodur (Andhra Pradesh), causing flooding around many low-lying regions along the Adyar River. Flooding also closed a number of roads in greater Chennai.

The fifth and final cyclone of the season, Cyclone Burevi (1–5 December), was a relatively weak cyclone that developed from a low-pressure system that formed off the west coast of Aceh (India

Meteorological Department 2020a). Moving west-northwestward, Burevi reached a maximum intensity of 45 kt (23 m s^{-1}) and a minimum central pressure of 999 hPa, before making landfall on the coast of Sri Lanka north of Trincomalee. After passing across northern Sri Lanka, Burevi emerged into the Gulf of Mannar where, due to a lack of middle and upper tropospheric steering winds, it remained stationary close to the coastline of the Ramanathapuram district of India for around 18 hours, before weakening. The recent occurrence of Nivar caused upwelling of cooler waters and a relative cooling of SSTs, thus limiting the intensification of Burevi. Burevi affected Sri Lanka and the Indian states of Tamil Nadu and Keralam, with 11 deaths and five missing persons reported. Intense rainfall occurred, particularly over northern Tamil Nadu and Puducherry, with 360 mm recorded in Kollidam over a 24-hour period. Flooding isolated many rural villages from Chennai and resulted in widespread power outages across Puducherry.

6) South Indian Ocean basin—A. D. Magee and C. J. Schreck

(I) SEASONAL ACTIVITY

The South Indian Ocean TC basin extends south of the equator and from the African coastline to 90°E. While the SIO TC season extends year-round, from July to June, the majority of activity typically occurs between November and April when the Intertropical Convergence Zone is located in the SH. The 2019/20 season includes TCs that occurred from July 2019 to June 2020. Landfalling TCs typically impact Madagascar, Mozambique, and the Mascarene Islands, including Mauritius and Réunion Island; however, impacts can be felt in other locations within the region. The RSMC on La Réunion is the official monitoring agency for TC activity within the SIO basin.

The 2019/20 SIO season had 11 named storms, six cyclones, and three major cyclones, which nearly matches the IBTrACS-JTWC 1981–2010 mean of 10.5, 6.0, and 3.0, respectively (Fig. 4.37). December 2019 was a particularly active month, with three named cyclones (Belna, Ambali, and Calvinia) occurring within the basin. The 2019/20 seasonal ACE index was 53.6 × 10^4 kt^2, which is well below the 1981–2010 climatology of 92.7 × 10^4 kt^2. Cyclone-favorable conditions including anomalously warm SSTs (Fig. 4.38a) likely driven by the strongly positive IOD event of 2019 (Chen

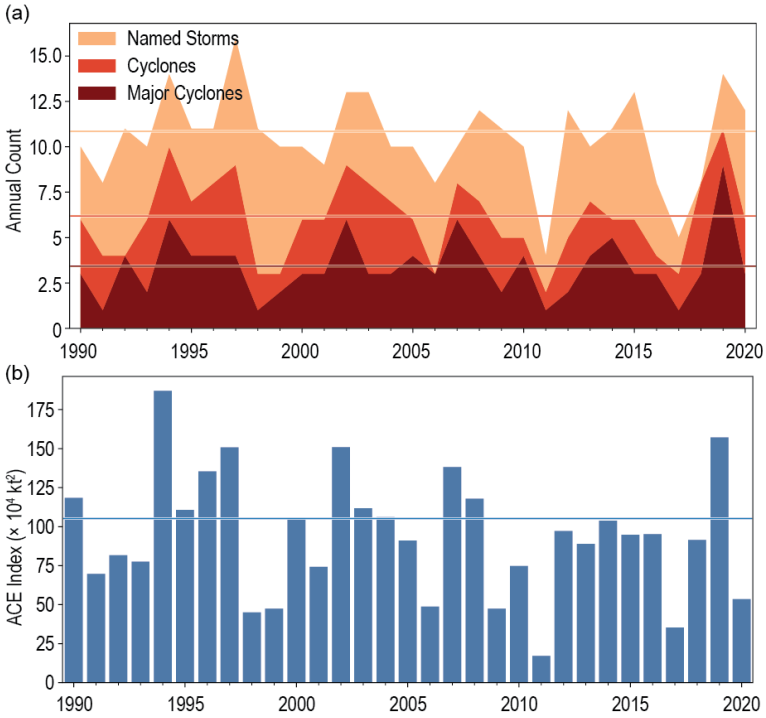

Fig. 4.37. Annual TC statistics for the SIO for 1990–2020: (a) number of named storms, cyclones, and major cyclones and (b) ACE (× 10^4 kt^2). Horizontal lines represent the 1981–2010 climatology.

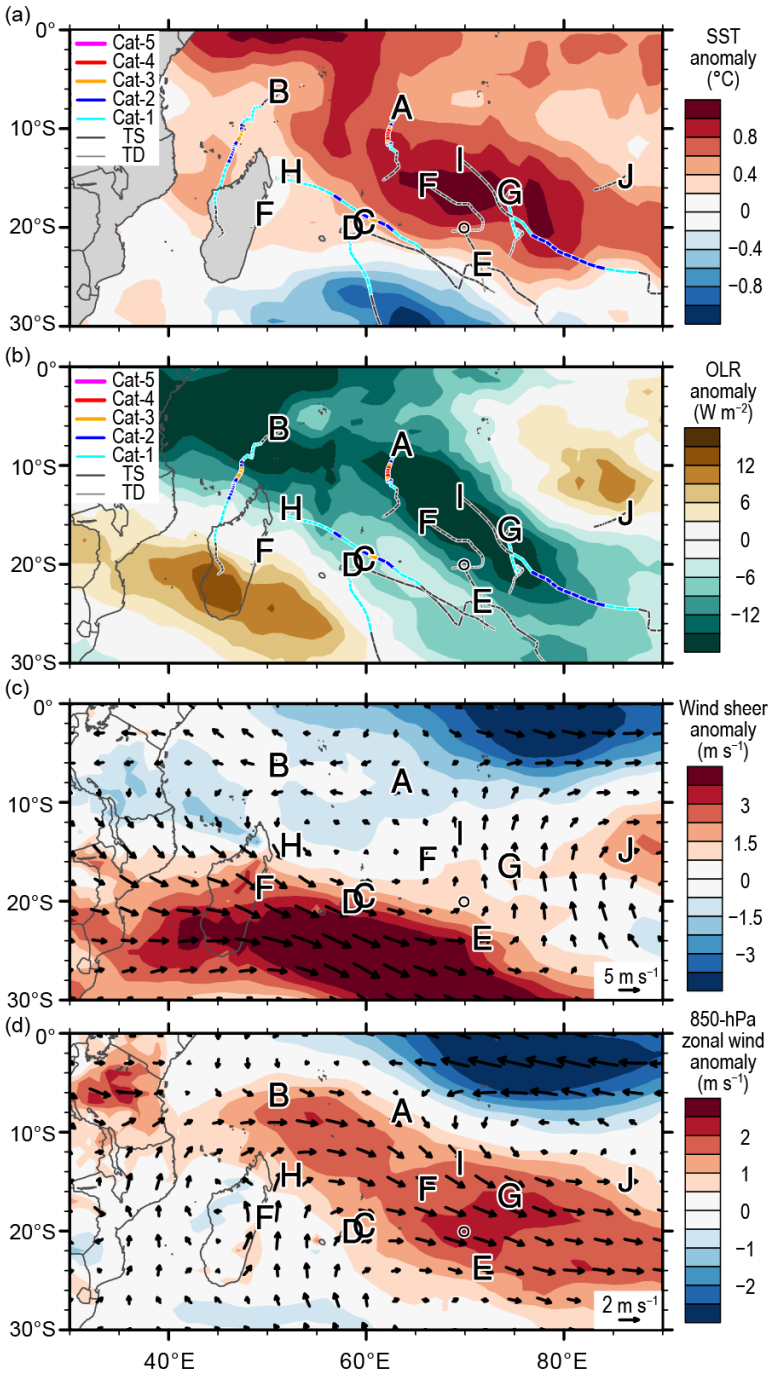

Fig. 4.38. Dec 2019–May 2020 SIO anomaly maps of (a) SST (°C; Banzon and Reynolds 2013), (b) OLR (W m^{-2}; Schreck et al. 2018); (c) 200–850-hPa vertical wind shear (m s^{-1}) vector (arrows) and scalar anomalies (shading), and (d) 850-hPa winds (m s^{-1} arrows) and zonal wind anomalies (shading). Anomalies are relative to the annual cycle from 1981–2010, except for SST, which is relative to 1982–2010. Letter symbols denote where each SIO TC attained its initial tropical storm intensity. (Source: Wind data from CFSR [Saha et al. 2014].)

et al. 2020), large areas of enhanced convection (<–12 W m^{-2}; Fig. 4.38b), and anomalously weak wind shear (Fig. 4.38c) were present in the main development region. Low-level westerly and northwesterly anomalies between ~10°–25°S, extending as far east as 90°E, provided enhanced cyclonic vorticity for many systems (Fig. 4.38d).

(II) NOTEWORTHY TROPICAL CYCLONES AND IMPACTS

The first named cyclone of the season, Cyclone Ambali, developed from a trough between the Seychelles and the Chagos Archipelago (the same extended trough that resulted in Cyclone Belna). Anomalously high SSTs (29°–30°C) promoted rapid intensification of 110 kt (51 m s^{-1}), the most rapid intensification for an SH cyclone in a 24-hour period since 1980. On 6 December, Ambali reached a maximum intensity of 135 kt (69 m s^{-1}) and with a minimum central pressure of 929 hPa, was rated as a Category 4 equivalent system on the SSHWS. Within a few hours of reaching peak intensity, Ambali weakened due to unfavorable vertical wind shear. No significant damage was reported as a result of Ambali.

The second named cyclone of the season, Cyclone Belna, initially started as a tropical disturbance to the west of the Seychelles. While tracking toward the west, Belna intensified over 24 hours and reached a peak intensity of 100 kt (51 m s^{-1}) and a minimum central pressure of 959 hPa, a Category 3 equivalent system on the SSHWS. After fluctuating in intensity, Belna reintensified as the system approached the Soalala district and made landfall along the northwestern coast of Madagascar, maintaining a southerly track over Madagascar before weakening and recurving to the southeast. Nine deaths were reported, with damages estimated to exceed $25 million (U.S. dollars). The primary hospital in Soalala was damaged by flooding, and significant power outages and a shortage of safe drinking water were reported in the region.

Cyclone Calvinia formed from a disturbance first observed by JTWC on 16 December. Calvinia initially tracked toward the south before turning southwest toward Mauritius, slowing down as it did so. At its closest point, Calvinia was approximately 60 km off the coast of Mauritius on 31 December and was tropical storm strength. A precyclonic alert was issued in advance for all three Mascarene Islands, which subsequently closed the Sir Seewoosagur Ramgoolam International Airport and Port Louis Harbour. Calvinia resulted in flooding and power outages for both Mauritius and southern Réunion. In southern Réunion, 325 mm of rainfall was recorded at Dimitile, along with a maximum wind gust of 64 kt (34 m s^{-1}). While tracking south away from Mauritius, Calvinia reintensified and reached peak intensity of 70 kt (36 m s^{-1}) and a minimum central pressure of 973 hPa—a Category 1 equivalent system on the SSHWS.

After a number of systems that achieved tropical storm strength including Diana, Esami, and Francisco, Cyclone Gabekile formed around 1200 km to the northeast of the island of Rodrigues and tracked southward, influenced by a subtropical ridge to the east. On 16 February, Gabekile reached its maximum intensity of 75 kt (39 m s^{-1}) and a minimum central pressure of 978 hPa—a Category 1 equivalent system on the SSHWS. Gabekile did not make landfall and continued to track southward before weakening.

Cyclone Herold formed off the northeastern coast of Madagascar where it remained almost stationary (<100 km from the coastline) for ~24 hours. During this time, Herold continued to intensify, but its slow-moving nature diminished the ocean heat content in the vicinity of the system, resulting in a slight weakening of the system. Herold then tracked to the southeast between the islands of Port Louis and Rodrigues, where it reached a peak intensity of 100 kt (51 m s^{-1}) and a minimum central pressure of 963—a Category 3 equivalent system on the SSHWS. It then tracked toward the southeast and rapidly weakened. Herold claimed the lives of five people and affected areas of Madagascar, Mauritius, and Rodrigues. On 13 March, 95 mm of rainfall was recorded in Sambava (northeastern Madagascar), and riverine flooding was reported from the Andranofosty River. Water levels were reported to be around 2 m, destroying homes, schools, and other essential services. In the Mascarene Islands, maximum sustained winds of 100 kt (51 m s^{-1}) were reported.

The last cyclone of the season, Cyclone Irondro was named approximately 1800 km to the east of Port Louis. On 4 April, Irondro reached a peak intensity of 95 kt (49 m s^{-1}) and minimum central pressure of 958 hPa—a Category 2 system on the SSHWS. Irondro continued to track toward the southeast where it weakened the following day due to unfavorable wind shear and lower SSTs.

7) Australian basin—B.C. Trewin and S. Bond

(I) SEASONAL ACTIVITY

The 2019/20 TC season was below normal in the broader Australian basin (areas south of the equator and between 90°E and 160°E, which includes Australian, Papua New Guinea, and Indonesian areas of responsibility); the Australian Bureau of Meteorology's warning area overlaps both the southern Indian Ocean and southwest Pacific. The season produced eight TCs, below the 1983/84–2010/11 average (1983/84 is the start of consistent satellite coverage over the region) of 10.8, in a season with a strong positive phase of the IOD, and warm waters in the central equatorial Pacific (although below the threshold for a formal El Niño declaration). The 1981–2010 IBTrACS Bureau of Meteorology seasonal averages for the basin are 9.9 named storms, 7.5 TCs, and 4.0 severe (or major) TCs (based on the Australian TC Intensity Scale unless noted otherwise), which compares with the 2019/20 IBTrACS counts of 10, six, and two, respectively (Fig. 4.39).

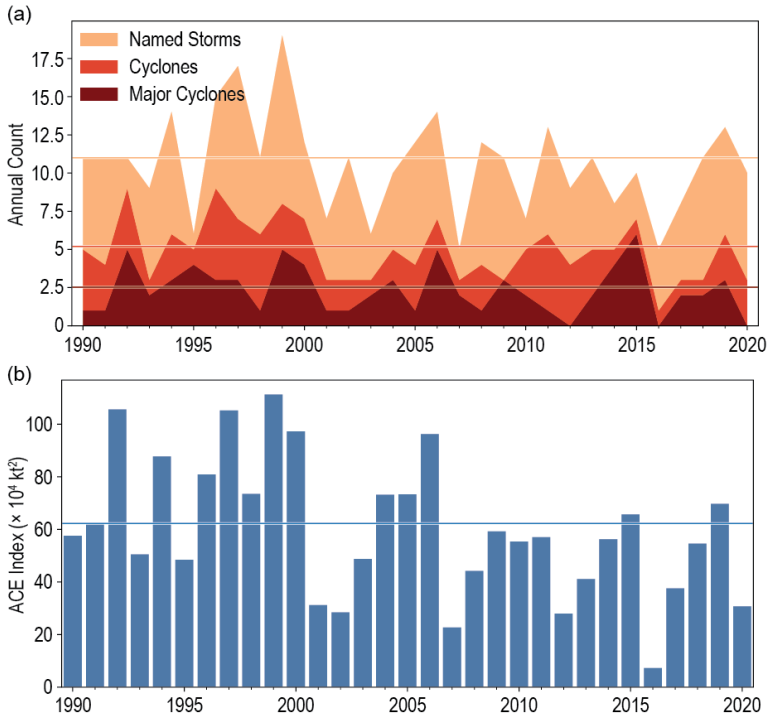

Fig. 4.39. Annual TC statistics for the Australian basin for 1990–2020: (a) number of named storms, cyclones, and major cyclones and (b) ACE (× 10^4 kt^2). The 1981–2010 means (horizontal lines) are included in both (a) and (b).

There were five TCs in the western sector[5] of the broader Australian region during 2019/20, two in the northern sector, and three in the eastern sector. (Esther passed through both the northern and eastern sectors, and Claudia passed through both the northern and western sectors.) Three systems made landfall in Australia as TCs, two in Western Australia and one in the Gulf of Carpentaria, while Tropical Cyclone Harold had major impacts in the southwest Pacific, particularly Vanuatu and the Solomon Islands, after leaving the Australian region (section 4g8).

(II) LANDFALLING AND OTHER SIGNIFICANT TROPICAL CYCLONES[6]

The most significant landfall of the season in the Australian region was Damien. Its precursor low moved west over the Kimberley region of northern Western Australia for several days in early February before emerging over water on 5 February. The low intensified and was named at 0600 UTC on 6 February near 17°S, 120°E. Further intensification took place as Damien turned southwest and then south, moving toward the Pilbara coast, and it reached Category 3 intensity,

[5] The western sector covers areas between 90°E and 125°E. The eastern sector covers areas east of the eastern Australian coast to 160°E, as well as the eastern half of the Gulf of Carpentaria. The northern sector covers areas from 125°E east to the western half of the Gulf of Carpentaria. The western sector incorporates the Indonesian area of responsibility, while the Papua New Guinea area of responsibility is incorporated in the eastern sector.

[6] The Australian TC Intensity Scale is used in this section except as noted otherwise.

with a central pressure of 955 hPa and maximum 10-minute sustained winds of 80 kt (42 m s^{-1}), on the evening of 7 February about 250 km north of Karratha. Damien continued to move south and made landfall near Karratha at close-to-peak intensity at about 0730 UTC on 8 February. It continued to move south over land and weakened below cyclone intensity on 9 February.

Damien caused widespread minor-to-moderate wind damage around Karratha, with a peak wind gust of 105 kt (54 m s^{-1}) at Karratha Airport. The Australian Bureau of Meteorology's radar at Dampier was badly damaged. Heavy rain caused some flooding along the cyclone's path. Both Karratha and Roebourne recorded 235 mm of rain in the 48 hours to 0900 local time on 9 February, with event totals above 100 mm extending south to near Meekatharra.

The other two landfalls of the season were both Category 1 cyclones: Blake in Western Australia and Esther in the Gulf of Carpentaria. Flooding was the main impact for both cyclones. Blake made its first landfall north of Broome on 6 January, then moved out to sea and tracked along the coast before a second landfall near Wallal Downs late on 7 January. Esther only briefly reached TC intensity as it made landfall near the Northern Territory–Queensland border on 24 February. Daily rainfall totals associated with Blake included 153 mm at Derby and 148 mm at Broome on 7 January, but the heaviest rainfall occurred in the interior of Western Australia as a result of moisture from Blake's remnant low; Carnegie received at least 270 mm (amount recorded before the gauge overflowed) on 10 January, the heaviest daily total on record in the Interior district of Western Australia. There was significant flooding in the west Kimberley, with Broome isolated by floodwaters, and in interior regions. Esther's remnant low drifted across the northern parts of the Northern Territory and northern Western Australia for more than a week, with numerous 48-hour rainfall totals in excess of 200 mm in both regions that caused significant flooding.

Claudia and Ferdinand reached severe (or major) cyclone intensity off the Western Australian coast in January and February, respectively. Ferdinand had maximum 10-minute sustained winds of 85 kt (43 m s^{-1}) and a minimum central pressure of 960 hPa, while Claudia reached 75 kt (39 m s^{-1}) and 969 hPa, respectively. Neither system was at cyclone intensity over land, although Claudia's precursor low produced extreme local rainfalls west of Darwin on 11 January. Dum In Mirrie Airstrip had a daily total of 562 mm, a record for the Northern Territory, while nearby Wagait Beach had 515 mm, although impacts were confined to localized flash flooding. Uesi was not a tropical cyclone within the Australian region, but after becoming subtropical it moved into the region, passing close to Lord Howe Island on 14 February, with a wind gust of 83 kt (43 m s^{-1}) at Windy Point. Some wind damage was reported. Gretel and Mangga both remained offshore in the Australian region and had no significant impacts on land.

8) Southwest Pacific basin—J.-M. Woolley, A. Magee, A. M. Lorrey, and H. J. Diamond

(I) SEASONAL ACTIVITY

The 2019/20 Southwest Pacific TC season officially began in November 2019 and ended in April 2020. Storm track data for 2019/20 were gathered from the Fiji Meteorological Service, Australian Bureau of Meteorology, and New Zealand MetService, Ltd. The Southwest Pacific basin (defined by Diamond et al. [2012] as 135°E–120°W) had nine TCs (based on the Australian TC Intensity Scale unless noted otherwise), including three severe (or major) TCs (based on the Australian TC intensity scale). As noted in section 4f1, Fig. 4.40 shows the standardized TC distribution based on the basin spanning the area from 160°E–120°W to avoid overlaps with the Australian basin that could result in double counting of storms; however, it is important to use the climatological definition of the Southwest Pacific basin (Diamond et al. 2012), instead of a political boundary.

The 1981–2010 South Pacific Enhanced Archive of Tropical Cyclones (SPEArTC; Diamond et al. 2012) indicates a seasonal average of 10.4 named TCs including 4.3 severe (or major) TCs. The 2019/20 TC season, therefore, had near-normal activity with nine named tropical cyclones, of which three were severe (Category 3 or above). Severe TCs accounted for one-third of the total number of TCs which is 11% less than last season.

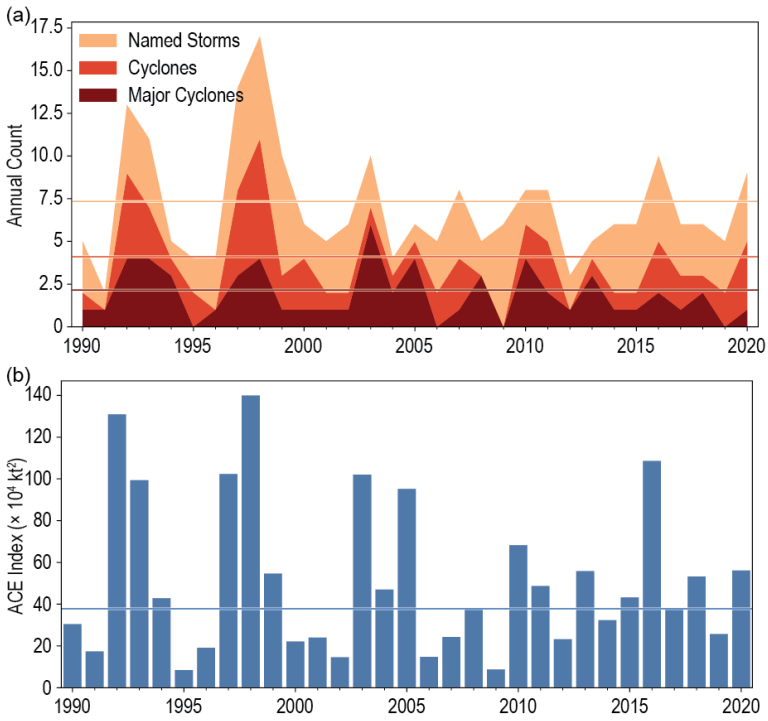

Fig. 4.40. Annual TC statistics for the Southwest Pacific for 1990–2020: (a) number of named storms, cyclones, and major cyclones and (b) ACE (× 10^4 kt^2). The 1981–2010 means (horizontal lines) are included in both (a) and (b).

(II) STORM TRACKS, LANDFALLS, AND IMPACTS

Tropical Cyclone Sarai formed from a southward tracking tropical depression (TD), located west of Tuvalu, which intensified into a Category 1 TC on 26 December while located approximately 100 km west of Rotuma. The storm reached Category 2 intensity on 27 December while it was 220 km west of Nadi in Fiji. The system tracked south and then turned east, passing south of Fiji and delivering heavy wind and rainfall on 27 December. More than 2000 people were evacuated to higher grounds, with two deaths reported. Damage to road infrastructure reached $5 million Fiji dollars ($2.5 million U.S. dollars). TC Sarai weakened to Category 1 intensity on 30 December and passed near Nuku'alofa on 31 December before rapidly deteriorating. Sarai's peak 10-minute sustained winds were 61 kt (31 m s^{-1}), and its minimum central pressure was 975 hPa.

Severe TC Tino was first noted as a tropical disturbance on 11 January to the southeast of Honiara in the Solomon Islands. The system tracked east between the Solomon Islands and Vanuatu and was classified as a Category 1 TC on 16 January before reaching Fiji. Tracking southeast, Tino strengthened to Category 2 intensity on 17 January near Vanua Levu and peaked as a Category 3 severe TC later that day with peak 10-minute sustained winds of 65 kt (33 m s^{-1}) and a minimum central pressure of 964 hPa. Tino passed over several of Tonga's Ha'apai islands on 18 January and gradually weakened as it tracked away to the southeast. By 19 January TC Tino had fully transitioned to an extratropical cyclone.

Severe TC Tino and its precursor tropical disturbance directly impacted the Solomon Islands, Vanuatu, Wallis and Futuna, Fiji, Tonga, and Niue, with the farthest geographic effects also reaching Samoa, American Samoa, Tuvalu, and the Cook Islands. In Tuvalu (500 km north of the storm track), waves up to 8 m combined with a king tide—an exceptionally high tide that occurs during a new or full moon—to cause catastrophic damage, including coastal erosion and flooding. Strong winds also blew roofs off buildings and uprooted trees and crops. In Fiji, over 3000 displaced people were housed across 78 evacuation centers. In Tonga, estimated gusts of 97 kt (50 m s^{-1}) were experienced across the Vava'u and Ha'apai island groups. Storm surge resulted in

damage to crops and main roads, including the causeway connecting the islands of Lifuka and Foa, contributing significantly to power outages in the area (~3000 people were affected overall). In Samoa, trees and billboards were toppled, disrupting power lines and blocking roads; power outages also affected several communities. Despite being 400 km away from Tino's center, strong winds tore off the upper layer of the Niue wharf.

Severe TC Uesi reached Category 1 TC intensity on 9 February while tracking south and positioned approximately 380 km west of Espiritu Santo in Vanuatu. Uesi intensified into a Category 3 TC the following day. On 11 February, Uesi passed west of New Caledonia, resulting in flooding that blocked several bridges and roads. There were also significant power outages and transportation delays. TC Uesi took a south-southwest trajectory and weakened to a Category 2 TC on 12 February. On 14 February, the system began to track to the south-southeast, transitioning to an extratropical storm over the Tasman Sea by the next day. TC Uesi's peak 10-minute sustained winds were 70 kt (36 m s^{-1}) with a minimum central pressure of 975 hPa.

TC Vicky developed from an east-southeast tracking TD that passed near Samoa and just south of Tutuila in American Samoa on 20 February before strengthening into a Category 1 TC later that day. The system then tracked southeast, passing just east of Niue on 21–22 February and weakened as it continued farther south. Vicky's peak 10-minute sustained winds were 40 kt (21 m s^{-1}), and its minimum central pressure was 996 hPa.

TC Wasi developed from a southeast-tracking TD and reached Category 1 TC intensity on 21 February while approximately 125 km north of the Wallis and Futuna Islands. The system strengthened to Category 2 intensity later that day as it tracked toward Samoa but became increasingly disorganized and weakened after passing south of the Samoan Islands. By 23 February, while positioned northwest of Niue, TC Wasi had weakened to below tropical cyclone strength. TC Wasi's peak 10-minute sustained winds were 60 kt (31 m s^{-1}), and its minimum central pressure was 975 hPa.

Tropical Cyclones Vicky and Wasi passed close to Samoa and American Samoa within 2 days of each other. River flooding was reported on the islands of Savai'i and Upolu, and brief power outages occurred in some locations.

Tropical Cyclone Gretel began as a tropical low that was located over the Arafura Sea on 10 March. The system intensified into a Category 1 storm on 14 March after tracking east-southeast, passing over Cape York Peninsula and across much of the Coral Sea. TC Gretel continued to strengthen and reached Category 2 TC intensity on 15 March before passing just south of New Caledonia, resulting in port closures and public transportation cancellations. The system transitioned into an extratropical cyclone on 16 March, while located well north of New Zealand. Gretel's peak 10-minute sustained winds were 54 kt (28 m s^{-1}) with a minimum central pressure of 971 hPa.

Severe TC Harold originated as a tropical low developing within a trough to the east of Papua New Guinea on 1 April and organized into a TC on 2 April near Honiara in the Solomon Islands. Tracking southeast, the system rapidly intensified, reaching SSHWS Category 5 intensity on 5 April. Harold made landfall as an SSHWS Category 5 storm on Espiritu Santo in Vanuatu on 6 April, and then on Pentecost later that day before reemerging over the South Pacific Ocean on an east-southeast trajectory. The system tracked just south of Viti Levu in Fiji, passing over the Kadavu islands early on 8 April before passing 115 km south of Nuku'alofa later that day. The storm weakened over the following days while tracking southeastward and was declared an extratropical TC on 10 April. Harold's peak 10-minute sustained winds were 124 kt (64 m s^{-1}) and its minimum central pressure was 912 hPa.

TC Harold impacted the Solomon Islands as a Category 1 TC, destroying or damaging dozens of homes. Twenty-eight passengers aboard a ferry from Honiara to Malaita Province were washed overboard by large waves caused by the storm, with all but one presumed dead. Harold passed directly over Vanuatu as an SSHWS Category 5 severe TC, the second-strongest TC on

record to make landfall across Vanuatu. Wind gusts exceeding 147 kt (76 m s^{-1}), rainfall totals of 250–450 mm, and a storm surge of up to 0.8 m contributed to torrential rain and flooding, with widespread telecommunication disruptions and a blackout. Significant damage occurred on Espiritu Santo upon Harold's initial landfall, destroying at least half of the buildings in the city of Luganville, with some areas experiencing damage to all structures.

Sidebar 4.2: "Medicanes" (Mediterranean tropical-like cyclones) in 2020—S.H. YOUNG

The traditional areas for tropical cyclone (TC) development in the Northern Hemisphere extend from the Atlantic African coast west across the Atlantic and Pacific Oceans, and the Indian Ocean to the eastern African coast. In the Southern Hemisphere, the eastern limit is around 120°W and extends east from there to the east African coast (Gray 1968). However, the March 2004 formation of Hurricane Catarina in the South Atlantic introduced the concept of tropical development in non-traditional areas (McTaggart-Cowan et.al. 2006).

The Mediterranean basin is another area not considered as an area for tropical development. Many cyclones in this basin are baroclinic synoptic-scale systems, but some are observed to resemble TCs, with an eyewall, an axisymmetric cloud pattern, and a warm core (Emanuel 2005). The fact that an eye feature develops is consistent with tropical development and can occur when winds reach 50 kt (36 m s^{-1}; Vigh et.al. 2012). These Mediterranean tropical-like systems are sometimes referred to as "medicanes," although their classification as TCs or subtropical cyclones are still the subject of debate.

These systems tend to develop under a mid-upper level cold low, often cut off from the westerlies, and where strong thermal gradients exist (Fita 2007). Another reason the Mediterranean is not considered suitable to support tropical development is the existence of low sea surface temperatures, below the 26.5°C often considered to be the minimum threshold for tropical development. McTaggart-Cowen et.al (2015) discuss how development and tropical transition can occur at lower temperatures.

Determining the climatology of medicanes is difficult as there is no formal definition of these systems, and many are identified based on satellite presentation. Cavicchia et al. (2014) used an algorithm that included the cyclone phase space (Hart 2003) to derive a frequency of 1.57 ± 1.30 events per season (maximum sustained wind > 56 kt (29 m s^{-1}), and between 0 and 5 events detected annually over the period 1948–2011. These systems are shown to usually form between September and April.

In 2020, there were three significant medicanes observed in the Mediterranean Sea, with one reportedly reaching hurricane strength of 65 kt (33 m s^{-1}; Fig. SB4.3; USDC 2020), while two displayed eye-like features. The first and strongest of the systems formed north of Libya on 15 September (Fig. SB4.4). Drifting northward, an eye feature developed on 17 September. The publication *Weekly Weather and Crop Bulletin* (USDC 2020) referred to the system as a "hurricane," with reported rainfall of up to 142 mm and likely higher on the windward-facing mountainous terrain. Following landfall, the residual low drifted southward and was last noted west of Crete. Shortly after this

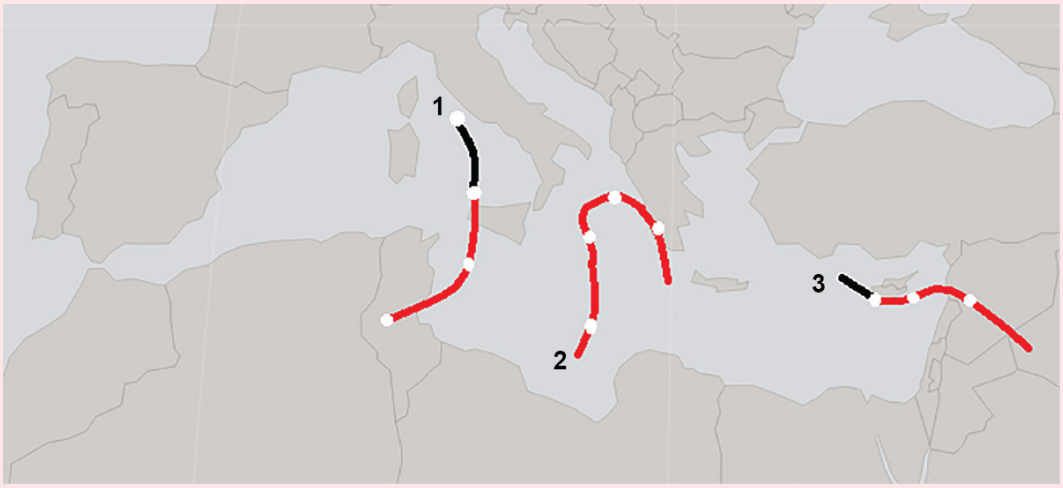

Fig. SB4.3. Tracks of medicanes derived from NCEP/NCAR Reanalysis (Kalnay et al. 1996) and satellite imagery. System #1, 16–19 Sep 2020; System #2, 20–23 Nov 2020; System #3, 14–17 Dec 2020. Black segments of track represent extratropical stage of the system.

system developed, Subtropical Storm Alpha developed in the eastern North Atlantic basin. The upper air aspects of the two systems were similar with cold core cut-off low precursors analyzed at the 700-hPa and 500-hPa levels, a feature that has been previously associated with tropical transition (TT; Pantillon et al. 2013).

The second system (Fig. SB4.4) developed on 20 November from an extratropical system between Italy and Sardinia, and underwent TT prior to crossing the western tip of Sicily (TT of baroclinic systems has been documented as a contributing factor to the development of medicanes [Mazza et al. 2017]). An eye-like feature then developed on 22 November prior to landfall in Tunisia. Maximum winds were estimated to have reached 40 kt (20 m s^{-1}) during the tropical phase.

The last system (Fig. SB4.4) developed south of Turkey on 14 December following the TT of a precursor system, then traveled east along the southern Cypriot coastline. A second landfall occurred along the Syrian coast while the remnant cloud mass tracked to near the Syria-Iraq border. Maximum winds were estimated around 45 kt (23 m s^{-1}). So, while the medicane is an area still open for debate in the tropical cyclone community, it is still an interesting feature, and to have three fairly significant such storms during the 2020 season was a topic considered as sufficiently interesting to highlight in this year's report.

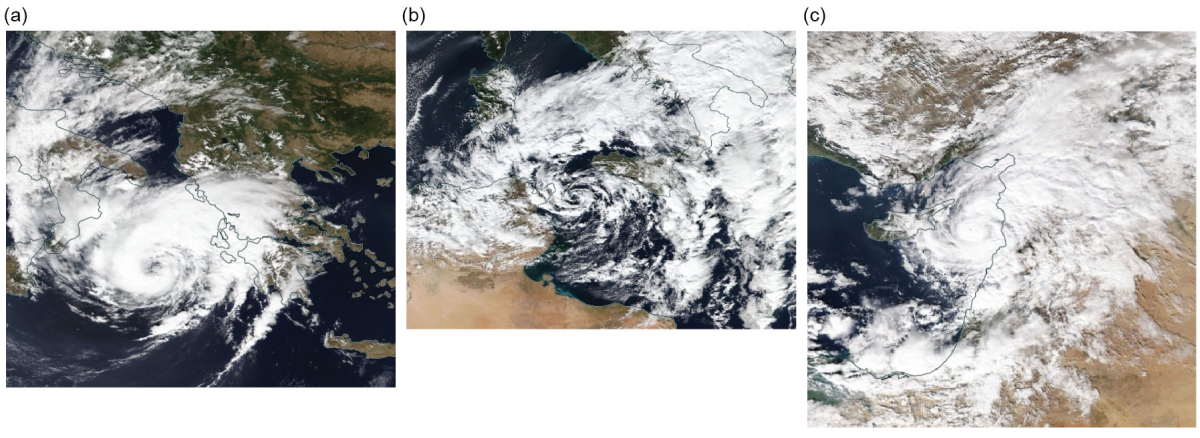

Fig. SB4.4. System #1, 17 Sep (NOAA 20); System #2, 21 Nov (*Aqua*); and System #3, 16 Dec (*Aqua*). Imagery courtesy of NASA Worldview.

h. Tropical cyclone heat potential—R. Domingues, G. J. Goni, J. A. Knaff, I-I Lin, and F. Bringas

In this section, upper-ocean heat content conditions based on the tropical cyclone heat potential (TCHP; e.g., Goni et al. 2009; 2017) are described as anomalies with respect to the long-term mean (1993–2019) and differences to conditions observed in 2019. TCHP quantifies the excess heat content between the sea surface and the depth of the 26°C isotherm (D26, the minimum temperature required for genesis and intensification; Leipper and Volgenau 1972; Dare and McBride 2011) and provides information about the amount of heat stored in the upper ocean and available to fuel TC intensification. As in this section, TCHP is often used as a convenient guide of pre-TC ocean thermal conditions because it carries information about the integrated upper-ocean thermal profile (from sea surface temperature [SST] to D26). High TCHP before a TC usually leads to a smaller amount of SST cooling during a TC, and hence higher enthalpy fluxes from the ocean into the storm, favoring intensification (e.g., Lin et al. 2013). Similarly, upper-ocean salinity is another condition of relevance for TC intensification because freshwater-induced barrier layers may also modulate the upper ocean mixing and cooling during a TC, and hence the air–sea fluxes (e.g., Balaguru 2012; Domingues et al. 2015). Areas in the ocean with pre-TC TCHP values above 50 kJ cm^{-2} have been associated with TC intensification (e.g., Shay et al. 2000; Mainelli et al. 2008; Lin et al. 2014, Knaff et al. 2018), provided that atmospheric conditions are also favorable.

TCHP seasonal anomalies (Fig. 4.41) are calculated as departures from the long-term mean (1993–2019) for the primary months of TC activity in each hemisphere: June–November 2020 in the Northern Hemisphere (NH) and November 2019–April 2020 in the Southern Hemisphere (SH). Differences between the 2020 and 2019 seasons are also analyzed (Fig. 4.42). In any of the regions highlighted in Fig. 4.41 in which TCs are known to form and intensify, TCHP anomalies generally exhibit large spatial and temporal variability due to mesoscale features and short- to long-term modes of variability (e.g., El Niño–Southern Oscillation [ENSO]) and trends.

The 2020 TC season exhibited above the mean 1993–2019 TCHP values in most of the tropical cyclone basins (Fig. 4.41), suggesting that conditions for TC development and intensification were generally favorable in terms of upper-ocean heat content. Notable anomalies with values as large as 30 kJ cm^{-2} above the long-term mean were observed in the North Indian, South Indian, and West Pacific basins, and in the western Caribbean Sea and parts of the Gulf of Mexico. Compared to 2019, TCHP values also increased in all basins (Fig. 4.42), with the exception of the East Pacific, where lower TCHP values observed in 2020 were associated with an ongoing La Niña event (additional details below).

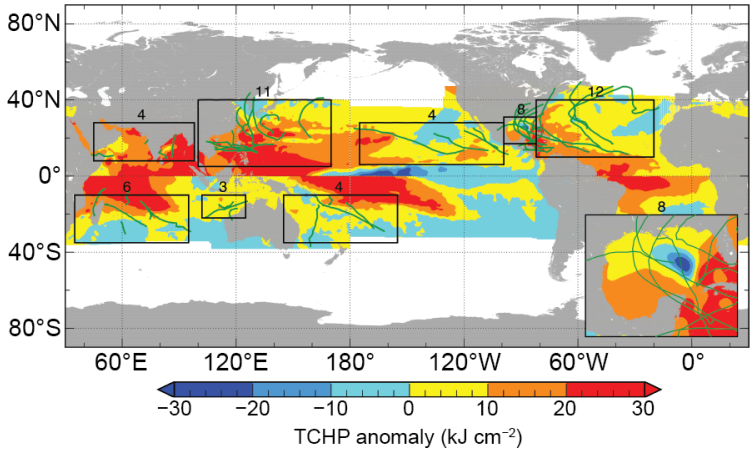

Fig. 4.41. Global anomalies of TCHP during 2020 computed as described in the text. The boxes indicate the seven regions where TCs occur: from left to right, southwest Indian, North Indian, west North Pacific, southeast Indian, southwest Pacific, east Pacific, and North Atlantic (shown as Gulf of Mexico and tropical Atlantic separately). The green lines indicate the trajectories of all tropical cyclones reaching at least Category 1 strength (≥ 64 kt, 34 m s^{-1}) and above during Jun–Nov 2020 in the NH and Nov 2019–Apr 2020 in the SH. The numbers above each box correspond to the number of Category 1 and above cyclones that traveled within each box. The Gulf of Mexico conditions are shown in the inset in the lower right corner.

In the SH, TCHP was anomalously elevated in the southwest Indian Ocean (IO) and beyond the date line during the TC season, and was near normal elsewhere (Fig. 4.41). The observed TC activity was slightly elevated in the southwest IO, which included TC Herold that skirted north of Mauritius. Harold formed near the Solomon Islands and later rapidly intensified before making landfall on Espiritu Santo and Pentecost Islands, Vanuatu, at Category 5 intensity. See section 4g8 for details of this storm.

In the IO, as indicated earlier, all three TC basins exhibited above-normal TCHP conditions (Fig. 4.41), with anomalies up to ~30 kJ cm^{-2} above the long-term average in the North IO basin inside the Bay of Bengal and in the southwest IO basin. All three basins also exhibited notable warming of 20 kJ cm^{-2} compared to values observed in 2019 (Fig. 4.42). In fact, the 2020 TCHP values were generally within the 80–100 kJ cm^{-2} range in the Bay of Bengal and southwest IO basin. Associated with these upper-ocean conditions, the North IO basin exhibited above-average TC activity, the southwest IO basin exhibited slightly above-normal

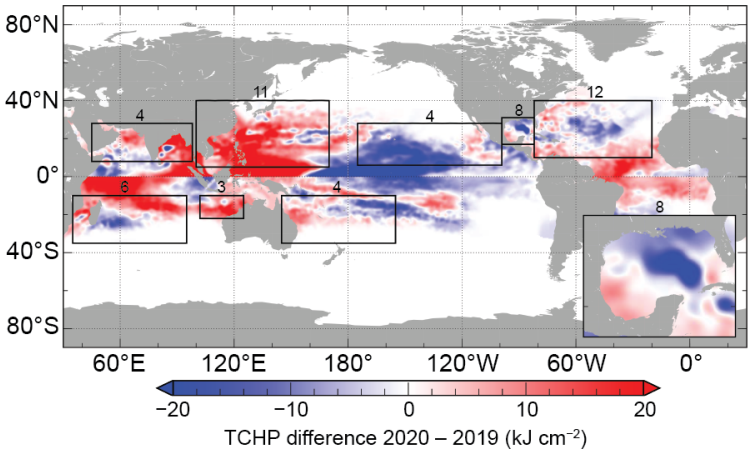

Fig. 4.42. TCHP anomaly difference (kg cm^{-2}) between the 2020 and 2019 tropical cyclone seasons (Jun–Nov in the NH and Nov 2019–Apr 2020 in the SH).

TC activity, and the southeast IO basin exhibited normal activity. With the above-average activity observed in the North IO basin, the 2020 TC season was also the costliest on record, largely due to Cyclone Amphan (16–21 May), which underwent rapid intensification over the anomalously large TCHP in the Bay of Bengal. Similarly, TC Gati, which was the most intense (100 kt, 51 m s^{-1}) to make landfall in Somalia since at least the start of the satellite era, rapidly and unexpectedly intensified over warm TCHP anomalies before striking land.

In the North Pacific, the ENSO state generally plays a large role in defining the large-scale upper-ocean thermal conditions that can impact both the eastern and western North Pacific basins (e.g., Lin et al. 2014, 2020; Zheng et al. 2015). In early 2020, ENSO transitioned from a weak positive phase to a negative phase by mid-year. La Niña conditions developed in August and persisted throughout the entire 2020 TC season. Associated with this ENSO state, TCHP values increased by over 20 kJ cm^{-2} in the western North Pacific and decreased by 20 kJ cm^{-2} in the eastern North Pacific basins with respect to conditions seen in 2019 (Fig. 4.42). Despite these changes, TCHP values were still 10–20 kJ cm^{-2} and 30 kJ cm^{-2} above the long-term mean in the eastern North Pacific and western North Pacific basins, respectively.

While upper-ocean conditions were warmer than normal, which is generally conducive for TC genesis and intensification, TC frequency in the western North Pacific basin was below average in 2020, as often found in La Niña years (Lin et al. 2020). This is because TC frequency in this basin is primarily controlled by atmospheric dynamics (Lin and Chan 2015) rather than by upper-ocean conditions. Despite the overall lower TC activity, large TCHP values likely contributed to the significant intensification of several storms in this basin, as also observed in previous La Niña or La Niña-like years (e.g., TC Megi in 2010, TC Haiyan in 2013; Lin et al. 2014). Among those, Super Typhoon Goni was a notable example. Goni developed south of Guam and followed a similar track to TC Haiyan in 2013 in the southwestern North Pacific main development region (Lin et al. 2014; i.e., east of the Philippines between 5°N and 20°N). As it traveled over areas characterized by high SSTs and high TCHP values (not shown), it experienced a very rapid intensification of 80 kt (41 m s^{-1}) during a 24-hour window, surpassing Haiyan's 60-kt intensification. Goni eventually reached the same record intensity of 170 kt (87 m s^{-1}) as Haiyan in 2013 before making landfall in the Philippines.

In the eastern North Pacific basin, there was an average number of TCs but a below-average number of hurricanes. The La Niña conditions observed in the North Pacific, which were associated with negative SST anomalies (not shown) and lower TCHP values compared to 2019 (Fig. 4.42), likely contributed to the reduced hurricane activity in this basin during the 2020 season.

The North Atlantic basin exhibited TCHP values 10–20 kJ cm^{-2} above the long-term mean in most areas within this basin (Fig. 4.41). Compared with conditions recorded in 2019, TCHP values were also approximately 10 kJ cm^{-2} larger in value for 2020 within the western Caribbean Sea, southern Gulf of Mexico, and along the southeast U.S. coast. A notable increase in TCHP values was observed in the western Caribbean Sea, where TCHP was approximately 30 kJ cm^{-2} larger-than-average conditions, with absolute values typically above 100 kJ cm^{-2} and as large as 140 kJ cm^{-2} (not shown). Associated with these conditions, the North Atlantic basin recorded unprecedented levels of TC activity (section 4g2). From the 14 TCs that reached Category 1 intensity, eight traveled through the open North Atlantic, Caribbean Sea, and Gulf of Mexico (Fig. 4.41). Hurricane Hanna (23–27 July) was the only system to develop and intensify strictly within the Gulf of Mexico. The positive TCHP anomalies observed in 2020 provided the favorable ocean conditions that likely contributed to this very intense TC activity, especially in the western Caribbean Sea, where Category 4 Hurricanes Delta (5–12 October), Eta (31 October–14 November), and Category 4 Hurricane Iota (13–18 November) reached their peak intensity. Iota, for example, rapidly intensified into a Category 5 hurricane over extremely anomalously high TCHP values for November.

In summary, the 2020 TC season exhibited positive TCHP anomalies in most of the TC basins (Fig. 4.41), with notable increases in the upper-ocean heat content in the North Indian, South Indian, and western North Pacific basins, and the western Caribbean and southern Gulf of Mexico. While this could suggest that upper-ocean conditions conducive for TC development and intensification were anomalously favorable in these basins in terms of upper-ocean heat content, in fact, global TC activity in terms of ACE was below normal in association with the La Niña conditions in place. In fact, some of the notable TCs of 2020 highlighted above, such as Cyclone Amphan in the North Indian Ocean, Super Typhoon Goni in the West Pacific, and Hurricane Iota in the Atlantic, underwent rapid intensification while traveling over areas with large TCHP values. In the Pacific Ocean, upper-ocean thermal conditions and TC activity were largely modulated by an ongoing La Niña, which likely caused below-normal TC activity in both the eastern and western North Pacific basins. In the Atlantic, a record number of named TCs were observed, with several major hurricanes reaching their peak intensity while traveling over the anomalously warm western Caribbean Sea. The 2020 season also featured the development of three hurricane-like cyclones or "medicanes" that were recorded within the Mediterranean Sea and were associated with positive SST anomalies.

Chapter 4 – Acronyms

ACE	accumulated cyclone energy
AEJ	African Easterly Jet
AMO	Atlantic Multi-decadal Oscillation
ASO	August–October
CMORPH	CPC Morphing Technique
CNP	central North Pacific
CPC	Climate Prediction Center
DJF	December–February
EASM	East Asian summer monsoon
ENP	East Asian summer monsoon
ENP	eastern North Pacific
ENSO	El Niño–Southern Oscillation
GPCP	Global Precipitation Climatology Project
GPI	genesis potential index
HTCs	hurricanes/typhoons/cyclones
IBTrACS	International Best Track Archive for Climate Stewardship
IO	Indian Ocean
IOB	Indian Ocean basin
IOD	Indian Ocean dipole
ITCZ	Intertropical Convergence Zone
JAS	July–September
JASO	July–October
JJA	June–August
JMA	Japan Meteorological Agency
JTWC	Joint Typhoon Warning Center
MAM	March–May
MDR	main development region
MJO	Madden-Julian Oscillation
NDJ	November–January
NAF	northern Africa
NH	Northern Hemisphere
NIO	North Indian Ocean
OLR	outgoing longwave radiation
OND	October–December
ONI	Oceanic Niño Index
PAGASA	Philippine Atmospheric, Geophysical and Astronomical Services Administration
RMM	Real-time Multivariate MJO
RSMCs	Regional Specialized Meteorological Centers
SAM	Southern Annular Mode
SH	Southern Hemisphere
SON	September–November
SPCZ	South Pacific Convergence Zone
SPEArTC	South Pacific Enhanced Archive of Tropical Cyclones
SSHWS	Saffir-Simpson Hurricane Wind Scale
SST	sea surface temperature

TC	tropical cyclone
TCHP	tropical cyclone heat potential
TD	tropical depression
TT	tropical transition
TUTT	tropical upper-tropospheric trough
WMO	World Meteorological Organization
WNP	western North Pacific
WWBs	westerly wind bursts
YHRV	Yangtze and Huaihe River Valleys

References

Aiyyer, A., and J. Molinari, 2008: MJO and tropical cyclogenesis in the Gulf of Mexico and eastern Pacific: Case study and idealized numerical modeling. *J. Atmos. Sci.*, **65**, 2691–2704, https://doi.org/10.1175/2007JAS2348.1.

Ashok, K., S. K. Behera, S. A. Rao, H. Weng, and T. Yamagata, 2007: El Nino Modoki and its possible teleconnection. *J. Geophys. Res.*, **112**, C11007, https://doi.org/10.1029/2006JC003798.

Balaguru, K., P. Chang, R. Saravanan, L. R. Leung, Z. Xu, M. Li, and J. S. Hsieh, 2012: Ocean barrier layers' effect on tropical cyclone intensification. *Proc. Natl. Acad. Sci. USA*, **109**, 14 343–14 347, https://doi.org/10.1073/pnas.1201364109.

Banzon, V. F., and R. W. Reynolds, 2013: Use of WindSat to extend a microwave-based daily optimum interpolation sea surface temperature time series. *J. Climate*, **26**, 2557–2562, https://doi.org/10.1175/JCLI-D-12-00628.1.

Baxter, S., S. Weaver, J. Gottschalck, and Y. Xue, 2014: Pentad evolution of wintertime impacts of the Madden–Julian oscillation over the contiguous United States. *J. Climate*, **27**, 7356–7367, https://doi.org/10.1175/JCLI-D-14-00105.1.

Behringer, D. W., M. Ji, and A. Leetmaa, 1998: An improved coupled model for ENSO prediction and implications for ocean initialization. Part I: The ocean data assimilation system. *Mon. Wea. Rev.*, **126**, 1013–1021, https://doi.org/10.1175/1520-0493(1998)126<1013:AICMFE>2.0.CO;2.

Bell, G. D., and M. Chelliah, 2006: Leading tropical modes associated with interannual and multi-decadal fluctuations in North Atlantic hurricane activity. *J. Climate*, **19**, 590–612, https://doi.org/10.1175/JCLI3659.1.

——, and Coauthors, 2000: The 1999 North Atlantic Hurricane season [in "Climate Assessment for 1999"]. Bull. Amer. Meteor. Soc., 81 (6), S19–S22, https://doi.org/10.1175/1520-0477(2000)81[s1:CAF]2.0.CO;2.

——, S. Goldenberg, C. Landsea, E. Blake, R. Pasch, M. Chelliah, and K. Mo, 2004: Atlantic hurricane season [in "State of the Climate in 2003"]. *Bull. Amer. Meteor. Soc.*, **85** (6), S20–S24, https://doi.org/10.1175/1520-0477-85.6s.S1.

——, E. Blake, K. C. Mo, C. W. Landsea, R. Pasch, M. Chelliah, and S. B. Goldenberg, 2006: Atlantic Basin [in "State of the Climate in 2005"]. *Bull. Amer. Meteor. Soc.*, **87** (6), S33–S37, https://doi.org/10.1175/1520-0477-87.6.S1.

——, ——, T. B. Kimberlain, C. W. Landsea, J. Schemm, R. J. Pasch, and S. B. Goldenberg, 2011: Atlantic Basin [in "State of the Climate in 2010"]. *Bull. Amer. Meteor. Soc.*, **92**, S115–S121, https://doi.org/10.1175/1520-0477-92.6.S1.

——, ——, C. W. Landsea, C. Wang, J. Schemm, T. Kimberlain, R. J. Pasch, and S. B. Goldenberg, 2017: Atlantic basin [in "State of the Climate in 2016"]. *Bull. Amer. Meteor. Soc.*, **98** (8), S108–S112, https://doi.org/10.1175/2017BAMSStateoftheClimate.1.

——, ——, ——, S. B. Goldenberg, and R. J. Pasch, 2018: Atlantic basin [in "State of the Climate in 2017"]. *Bull. Amer. Meteor. Soc.*, **99** (8), S114–S118, https://doi.org/10.1175/2018BAMSStateoftheClimate.1.

——, M. S. Halpert, and M. L'Heureux, 2019: ENSO and the tropical Pacific [in "State of the Climate in 2018"]. *Bull. Amer. Meteor. Soc.*, **100** (9), S101–S104, https://doi.org/10.1175/2019BAMSStateoftheClimate.1.

——, E. S. Blake, C. W. Landsea, M. Rosencrans, H. Wang, S. B. Goldenberg, and R. J. Pasch, 2020: Atlantic basin [in "State of the Climate in 2019"]. *Bull. Amer. Meteor. Soc.*, **101** (7), S204–S212, https://doi.org/10.1175/BAMS-D-20-0077.1.

Berg, R., 2020: Tropical Storm Amanda (EP022020). National Hurricane Center Tropical Cyclone Rep., 18 pp. https://www.nhc.noaa.gov/data/tcr/EP022020_Amanda.pdf.

Bjerknes, J., 1969: Atmospheric teleconnections from the equatorial Pacific. *Mon. Wea. Rev.*, **97**, 163–172, https://doi.org/10.1175/1520-0493(1969)097<0163:ATFTEP>2.3.CO;2.

Brown, D. P., 2020: Unnamed Tropical Storm (formerly Tropical Depression Seven-E) (EP072020). National Hurricane Center Tropical Cyclone Rep., 9 pp. https://www.nhc.noaa.gov/data/tcr/EP072020_Unnamed.pdf.

Camargo, S. J., and A. H. Sobel, 2005: Western North Pacific tropical cyclone intensity and ENSO. *J. Climate*, **18**, 2996–3006, https://doi.org/10.1175/JCLI3457.1.

——, A. W. Robertson, S. J. Gaffney, P. Smyth, and M. Ghil, 2007a: Cluster analysis of typhoon tracks: Part II: Large-scale circulation and ENSO. *J. Climate*, **20**, 3654–3676, https://doi.org/10.1175/JCLI4203.1.

——, K. A. Emanuel, and A. H. Sobel, 2007b: Use of a genesis potential index to diagnose ENSO effects on tropical cyclone genesis. *J. Climate*, **20**, 4819–4834, https://doi.org/10.1175/JCLI4282.1.

——, M. C. Wheeler, and A. H. Sobel, 2009: Diagnosis of the MJO modulation of tropical cyclogenesis using an empirical index. *J. Atmos. Sci.*, **66**, 3061–3074, https://doi.org/10.1175/2009JAS3101.1.

Cangialosi, J. P., 2020: Tropical Depression One-E (EP012020). National Hurricane Center Tropical Cyclone Rep., 7 pp. https://www.nhc.noaa.gov/data/tcr/EP012020_One-E.pdf.

Cassou, C., 2008: Intraseasonal interaction between the Madden Julian Oscillation and the North Atlantic Oscillation. *Nature*, **455**, 523–527, https://doi.org/10.1038/nature07286.

Cavicchia, L., H. von Storch, and S. Gualdi, 2014: A long-term climatology of medicanes. *Climate Dyn.*, **43**, 1183–1195, https://doi.org/10.1007/s00382-013-1893-7.

Chen, L., J.-J. Luo, and A. D. Magee, 2020: Indian Ocean dipole [in "State of the Climate in 2019"]. *Bull. Amer. Meteor. Soc.*, **100** (9), S229–S232, https://doi.org/10.1175/BAMS-D-20-0077.1.

Chia, H. H., and C. F. Ropelewski, 2002: The interannual variability in the genesis location of tropical cyclones in the northwest Pacific. *J. Climate*, **15**, 2934–2944, https://doi.org/10.1175/1520-0442(2002)015<2934:TIVITG>2.0.CO;2.

Clarke, A. J., 2010: Analytical theory for the quasi-steady and low-frequency equatorial ocean response to wind forcing: The "tilt" and "warm water volume" modes. *J. Phys. Oceanogr.*, **40**, 121–137, https://doi.org/10.1175/2009JPO4263.1.

CNN, 2020: Cyclone Amphan caused an estimated $13.2 billion in damage in India's West Bengal: Government source. 22 May, accessed 10 January 2021, https://edition.cnn.com/2020/05/22/weather/cyclone-amphan-damage-intl-hnk/index.html.

Dare, R. A., and J. L. McBride, 2011: Sea surface temperature response to tropical cyclones. *Mon. Wea. Rev.*, **139**, 3798–3808, https://doi.org/10.1175/MWR-D-10-05019.1.

Diamond, H. J., and J. A. Renwick, 2015: The climatological relationship between tropical cyclones in the southwest pacific and the Madden–Julian Oscillation. *Int. J. Climatol.*, **35**, 676–686, https://doi.org/10.1002/joc.4012.

——, and C. J. Schreck III, Eds., 2017: The tropics [in "State of the Climate in 2016"]. *Bull. Amer. Meteor. Soc.*, **98** (8), S93–S128, https://doi.org/10.1175/2017BAMSStateoftheClimate.1.

——, and ——, Eds., 2018: The tropics [in "State of the Climate in 2017"]. *Bull. Amer. Meteor. Soc.*, **99** (8), S101–S141, https://doi.org/10.1175/2018BAMSStateoftheClimate.1.

——, and ——, Eds., 2019: The tropics [in "State of the Climate in 2018"]. *Bull. Amer. Meteor. Soc.*, **100** (9), S101–S140, https://doi.org/10.1175/2019BAMSStateoftheClimate.1.

——, and ——, Eds., 2020: The tropics [in "State of the Climate in 2019"]. *Bull. Amer. Meteor. Soc.*, **100** (8), S185–S238, https://doi.org/10.1175/BAMS-D-20-0077.1.

——, A. M. Lorrey, K. R. Knapp, and D. H. Levinson, 2012: Development of an enhanced tropical cyclone tracks database for the southwest Pacific from 1840 to 2011. *Int. J. Climatol.*, **32**, 2240–2250, https://doi.org/10.1002/joc.2412.

Domingues, R., and Coauthors, 2015: Upper ocean response to Hurricane Gonzalo (2014): Salinity effects revealed by targeted and sustained underwater glider observations. *Geophys. Res. Lett.*, **42**, 7131–7138, https://doi.org/10.1002/2015GL065378.

Dube, S. K., D. Rao, P. C. Sinha, T. S. Murty, and N. Bahuluyan, 1997: Storm surge in the Bay of Bengal and Arabian Sea: The problem and its prediction. *Mausam* **48**, 288–304.

Ebita, A., and Coauthors, 2011: The Japanese 55-year reanalysis "JRA-55": An interim report. *Sci. Online Lett. Atmos.*, **7**, 149–152, https://doi.org/10.2151/sola.2011-038.

Emanuel, K. A., 1988: The maximum intensity of hurricanes. *J. Atmos. Sci.*, **45**, 1143–1155, https://doi.org/10.1175/1520-0469(1988)045<1143:TMIOH>2.0.CO;2.

——, 2005: Genesis and maintenance of "Mediterranean Hurricanes." *Adv. Geosci.*, **2**, 217–220, https://doi.org/10.5194/adgeo-2-217-2005.

——, and D. S. Nolan, 2004: Tropical cyclone activity and the global climate system. 26th Conf. on Hurricanes and Tropical Meteorology, Miami, FL, Amer. Meteor. Soc., 10A.2, https://ams.confex.com/ams/26HURR/techprogram/paper_75463.htm.

Enfield, D. B., and A. M. Mestas-Nuñez, 1999: Multiscale variabilities in global sea surface temperatures and their relationships with tropospheric climate patterns. *J. Climate*, **12**, 2719–2733, https://doi.org/10.1175/1520-0442(1999)012<2719:MVIGSS>2.0.CO;2.

Fita, L., R. Romero, A. Luque, K. Emanuel, and C. Ramis, 2007: Analysis of the environments of seven Mediterranean tropical-like storms using an axisymmetric, nonhydrostatic, cloud resolving model. *Nat. Hazards Earth Syst. Sci.*, **7**, 41–56, https://doi.org/10.5194/nhess-7-41-2007.

Frank, W. M., and P. E. Roundy, 2006: The role of tropical waves in tropical cyclogenesis. *Mon. Wea. Rev.*, **134**, 2397–2417, https://doi.org/10.1175/MWR3204.1.

Goldenberg, S. B., and L. J. Shapiro, 1996: Physical mechanisms for the association of El Niño and West African rainfall with Atlantic major hurricane activity. *J. Climate*, **9**, 1169–1187, https://doi.org/10.1175/1520-0442(1996)009<1169:PMFTAO>2.0.CO;2.

——, C. W. Landsea, A. M. Mestas-Nuñez, and W. M. Gray, 2001: The recent increase in Atlantic hurricane activity: Causes and implications. *Science*, **293**, 474–479, https://doi.org/10.1126/science.1060040.

Goni, G. J., and Coauthors, 2009: Applications of satellite-derived ocean measurements to tropical cyclone intensity forecasting. *Oceanography*, **22**, 176–183, https://doi.org/10.5670/oceanog.2009.78.

——, and Coauthors, 2017: Autonomous and Lagrangian Ocean observations for Atlantic tropical cyclone studies and forecasts. *Oceanography*, **30**, 92–103, https://doi.org/10.5670/oceanog.2017.227.

Gray, W., 1968: Global view of the origin of tropical disturbances and storms. *Mon. Wea. Rev.*, **96**, 669–700, https://doi.org/10.1175/1520-0493(1968)096<0669:GVOTOO>2.0.CO;2.

——, 1990: Strong association between West African rainfall and U.S. landfall of intense hurricanes. *Science*, **249**, 1251–1256, https://doi.org/10.1126/science.249.4974.1251.

Guo, Y., X. Jiang, and D. E. Waliser, 2014: Modulation of the convectively coupled Kelvin waves over South America and the tropical Atlantic Ocean in association with the Madden–Julian oscillation. *J. Atmos. Sci.*, **71**, 1371–1388, https://doi.org/10.1175/JAS-D-13-0215.1.

Halpert, M. S., and C. F. Ropelewski, 1992: Surface temperature patterns associated with the southern oscillation. *J. Climate*, **5**, 577–593, https://doi.org/10.1175/1520-0442(1992)005<0577:STPAWT>2.0.CO;2.

Hart, R. E., 2003: A cyclone phase space derived from thermal wind and thermal asymmetry. *Mon. Wea. Rev.*, **131**, 585–616, https://doi.org/10.1175/1520-0493(2003)131<0585:ACPSDF>2.0.CO;2.

Hastenrath, S., 1990: Decadal-scale changes of the circulation in the tropical Atlantic sector associated with Sahel drought. *Int. J. Climatol.*, **10**, 459–472, https://doi.org/10.1002/joc.3370100504.

Hendon, H., C. Zhang, and J. Glick, 1999: Interannual variation of the Madden–Julian oscillation during austral summer. *J. Climate*, **12**, 2538–2550, https://doi.org/10.1175/1520-0442(1999)012<2538:IVOTMJ>2.0.CO;2.

Hersbach, H., and Coauthors, 2020: The ERA5 global reanalysis. *Quart. J. Roy. Meteor. Soc.*, **146**, 1999–2049, https://doi.org/10.1002/qj.3803.

Huang, B., and Coauthors, 2017: Extended reconstructed sea surface temperature, version 5 (ERSSTv5): Upgrades, validations, and intercomparisons. *J. Climate*, **30**, 8179–8205, https://doi.org/10.1175/JCLI-D-16-0836.1.

Huffman, G. J., R. F. Adler, D. T. Bolvin, and G. Gu, 2009: Improving the global precipitation record: GPCP Version 2.1. *Geophys. Res. Lett.*, **36**, L17808, https://doi.org/10.1029/2009GL040000.

India Meteorological Department, 2020a: Cyclonic storm 'BUREVI' over the Bay of Bengal (30th November - 5th December 2020): A preliminary report. 20 pp., https://static.pib.gov.in/WriteReadData/userfiles/Summary-BUREVI_12122020.pdf.

——, 2020b: Very severe cyclonic storm 'GATI' over the Arabian Sea (21-24 November 2020): A report. 33 pp., http://rsmcnewdelhi.imd.gov.in/uploads/report/26/26_fd784d_gati.pdf.

——, 2020c: Very severe cyclonic storm 'NIVAR' over the Bay of Bengal (22nd-27th November 2020): A report. 42 pp., http://www.rsmcnewdelhi.imd.gov.in/uploads/report/26/26_891f5a_NIVAR.pdf.

——, 2020d: Severe cyclonic storm "NISARGA" over the Arabian Sea (01-04 June 2020): Summary. 35 pp., http://www.rsmcnewdelhi.imd.gov.in/images/pdf/publications/preliminary-report/nisarga.pdf.

——, 2021: Super cyclonic storm "AMPHAN" over Southeast Bay of Bengal (16 May - 21 May 2020): A report. 73 pp., http://www.rsmcnewdelhi.imd.gov.in/uploads/report/26/26_936e63_amphan.pdf.

Island Climate Update, 2020: The island climate update. National Institute of Water and Atmospheric Research, New Zealand, https://niwa.co.nz/climate/island-climate-update.

Joyce, R. J., J. E. Janowiak, P. A. Arkin, and P. Xie, 2004: CMORPH: A method that produces global precipitation estimates from passive microwave and infrared data at high spatial and temporal resolution. *J. Hydrometeor.*, **5**, 487–503, https://doi.org/10.1175/1525-7541(2004)005<0487:CAMTPG>2.0.CO;2.

Kalnay, E., and Coauthors, 1996: The NCEP/NCAR 40-Year Reanalysis Project. *Bull. Amer. Meteor. Soc.*, **77**, 437–471, https://doi.org/10.1175/1520-0477(1996)077<0437:TNYRP>2.0.CO;2.

Kayano, M., and V. Kousky, 1999: Intraseasonal (30-60 day) variability in the global tropics: Principal modes and their evolution. *Tellus*, **51**, 373–386, https://doi.org/10.3402/tellusa.v51i3.13459.

Kiladis, G. N., and K. M. Weickmann, 1992: Circulation anomalies associated with tropical convection during northern winter. *Mon. Wea. Rev.*, **120**, 1900–1923, https://doi.org/10.1175/1520-0493(1992)120<1900:CAAWTC>2.0.CO;2.

——, K. H. Straub, and P. T. Haertel, 2005: Zonal and vertical structure of the Madden–Julian oscillation. *J. Atmos. Sci.*, **62**, 2790–2809, https://doi.org/10.1175/JAS3520.1.

——, M. C. Wheeler, P. T. Haertel, K. H. Straub, and P. E. Roundy, 2009: Convectively coupled equatorial waves. *Rev. Geophys.*, **47**, RG2003, https://doi.org/10.1029/2008RG000266.

Klotzbach, P. J., 2010: On the Madden–Julian oscillation–Atlantic hurricane relationship. *J. Climate*, **23**, 282–293, https://doi.org/10.1175/2009JCLI2978.1.

Knaff, J. A., C. R. Sampson, and K. D. Musgrave, 2018: An operational rapid intensification prediction aid for the western North Pacific. *Wea. Forecasting*, **33**, 799–811, https://doi.org/10.1175/WAF-D-18-0012.1.

Knapp, K. R., M. C. Kruk, D. H. Levinson, H. J. Diamond, and C. J. Neumann, 2010: The International Best Track Archive for Climate Stewardship (IBTrACS): Unifying tropical cyclone data. *Bull. Amer. Meteor. Soc.*, **91**, 363–376, https://doi.org/10.1175/2009BAMS2755.1.

——, J. A. Knaff, C. R. Sampson, G. M. Riggio, and A. D. Schnapp, 2013: A pressure-based analysis of the historical western North Pacific tropical cyclone intensity record. *Mon. Wea. Rev.*, **141**, 2611–2631, https://doi.org/10.1175/MWR-D-12-00323.1.

Knutson, T. R., and K. M. Weickmann, 1987: 30–60 day atmospheric oscillations: Composite life cycles of convection and circulation anomalies. *Mon. Wea. Rev.*, **115**, 1407–1436, https://doi.org/10.1175/1520-0493(1987)115<1407:DAOCLC>2.0.CO;2.

Kousky, V. E., and M. T. Kayano, 1994: Principal modes of outgoing longwave radiation and 250-mb circulation for the South American sector. *J. Climate*, **7**, 1131–1143, https://doi.org/10.1175/1520-0442(1994)007<1131:PMOOLR>2.0.CO;2.

Krishnamurti, T. N., and D. Subrahmanyam, 1982: The 30–50 day mode at 850 mb during MONEX. *J. Atmos. Sci.*, **39**, 2088–2095, https://doi.org/10.1175/1520-0469(1982)039<2088:TDMAMD>2.0.CO;2.

Kruk, M. C., and C. J. Schreck, 2019: Eastern North Pacific basin [in "State of the Climate in 2018"]. *Bull. Amer. Meteor. Soc.*, **100**, S121–S124, https://doi.org/10.1175/2019BAMSStateoftheClimate.1.

Kumar, A., and Z.-Z. Hu, 2014: Interannual and interdecadal variability of ocean temperature along the equatorial Pacific in conjunction with ENSO. *Climate Dyn.*, **42**, 1243–1258, https://doi.org/10.1007/s00382-013-1721-0.

Landsea, C. W., and J. L. Franklin, 2013: Atlantic hurricane database uncertainty and presentation of a new database format. *Mon. Wea. Rev.*, **141**, 3576–3592, https://doi.org/10.1175/MWR-D-12-00254.1.

——, W. M. Gray, P. W. Mielke, and K. J. Berry, 1992: Long-term variations of western Sahelian monsoon rainfall and intense U.S. landfalling hurricanes. *J. Climate*, **5**, 1528–1534, https://doi.org/10.1175/1520-0442(1992)005<1528:LTVOWS>2.0.CO;2.

——, G. D. Bell, W. M. Gray, and S. B. Goldenberg, 1998: The extremely active 1995 Atlantic hurricane season: Environmental conditions and verification of seasonal forecasts. *Mon. Wea. Rev.*, **126**, 1174–1193, https://doi.org/10.1175/1520-0493(1998)126<1174:TEAAHS>2.0.CO;2.

——, G. A. Vecchi, L. Bengtsson, and T. R. Knutson, 2010: Impact of duration thresholds on Atlantic tropical cyclone counts. *J. Climate*, **23**, 2508–2519, https://doi.org/10.1175/2009JCLI3034.1.

Latto, A., 2020: Hurricane Douglas (EP082020). National Hurricane Center Tropical Cyclone Rep., 14 pp. https://www.nhc.noaa.gov/data/tcr/EP082020_Douglas.pdf.

Lau, W. K.-M., and D. E. Waliser, 2012: Intraseasonal Variability in the Atmosphere-Ocean Climate System. Springer, 642 pp.

Leipper, D. F., and D. Volgenau, 1972: Hurricane heat potential of the Gulf of Mexico. *J. Phys. Oceanogr.*, **2**, 218–224, https://doi.org/10.1175/1520-0485(1972)002<0218:HHPOTG>2.0.CO;2.

Liebmann, B., and C. A. Smith, 1996: Description of a complete (interpolated) outgoing longwave radiation dataset. *Bull. Amer. Meteor. Soc.*, **77**, 1275–1277, https://doi.org/10.1175/1520-0477-77.6.1274.

Lin, H., G. Brunet, and J. Derome, 2009: An observed connection between the North Atlantic oscillation and the Madden–Julian oscillation. *J. Climate*, **22**, 364–380, https://doi.org/10.1175/2008JCLI2515.1.

Lin, I. I., and J. Chan, 2015: Recent decrease in typhoon destructive potential and global warming implications. *Nat. Commun.*, **6**, 7182, https://doi.org/10.1038/ncomms8182.

——, and Coauthors, 2013: An ocean coupling potential intensity index for tropical cyclones. *Geophys. Res. Lett.*, **40**, 1878–1882, https://doi.org/10.1002/grl.50091.

——, I.-F. Pun, and C.-C. Lien, 2014: "Category-6" Supertyphoon Haiyan in global warming hiatus: Contribution from subsurface ocean warming. *Geophys. Res. Lett.*, **41**, 8547–8553, https://doi.org/10.1002/2014GL061281.

——, and Coauthors, 2020: ENSO and tropical cyclones. *El Niño Southern Oscillation in a Changing Climate*, *Geophys. Monogr.*, Vol. 253, Amer. Geophys. Union, 377–408, https://doi.org/10.1002/9781119548164.ch17.

Juo, J. J., R. Zhang, S. K. Behera, Y. Masumoto, F.-F. Jin, R. Lukas, and T. Yamagata, 2010: Interaction between El Niño and extreme Indian Ocean dipole. *J. Climate*, **23**, 726–742, https://doi.org/10.1175/2009JCLI3104.1.

——, W. Sasaki, and Y. Masumoto, 2012: Indian Ocean warming modulates Pacific climate change. *Proc. Natl. Acad. Sci. USA*, **109**, 18 701–18 706, https://doi.org/10.1073/pnas.1210239109.

Madden, R., and P. Julian, 1971: Detection of a 40–50 day oscillation in the zonal wind in the tropical Pacific. *J. Atmos. Sci.*, **28**, 702–708, https://doi.org/10.1175/1520-0469(1971)028<0702:DOADOI>2.0.CO;2.

—., and ——, 1972: Description of global-scale circulation cells in the tropics with a 40–50 day period. *J. Atmos. Sci.*, **29**, 1109–1123, https://doi.org/10.1175/1520-0469(1972)029<1109:DOGSCC>2.0.CO;2.

——, and ——, 1994: Observations of the 40–50-day tropical oscillation: A review. *Mon. Wea. Rev.*, **122**, 814–837, https://doi.org/10.1175/1520-0493(1994)122<0814:OOTDTO>2.0.CO;2.

Mainelli, M., M. DeMaria, L. Shay, and G. Goni, 2008: Application of oceanic heat content estimation to operational forecasting of recent Atlantic category 5 hurricanes. *Wea. Forecasting*, **23**, 3–16, https://doi.org/10.1175/2007WAF2006111.1.

Maloney, E. D., and D. L. Hartmann, 2001: The Madden–Julian oscillation, barotropic dynamics, and North Pacific tropical cyclone formation. Part I: Observations. *J. Atmos. Sci.*, **58**, 2545–2558, https://doi.org/10.1175/1520-0469(2001)058<2545:TMJOBD>2.0.CO;2.

Matthews, A. J., 2008: Primary and successive events in the Madden–Julian Oscillation. *Quart. J. Roy. Meteor. Soc.*, **134**, 439–453, https://doi.org/10.1002/qj.224.

Mazza, E., U. Ulbrich, and R. Klein, 2017: The tropical transition of the October 1996 medicane in the western Mediterranean Sea: A warm seclusion event. *Mon. Wea. Rev.*, **145**, 2575–2595, https://doi.org/10.1175/MWR-D-16-0474.1.

McTaggart-Cowan, R., L. F. Bosart, C. A. Davis, E. H. Atallah, J. R. Gyakum, and K. A. Emanuel, 2006: Analysis of Hurricane Catarina (2004). *Mon. Wea. Rev.*, **134**, 3029–3053, https://doi.org/10.1175/MWR3330.1.

McTaggart-Cowan, R., E. L. Davies, J. G. Fairman Jr., T. J. Galarneau Jr., and D. M. Schultz, 2015: Revisiting the 26.5°C sea surface temperature threshold for tropical cyclone development. *Bull. Amer. Meteor. Soc.*, **96**, 1929–1943, https://doi.org/10.1175/BAMS-D-13-00254.1.

Mo, K. C., 2000: The association between intraseasonal oscillations and tropical storms in the Atlantic Basin. *Mon. Wea. Rev.*, **128**, 4097–4107, https://doi.org/10.1175/1520-0493(2000)129<4097:TABIOA>2.0.CO;2.

Mo, K. C., and V. E. Kousky, 1993: Further analysis of the relationship between circulation anomaly patterns and tropical convection. *J. Geophys. Res.*, **98**, 5103–5113, https://doi.org/10.1029/92JD02952.

——, and R. W. Higgins, 1998: The Pacific–South American modes and tropical convection during the Southern Hemisphere winter. *Mon. Wea. Rev.*, **126**, 1581–1596, https://doi.org/10.1175/1520-0493(1998)126<1581:TPSAMA>2.0.CO;2.

Münnich, M., and J. D. Neelin, 2005: Seasonal influence of ENSO on the Atlantic ITCZ and equatorial South America. *Geophys. Res. Lett.*, **32**, L21709, https://doi.org/10.1029/2005GL023900.

Nobre, P., and J. Shukla, 1996: Variations of sea surface temperature, wind stress and rainfall over the tropical Atlantic and South America. *J. Climate*, **9**, 2464–2479, https://doi.org/10.1175/1520-0442(1996)009<2464:VOSSTW>2.0.CO;2.

Pantillon, F., J.-P. Chaboureau, P. J. Mascart, and C. Lac, 2013: Predictability of a Mediterranean tropical-like storm downstream of the extratropical transition of Hurricane Helene (2006). *Mon. Wea. Rev.*, **141**, 1943–1962, https://doi.org/10.1175/MWR-D-12-00164.1.

Papin, P. P., L. F. Bosart, and R. D. Torn, 2017: A climatology of Central American gyres. *Mon. Wea. Rev.*, **145**, 1983–2000, https://doi.org/10.1175/MWR-D-16-0411.1.

Pasch, R. J., R. Berg, D. P. Roberts, and P. P. Papin, 2021: Hurricane Laura (AL132020). National Hurricane Center Tropical Cyclone Rep., 75 pp, https://www.nhc.noaa.gov/data/tcr/AL132020_Laura.pdf.

Penland, C., and P. D. Sardeshmukh, 1995: The optimal growth of tropical sea surface temperature anomalies. *J. Climate*, **8**, 1999–2024, https://doi.org/10.1175/1520-0442(1995)008<1999:TOGOTS>2.0.CO;2.

Pezza, A. B., and A. S. Coelho, 2019: Atlantic [in "State of the Climate in 2018"]. *Bull. Amer. Meteor. Soc.*, **100** (9), S109–S110, https://doi.org/10.1175/2019BAMSStateoftheClimate.1.

Qiao, S., and Coauthors, 2021: The longest 2020 Meiyu season over the past 60 years: Subseasonal perspective and its predictions. *Geophys. Res. Lett.*, **48**, e2021GL093596, https://doi.org/10.1029/2021GL093596.

Raga, G. B., B. Bracamontes-Ceballos, L. Farfán, and R. Romero-Centeno, 2013: Landfalling tropical cyclones on the Pacific coast of Mexico: 1850–2010. *Atmósfera*, **26**, 209–220, https://doi.org/10.1016/S0187-6236(13)71072-5.

Reynolds, R. W., N. A. Rayner, T. M. Smith, D. C. Stokes, and W. Wang, 2002: An improved in situ and satellite SST analysis for climate. *J. Climate*, **15**, 1609–1625, https://doi.org/10.1175/1520-0442(2002)015<1609:AIISAS>2.0.CO;2.

Riddle, E., M. Stoner, N. Johnson, M. L'Heureux, D. Collins, and S. Feldstein, 2012: The impact of the MJO on clusters of wintertime circulation anomalies over the North American region. *Climate Dyn.*, **40**, 1749–1766, https://doi.org/10.1007/s00382-012-1493-y .

Ropelewski, C. F., and M. S. Halpert, 1989: Precipitation patterns associated with the high index phase of the southern oscillation. *J. Climate*, **2**, 268–284, https://doi.org/10.1175/1520-0442(1989)002<0268:PPAWTH>2.0.CO;2.

Rui, H., and B. Wang, 1990: Development characteristics and dynamic structure of tropical intraseasonal convection anomalies. *J. Atmos. Sci.*, **47**, 357–379, https://doi.org/10.1175/1520-0469(1990)047<0357:DCADSO>2.0.CO;2.

Saha, S., and Coauthors, 2014: The NCEP Climate Forecast System version 2. *J. Climate*, **27**, 2185–2208, https://doi.org/10.1175/JCLI-D-12-00823.1.

Saji, N. H., B. N. Goswami, P. N. Vinayachandran, and T. Yamagata, 1999: A dipole mode in the tropical Indian ocean. *Nature*, **401**, 360–363, https://doi.org/10.1038/43854.

Schneider, T., T. Bischoff, and G. H. Haug, 2014: Migrations and dynamics of the intertropical convergence zone. *Nature*, **513**, 45–53, https://doi.org/10.1038/nature13636.

Schreck, C. J., 2015: Kelvin waves and tropical cyclogenesis: A global survey. *Mon. Wea. Rev.*, **143**, 3996–4011, https://doi.org/10.1175/MWR-D-15-0111.1.

Schreck, C. J., 2016: Convectively coupled Kelvin waves and tropical cyclogenesis in a semi-Lagrangian framework. *Mon. Wea. Rev.*, **144**, 4131–4139, https://doi.org/10.1175/MWR-D-16-0237.1.

Schreck, C. J., and J. Molinari, 2011: Tropical cyclogenesis associated with Kelvin waves and the Madden–Julian oscillation. *Mon. Wea. Rev.*, **139**, 2723–2734, https://doi.org/10.1175/MWR-D-10-05060.1.

Schreck, C. J., J. Molinari, and A. Aiyyer, 2012: A global view of equatorial waves and tropical cyclogenesis. *Mon. Wea. Rev.*, **140**, 774–788, https://doi.org/10.1175/MWR-D-11-00110.1.

Schreck, C. J., J. M. Cordeira, and D. Margolin, 2013: Which MJO events affect North American temperatures? *Mon. Wea. Rev.*, **141**, 3840–3850, https://doi.org/10.1175/MWR-D-13-00118.1.

Schreck, C. J., K. R. Knapp, and J. P. Kossin, 2014: The impact of best track discrepancies on global tropical cyclone climatologies using IBTrACS. *Mon. Wea. Rev.*, **142**, 3881–3899, https://doi.org/10.1175/MWR-D-14-00021.1.

Schreck, C. J., H.-T. Lee, and K. R. Knapp, 2018: HIRS outgoing longwave radiation—Daily climate data record: Application toward identifying tropical subseasonal variability. *Remote Sens.*, **10**, 1325, https://doi.org/10.3390/rs10091325.

Shay, L. K., G. J. Goni, and P. G. Black, 2000: Effects of a warm oceanic feature on Hurricane Opal. *Mon. Wea. Rev.*, **128**, 1366–1383, https://doi.org/10.1175/1520-0493(2000)128<1366:EOAWOF>2.0.CO;2.

Smith, T. M., R. W. Reynolds, T. C. Peterson, and J. Lawrimore, 2008: Improvements to NOAA's historical merged land–ocean surface temperature analysis (1880–2006). *J. Climate*, **21**, 2283–2296, https://doi.org/10.1175/2007JCLI2100.1.

Stewart, S. R., 2019: Tropical Storm Priscilla (EP192019). National Hurricane Center Tropical Cyclone Rep., 9 pp. https://www.nhc.noaa.gov/data/tcr/EP192019_Priscilla.pdf.

Straub, K. H., 2013: MJO initiation in the real-time multivariate MJO index. *J. Climate*, **26**, 1130–1151, https://doi.org/10.1175/JCLI-D-12-00074.1.

USDC, 2020: Weekly Weather and Crop Bulletin. Vol 107, No. 38, U.S. Dept. of Commerce, 40 pp., https://usda.library.cornell.edu/concern/publications/cj82k728n?locale=en .

Vecchi, G. A., and B. J. Soden, 2007: Effect of remote sea surface temperature change on tropical cyclone potential intensity. *Science*, **450**, 1066–1071, https://usda.library.cornell.edu/concern/publications/cj82k728n?locale=en.

Ventrice, M. J., C. D. Thorncroft, and M. A. Janiga, 2012a: Atlantic tropical cyclogenesis: A three-way interaction between an African easterly wave, diurnally varying convection, and a convectively coupled atmospheric Kelvin wave. *Mon. Wea. Rev.*, **140**, 1108–1124, https://doi.org/10.1175/MWR-D-11-00122.1.

Ventrice, M. J., C. D. Thorncroft, and C. J. Schreck, 2012b: Impacts of convectively coupled Kelvin waves on environmental conditions for Atlantic tropical cyclogenesis. *Mon. Wea. Rev.*, **140**, 2198–2214, https://doi.org/10.1175/MWR-D-11-00305.1.

Vigh, J. L., J. A. Knaff, and W. H. Schubert, 2012: A climatology of Hurricane eye formation. *Mon. Wea. Rev.*, **140**, 1405–1426, https://doi.org/10.1175/MWR-D-11-00108.1.

Villarini, G., G. A. Vecchi, T. R. Knutson, and J. A. Smith, 2011: Is the recorded increase in short duration North Atlantic tropical storms spurious? *J. Geophys. Res.*, **116**, D10114, https://doi.org/10.1029/2010JD015493.

Vincent, D. G., 1994: The South Pacific Convergence Zone (SPCZ): A review. *Mon. Wea. Rev.*, **122**, 1949–1970, https://doi.org/10.1175/1520-0493(1994)122<1949:TSPCZA>2.0.CO;2.

Waliser, D. E., and C. Gautier, 1993: A satellite-derived climatology of the ITCZ. *J. Climate*, **6**, 2162–2174, https://doi.org/10.1175/1520-0442(1993)006<2162:ASDCOT>2.0.CO;2.

Wang, B., 1994: Climatic regimes of tropical convection and rainfall. *J. Climate*, **7**, 1109–1118, https://doi.org/10.1175/1520-0442(1994)007<1109:CROTCA>2.0.CO;2.

Wang, B., and Q. Ding, 2008: Global monsoon: Dominant mode of annual variation in the tropics. *Dyn. Atmos. Oceans*, **44**, 165–183, https://doi.org/10.1016/j.dynatmoce.2007.05.002.

Wang, B., J. Liu, H. J. Kim, P. J. Webster, and S. Y. Yim, 2012: Recent change of the global monsoon precipitation (1979-2008). *Climate Dyn.*, **39**, 1123–1135, https://doi.org/10.1007/s00382-011-1266-z.

Wei, K., C. Ouyang, H. Duan, Y. Li, and S. Zhou, 2020: Reflections on the catastrophic 2020 Yangtze River Basin flooding in southern China. *Innovation*, **1**, 100038, https://doi.org/10.1016/j.xinn.2020.100038.

Wheeler, M., and G. N. Kiladis, 1999: Convectively coupled equatorial waves: Analysis of clouds and temperature in the wavenumber-frequency domain. *J. Atmos. Sci.*, **56**, 374–399, https://doi.org/10.1175/1520-0469(1999)056<0374:CCEWAO>2.0.CO;2.

Wheeler, M. C., and H. H. Hendon, 2004: An all-season real-time multivariate MJO index: Development of an index for monitoring and prediction. *Mon. Wea. Rev.*, **132**, 1917–1932, https://doi.org/10.1175/1520-0493(2004)132<1917:AARMMI>2.0.CO;2.

Wood, K. M., and E. A. Ritchie, 2015: A definition for rapid weakening in the North Atlantic and eastern North Pacific. *Geophys. Res. Lett.*, **42**, 10 091–10 097, https://doi.org/10.1002/2015GL066697.

Wood, K. M., and C. J. Schreck, 2020: Eastern North Pacific and central North Pacific basins [in "State of the Climate in 2019"]. *Bull. Amer. Meteor. Soc.*, **101** (8), S212–S214, https://doi.org/10.1175/BAMS-D-20-0077.1.

Xie, S.-P., K. Yu, Y. Du, K. Hu, J. S. Chowdary, and G. Huang, 2016: Indo-Western Pacific Ocean capacitor and coherent climate anomalies in post-ENSO summer: A review. *Adv. Atmos. Sci.*, **33**, 411–432, https://doi.org/10.1007/s00376-015-5192-6.

Yang, J., Q. Liu, S.-P. Xie, Z. Liu, and L. Wu, 2007: Impact of the Indian Ocean SST basin mode on the Asian summer monsoon. *Geophys. Res. Lett.*, **34**, L02708, https://doi.org/10.1029/2006GL028571.

Yim, S. Y., B. Wang, J. Liu, and Z. W. Wu, 2014: A comparison of regional monsoon variability using monsoon indices. *Climate Dyn.*, **43**, 1423–1437, https://doi.org/10.1007/s00382-013-1956-9.

Yuan, J., and J. Cao, 2012: North Indian Ocean tropical cyclone activities influenced by the Indian Ocean dipole mode. *Sci. China Earth Sci.*, **56**, 855–865, https://doi.org/10.1007/s11430-012-4559-0.

Zhang, C., 2005: Madden–Julian oscillation. *Rev. Geophys.*, **43**, RG2003, https://doi.org/10.1029/2004RG000158.

Zhang, C., and J. Gottschalck, 2002: SST anomalies of ENSO and the Madden–Julian oscillation in the equatorial Pacific. *J. Climate*, **15**, 2429–2445, https://doi.org/10.1175/1520-0442(2002)015<2429:SAOEAT>2.0.CO;2.

Zheng, Z.-W., 2015: A long neglected damper in the El Nino–typhoon relationship: A 'Gaia-like' process. *Sci. Rep.*, **5**, 11103, https://doi.org/10.1038/srep11103.